Possibilities of Articular Cartilage Quantification Based on High-Frequency Ultrasound and Ultrasound Palpation

D i s s e r t a t i o n

zur Erlangung des akademischen Grades
doctor rerum naturalium
(Dr. rer. nat.)
im Fach: Physik
Spezialisierung: Experimentalphysik
eingereicht an der

Mathematisch-Naturwissenschaftlichen Fakultät
der Humboldt-Universität zu Berlin

von

Diplom-Physiker (Medizinphysik) Martin Schöne

Präsidentin der Humboldt-Universität zu Berlin
Prof. Dr.-Ing. Dr. Sabine Kunst

Dekan der Mathematisch-Naturwissenschaftlichen Fakultät
Prof. Dr. Elmar Kulke

Gutachter:
1. Prof. Dr. Kay Raum
2. Prof. Dr. Dr. h.c. Peter Fratzl
3. Prof. Dr. Jan Laufer

Tag der Disputation: 23.06.2020

Abstract

In the diagnostics and repair of hyaline articular cartilage, new methods to quantify structure and mechanical capacity are required to improve the treatment of cartilage defects for millions of patients worldwide.

Surface parameters for reflectivity and roughness derived from high frequency focused ultrasound are very sensitive to superficial structural changes of articular cartilage. However, these parameters show a strong dependency on the angle of incidence of the sound field, which can hardly be controlled when investigating a native cartilage surface. This study investigates the inclination dependency and aims for a control of the inclination effects in the signal evaluation. A method was developed to reconstruct the surface of cartilage samples based on three-dimensional ultrasound scans allowing for the derivation of the angle of incidence. This enabled for a profound analysis of the inclination dependency of the surface parameters. The results provided a better understanding of the composition of ultrasonic signals from reflected and scattered components. In addition, by considering the inclination, the surface parameters for reflectivity and roughness are determined more precisely and thus enable for a differentiation between healthy articular cartilage and first degrees of degeneration.
The second part of this thesis investigates a novel volumetric quantification or cartilage repair outcomes and its correlation with established evaluation systems. On three-dimensional ultrasound scans of cartilage repair tissue on ovine femoral condyles the methods of the surface reconstruction were applied and extended to quantify the entire defect site volumetrically. The extracted parameters describe the relative defect filling and its composition of cartilaginous and bony tissue. Additionally, the samples were graded according to established scoring systems based on macroscopic evaluation, MRI scans and histology. The ultrasound-based volumetric parameters showed good correlation with these scores, especially with certain sub-scores which explicitly describe the defect filling. Based on their objective character, the ultrasound-based parameters also pointed to problems in the established methods, which can be biased.
For the biomechanical characterization of articular cartilage, a porous, viscoelastic material is assumed and experiments are usually performed on samples excised from the joint. However, the complex measuring setups used in laboratories cannot be applied to the patient. Therefore, currently physicians have to estimate the stiffness of cartilage by means of manual palpation. In the third part of this thesis, a

method denoted as ultrasound palpation is developed, which allows for measuring the applied force and strain during manual palpation in real time, solely based on the evaluation of the time of flight of ultrasound pulses. A functional prototype was developed and its measurement accuracy and reproducibility were characterized. For this purpose, measurements were conducted on phantoms and cartilage samples with and without artificial degeneration. The results were compared to indentation experiments on mechanical reference systems. It could be shown that ultrasound palpation has sufficient accuracy and reproducibility. Additionally, by repeated measurements it was possible to derive time-dependent biomechanical parameters of cartilage. Furthermore, it could be demonstrated that the biomechanical experiments lead to different results when the cartilage sample is excised from the bone instead of performing the experiment directly on the intact joint surface.

In summary, this work shows improved and new possibilities for structural and biomechanical characterization of hyaline articular cartilage and the outcomes of cartilage repair based on ultrasound data. The methods have the potential to improve the diagnostics of articular cartilage and quantification of its repair.

Zusammenfassung

In der Diagnostik und Reparatur von hyalinem Gelenkknorpel sind neue Methoden zur Quantifizierung von Struktur und mechanischer Belastbarkeit gefragt, um die Behandlung von Knorpelschäden an Millionen von Patienten weltweit zu verbessern.

Oberflächenparameter für Reflektivität und Rauheit, abgeleitet von hochfrequentem, fokussierten Ultraschall, reagieren sehr sensitiv auf oberflächliche Strukturveränderungen von hyalinem Gelenkknorpel. Jedoch zeigen beide Parameter eine starke Abhängigkeit vom Einfallswinkel des Schallfeldes, welcher bei der Untersuchung einer natürlichen Knorpeloberfläche kaum zu kontrollieren ist. Diese Studie untersucht die Neigungsabhängigkeit und zielt auf eine Kontrolle der Neigungseffekte in der Signalauswertung ab. Dazu wurde eine Methode entwickelt um basierend auf dreidimensionalen Ultraschallscans die Oberfläche von Knorpelproben zu rekonstruieren, was dann die Bestimmung des Einfallswinkels erlaubt. Dies ermöglichte eine tiefgehende Analyse der Neigungsabhängigkeit der Oberflächenparameter. Die Ergebnisse vermitteln ein besseres Verständnis über die Zusammensetzung der Ultraschallsignale aus reflektierten und gestreuten Komponenten. Zusätzlich werden die Oberflächenparameter der Reflektivität und Rauheit genauer bestimmt wenn man die Neigung berücksichtigt und ermöglichen daher eine Unterscheidung zwischen gesundem Gelenkknorpel und ersten Graden an Degeneration.
Der zweite Teil dieser Arbeit untersucht eine neue Methode zur volumetrischen Quantifizierung von Knorpelregeneraten und deren Korrelation mit etablierten Bewertungssystemen. An dreidimensionalen Ultraschallscans von Knorpelregeneraten an ovinen Femurkondylen wurden die Methoden aus der Oberflächenrekonstruktion verwendet und erweitert, um die gesamte Defektstelle volumetrisch, im Hinblick auf die relative Defektfüllung und deren Zusammensetzung aus Knorpel- und Knochengewebe, zu quantifizieren. Zusätzlich wurden die Proben nach etablierten Bewertungssystemen benotet, welche auf makroskopischer Beurteilungen, MRT-Scans und Histologie basieren. Die ultraschallbasierten Volumendaten zeigten dabei gute Korrelationen mit den Punktwertungen, besonders wenn diese explizit die Defektfüllung beschreiben. Aufgrund ihrer Objektivität wiesen die ultraschallbasierten Parameter darüber hinaus auf Probleme in den etablierten Methoden hin, da diese verzerrt sein können.
Zur biomechanischen Charakterisierung von Gelenkknorpel wird ein poröses, viskoelastisches Material angenommen und Experimente werden für gewöhnlich an Proben vorgenommen, welche aus dem Gelenk herausgeschnitten wurden. Die im

Labor verwendeten aufwendigen Messaufbauten können am Patienten jedoch nicht angewandt werden. Daher können Ärzte die Festigkeit von Knorpel bisher nur mittels manueller Palpation abschätzen. Im dritten Teil dieser Arbeit wird eine als Ultraschall-Palpation bezeichnete Methode entwickelt, um die während der manuellen Palpation aufgewendeten Kraft und Deformation in Echtzeit aufzunehmen, basierend auf der Auswertung von Ultraschalllaufzeiten. Es wurde einen funktioneller Prototyp entwickelt und dessen Messgenauigkeit und Reproduzierbarkeit untersucht. Dazu wurden Messungen an Phantomen sowie an Knorpelproben mit und ohne künstlicher Degeneration durchgeführt und die Ergebnisse mit Indentationsexperimenten an mechanischen Referenzsystemen verglichen. Es wurde gezeigt, dass die Ultraschall-Palpation eine ausreichende Genauigkeit und Reproduzierbarkeit aufweist. Durch wiederholte Messungen konnen zusätzlich zeitabhängige biomechanische Parameter von Knorpel ermittelt werden. Außerdem wurde dargelegt, dass biomechanische Experimente zu anderen Ergebnissen kommen, wenn die Knorpelprobe vom Knochen getrennt wurde, als wenn die Messungen direkt an der intakten Gelenkfläche durchgeführt werden.

Zusammenfassend zeigt diese Arbeit verbesserte und neue Möglichkeiten zur strukturellen und biomechanischen Charakterisierung von hyalinem Gelenkknorpel bzw. den Ergebnissen von Knorpelreparatur basierend auf Ultraschalldaten. Diese Methoden haben das Potenzial die Diagnostik von Gelenkknorpel und die Quantifizierung von Knorpelreparatur zu verbessern.

Contents

1 Introduction

1.1 Motivation

Cartilage, bone, muscle, tendon, and ligaments together comprise the musculoskeletal system of the human body, which builds a kind of scaffolding and provides both stability and locomotion. Articular cartilage covers the ends of bones that form a joint. In simple words, the function of cartilage is to provide shock absorption and to allow frictionless movement. However, when delving deeper into its structural and compositional aspects and their relation to the highly complex biomechanics, articular cartilage becomes very fascinating. The apparent stiffness of articular cartilage depends on the velocity of its deformation. Thus it can absorb high peak loads as occurr during jumps, but also provide wide load distribution during standing. While loading is mostly axial, joint movements additionally cause high shear forces that articular cartilage sustains by a very low friction coefficient. In contrast to bone and muscle, articular cartilage is aneural, avascular and comprises few cells (chondrocytes). The nutrition of the tissue is dependent on fluid movements induced by regular deformation of the tissue.
Currently, no artificial tissue is able to mimic the biomechanical behavior of articular cartilage and tissue engineering methods cannot induce growth of articular cartilage (Hunziker et al., 2015; Bernhard and Vunjak-Novakovic, 2016). However, there is a clinical need for such materials because adult articular cartilage has no or almost no regenerative potential. Spontaneous repair results in fibrotic cartilage with reduced mechanical competence. The epidemiologic problem of degenerated cartilage is well known - Osteoartritis (OA) - but a cure does not exist. The existing treatments can reduce pain and improve quality of life, but only for a restricted time. Currently, the last option is total joint arthroplasty. On the one hand, research is aiming for an early diagnosis of joint degeneration and to delay disease progression. On the other hand, several research groups are investigating ways of cartilage restoration or regeneration. Despite several decades of research activities, progress is very slow. One problem is the lack of suitable methods for objective cartilage characterization, which is the main motivation for the methods developed in this thesis. The methods described here support diagnostics and repair outcome evaluation of articular cartilage based on ultrasound. The research results shown here do not represent a final stage but show new ways of data evaluation and measurements methods that need to be brought to the patient.

1.2 Objectives

The main focus of this thesis is the investigation and validation of improvements in articular cartilage characterization based on ultrasound biomicroscopy (UBM) scans and by evaluation of ultrasound palpation measurements for hand-held biomechanical experiments on articular cartilage. Articular cartilage is found in synovial joints and has important functions for frictionless movement and shock absorption. However, cartilage injury, wear or degeneration in combination with its low regenerative potential lead to a high prevalence of joint pathologies, mostly osteoarthritis (OA). Several studies in many scientific disciplines have been conducted in order to allow for the detection of early signs of cartilage degeneration or to improve the outcomes of cartilage repair. This thesis is trying to support the achievement of these objectives based on ultrasound technologies.

UBM has been investigated for two decades as a method for quantification of articular cartilage. It has been shown that healthy articular cartilage shows the highest ultrasound reflectivity, and with degeneration, the reflectivity decreases. UBM also allows for assessment of the surface roughness, which is shown to increase with degeneration. It is known that both surface parameters - reflectivity and roughness - have a strong inclination dependency. Though the shape of articulating surfaces are mostly convex, at some sites they are concave. Thus, surface parameters of cartilage derived from 3D ultrasound scans are therefore additionally influenced by the local surface inclination. Perpendicular alignment of the transducers sound field to the surface is restricted to a specific spot only. For intra-articular ultrasound scans, which are currently under investigation, the alignment gets even more complex. Within the first study of this thesis, I followed three aims:

- Calculation of the local surface inclination based on the pulse-echoes of 3D UBM scans on articular cartilage.
- Investigation of the relation between surface parameters and their corresponding local inclination and based on that improve the parameterization of cartilage samples.
- Applying the newly developed methods to data of human articular cartilage of different stages of degeneration and compare the ultrasound parameters to histological grading scores.

The methods were developed on ultrasound scans on spherical rubber phantoms with different acoustic properties. The human cartilage samples were obtained from patients who underwent total knee arthroplasty and from human cadavers without joint degeneration.

Next to cartilage degeneration, research is also focusing on the regeneration of articular cartilage. Currently, no method is found to restore lost cartilage with a repair tissue which is structurally and biomechanically comparable to healthy hyaline articular cartilage. The repair outcomes are as diverse as the different repair approaches. Next to macroscopic evaluation, histology and magnetic-resonance imaging, ultrasound has been used in some studies to quantify the outcomes of experimental animal studies. However, ultrasound based quantification is not standardized but several attempts of varying complexity have been proposed. The reported methods comprise subjective grading of cross-sectional images, quantification of the brightness of backscatter signal and depth-dependent spectral analysis of the backscatter signal. However, cartilage repair methods are currently not reliable in filling the former defect. Thus, it is not very meaningful to describe cellular density and viability, the hyaline similarity or proteoglycan content when the defect is only partially filled. Based on that we elaborated how cartilage repair tissue can be quantified volumetrically based on 3D UBM data. This is summarized in study II, with the following main objectives:

- Developing methods to reconstruct the geometry of the cartilage defect area and surrounding healthy tissue based on 3D UBM data.
- Estimating the shape of the original cartilage surface based on these data, and deriving parameters for the volumetric characterization of the repair tissue.
- Comparing the derived volumetric parameters to scores obtained from established classification systems based on macroscopic evaluation, MRI and histology.

This study was conducted within a large pre-clinical trial of scaffold-based cartilage repair on sheep. The ultrasound data were acquired with a portable ultrasound scanner next to the operation theater directly after opening the joints.

Another huge topic in cartilage research is the biomechanical characterization of articular cartilage. On the one hand, the biomechanics of cartilage already changes with the first degeneration, or even before. On the other hand, cartilage repair aims not only to fill the defect but also to create a biomechanical competence comparable to that of native hyaline cartilage, which is currently not achievable. Most of the biomechanical studies were done with excised cartilage samples mounted into precise but large material testing machines. Such experiments cannot be performed intra-operatively. Therefore, some devices have been introduced to allow intra-operative biomechanical cartilage testing. Clinically, there is a need for such methods, but such a device is not currently available on the market. The reasons are variable, but may be due to a lack of reliability and comparability in the results. In this thesis we found a way for a simple measurement of the manually applied stress and strain during palpation of cartilage. Referring to a similar device for scar tissue, we named

this method ultrasound palpation (USP) (Raum et al., 2013). The third part of this thesis focuses on the realization of this method based on the following objectives:

- Investigating and understanding the principles and side-effects of USP.
- Designing and developing a functional prototype.
- Comparing USP measurements to conventional indentation experiments for phantoms and cartilage samples and defining reliability and repeatability.
- Analyzing whether the correction method from indentation is suitable for USP.
- Investigating cartilage's sensitivity to degenerative changes and the effect of samples preparation.

The experiments in this part were performed on custom-made rubber phantoms and on porcine cartilage samples. To simulate degeneration, cartilage samples were partially enzymatically digested.

1.3 Outline

The structure of this thesis shall briefly be outlined here, based on the objectives formulated beforehand.

Chapter 1 provides an introduction to the context and motivation for this thesis. It points out the fascination and the challenges articular cartilage provides and gives a preview of the presented research. Additionally, the detailed objectives of this thesis are formulated.

Chapter 2 describes the state of the art with respect to the materials and methods of this thesis. This comprises the explanation of articular cartilage structure, composition, and biomechanics, as well as potential degenerative changes. Current strategies in the diagnosis and treatment of Osteoarthritis (OA) and focal cartilage defects are presented. Furthermore, the required physical principles of ultrasound and biomechanics are summarized here.

Chapter 3 contains the first experimental study of this thesis (Study I). In this study ultrasound scans of different rubber phantoms were acquired to investigate the principles of inclination dependency of ultrasound surface parameters for reflectivity and roughness. These scans were also used to optimize the data evaluation methods that were eventually applied to high-frequency ultrasound data of human cartilage. In the last step, the derived ultrasound parameters were compared to histological scores that allow for grading of different degeneration stages.

Chapter 4 is about the volumetric characterization of cartilage repair tissue based on UBM scans (Study II). Based on the UBM data the initial cartilage thickness and the defect volume were estimated. Further, different parameters were derived to quantify the filling of the defects as well as irregularities in the subchondral bone plate. The same samples have been investigated by gross macroscopy, histology, and partially by MRI. Clinicians viewed these data and scored them according to established classification systems. Finally, a profound statistical analysis was conducted to compare the volumetric scores from UBM to the scores of the classification systems.

Chapter 5 describes the experimental studies on the novel ultrasound palpation (Study III). In preliminary tests, the physical principles are elaborated and the mechanical and acoustical limitations have been considered. Then a prototype was developed and first validated on rubber phantoms and then used to investigate cartilage samples. Conventional indentation experiments were performed as reference measurements.

Chapter 6 provides an overall conclusion to this thesis and closes with an outlook.

2 State of the Art

Cartilage is a flexible and elastic connective tissue and classified in three types: *hyaline* cartilage, *elastic* cartilage and *fibrocartilage* (Staubesand et al., 1985). This thesis always refers to hyaline cartilage.

2.1 Articular cartilage, structure, development, and repair

Articular cartilage covers the articulating surfaces of bones within synovial joints (Fig. 2.1). Its mechanical properties are highly complex and unrivaled by any artificial material. The knee joint, the largest joint in humans, is a compound joint of condyloid and saddle joint (Fig. 2.2). The femur condyles and tibia plateau build the condyloid joint, enabling flexion and extension of the lower leg. During motion of the lower leg, the patella slides in the V-shaped trochlea of the femur. The involved structures of this interplay are called the patellofemoral joint. The surfaces of articular cartilage are very smooth and together with the viscid synovial fluid, the movement is almost frictionless. At the same time, the cartilage layers have to withstand high loads of 200 - 300 % of body weight during routine daily activities (Kutzner et al., 2010). Such loadings can be static, e.g. standing, or dynamic, e.g. walking, running, jumping.

2.1.1 Structure and composition

In contrast to most other tissues, articular cartilage is avascular and aneural and with a sparse amount of cells (3 % wet weight) (Bronner and Farach-Carson, 2007). Its main component is water, between 70-80 %. The extracellular matrix consists of collagen type II (60 % dry weight) and proteoglycan macromolecules (20-30 % dry weight) (Mow et al., 1984). Despite its homogeneous appearance, adult articular cartilage is divided into four layers, wherein each layer is specified by its collagen orientation, cell shape and amount, proteoglycan content, and water content. From surface to bone, these are described as superficial, tangential, radial, and calcified layer (Fig. 2.3). In the radial zone, the collagen fibers are aligned perpendicular to the surface, then change orientation in the tangential zone and reach the superficial

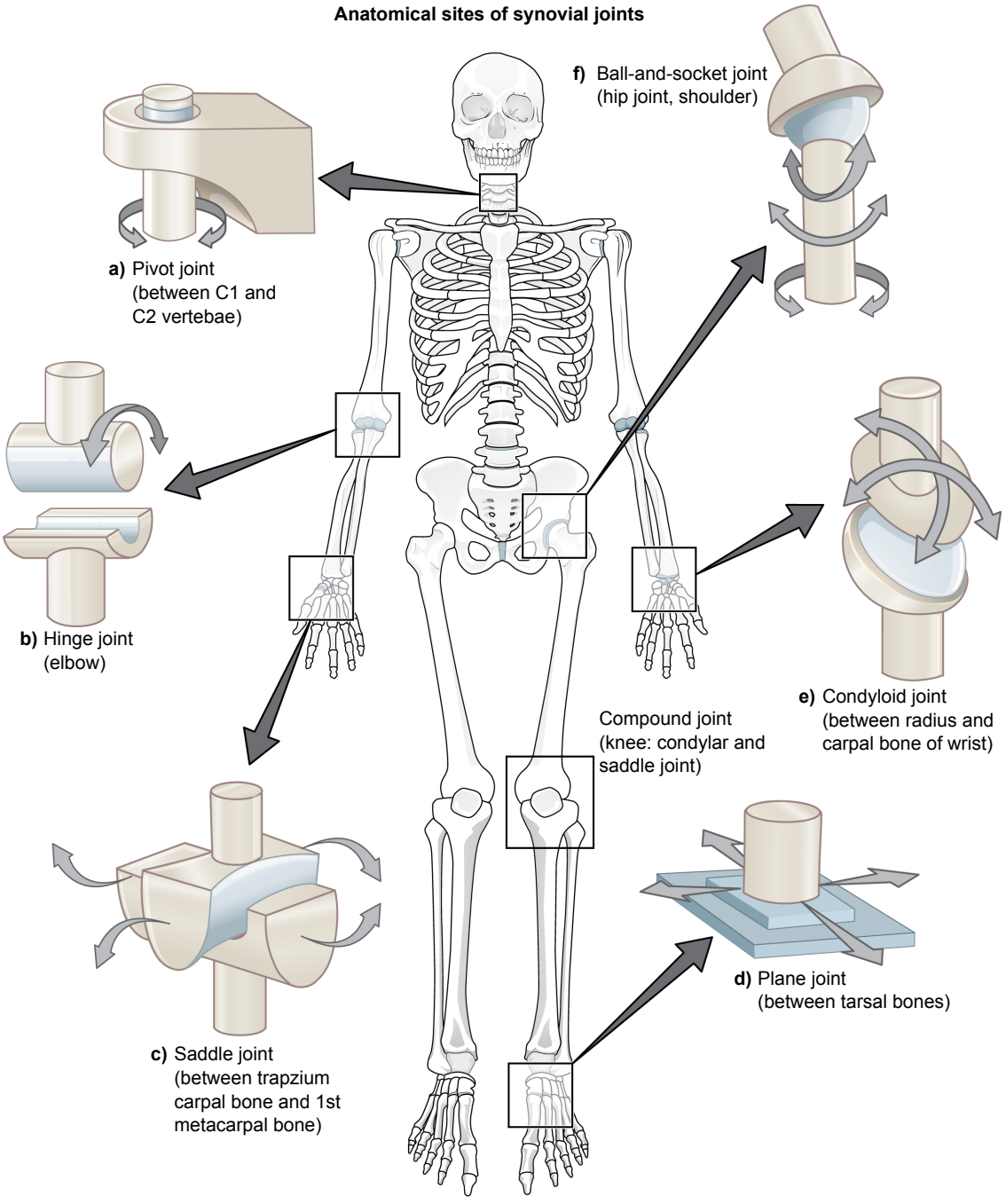

Figure 2.1 – Overview of anatomical sites of synovial joints and different joint types. (adapted from the original work of OpenStax College[a], license: CC BY 3.0)

[a] http://cnx.org/contents/FPtK1zmh@6.27:bFtYymxt@4/Synovial-Joints

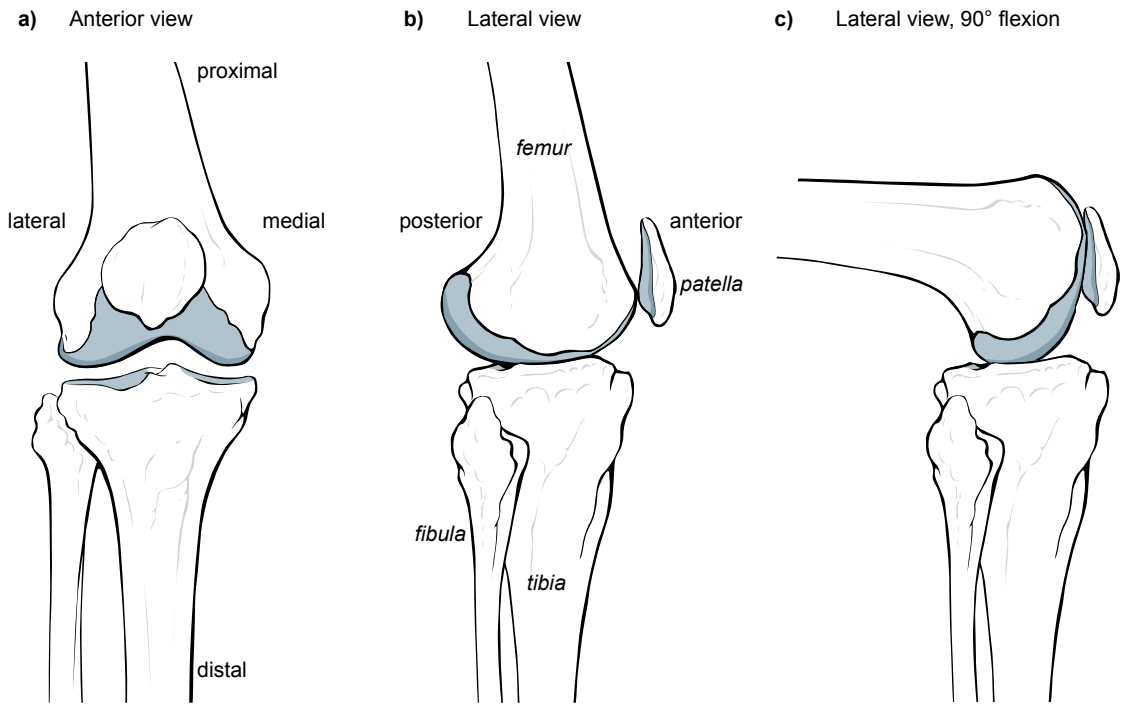

Figure 2.2 – Schematic drawing of the bones of knee joint in a) anterior, b) lateral view at 0° flexion and c) at 90°. Articulating surfaces are covered by articular cartilage (gray areas). Other important structures like tendons and meniscus are not shown. (adapted from the original work of Patrick J. Lynch[a], license: CC BY 2.5)

[a] https://en.wikipedia.org/wiki/File:Knee_skeleton_lateral_anterior_views.svg

zone with parallel aligned collagen fibers - the so-called arcade-like alignment (Benninghoff, 1925). This should provide resistance to shear forces and axial load. The cartilage cells - chondrocytes - are small, flat, and in higher density at the superficial layer. In the tangential zone, they are more round and distributed separately. In the radial zone, they build chain-like constructs of several chondrocytes aligned in parallel to the collagen fibers. Also the proteoglycan concentration shows depth-dependent distributions, from a low amount close to the surface to a high amount deeper down (Mow et al., 1984). The fourth layer, the calcified layer, builds the connection between the subchondral bone plate to the non-mineralized cartilage. This layer is composed of chondrocytes, collagen type II, and proteoglycan, but also of components that compose bone, i.e. hydroxylapatite minerals and collagen type I (Hoemann et al., 2012).
Some literature denoted the first 6 - 15 μm of the cartilage surface as additional layer, called either *most superficial layer* or *lamina splendens* (Fujioka et al., 2013). This layer shows a layered ultrastructure, incorporating collagen type I and III as well as lipids, proteins, and proteoglycans (Yoshida et al., 2004; Fujioka et al., 2013).
The nutrition of articular cartilage relies on the exchange of interstitial water with synovial fluid induced by cyclic loading and unloading phases (O'Hara et al., 1990; Hassenpflug, 2007). It has been shown that cyclic loading is most effective to increase the exchange for large solutes like growth factors, hormones, enzymes, and cytokines that have strong regulatory effects on cell metabolism (O'Hara et al., 1990).

Collagen

Collagen is a common protein found in all animals. In humans, for example, one-third of the total protein is collagen (Shoulders and Raines, 2009). In vertebrates, 28 different types of collagen have been identified. Collagen type I is the most abundant, and is found in the skin, bones, tendons, and ligaments. All collagen types in common are their secondary structure of a right-handed triple helix, called tropocollagen, that is comprised of three parallel procollagens (Shoulders and Raines, 2009). On the primary structure level, the procollagen chains have a regular pattern of amino acids with glycine (Gly) at every third position. Between two Gly any combination of amino acids Xaa and Yaa can be placed. Finally, the chains consist of repeating XaaYaaGly sequences. For collagen type I the triple helix consists of two identical chains and a third chain with different amino acids. In contrast, collagen type II consists of three identical chains (Shoulders and Raines, 2009).
Since collagen type II is the dominant collagen in cartilage, this work always refers to collagen type II if not stated otherwise.

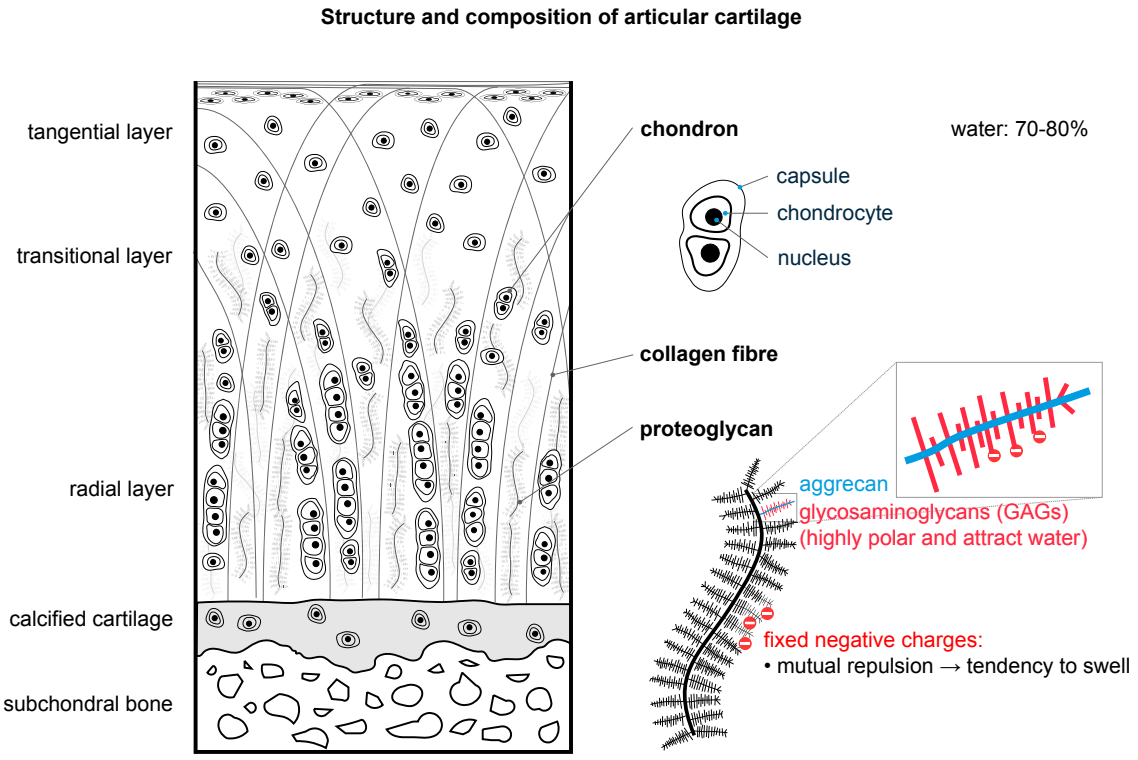

Figure 2.3 – Illustration of the structure and composition of articular cartilage.

Proteoglycans

Proteoglycans (PG) are large proteins that consist of a core protein to which several glycosaminoglycan (GAG) chain are attached by covalent bonding. The GAG chains are negatively charged and therefore attract water or ions like Na^+ or Ca^{2+}. Since these negative charges are bound to the molecule, they are often denoted as *fixed charges* (Lu and Mow, 2008). In cartilage, several single PG units are connected to a backbone of hyaluronic acid and form a huge macromolecule. The water attraction and repulsive forces between the negatively charged endings of the GAG chains are then multiplied and cause swelling of the molecule.
In cartilage, aggrecan is the most abundant PG with GAG chains of chondroitin sulfate and keratan sulfate. The trypsin that is used within this study to artificially degenerate cartilage digests predominantly the PG and is therefore a good model to simulate the stiffness loss of early-stage osteoarthritis (Moody et al., 2006).

2.1.2 Osteoarthritis

Osteoarthritis (OA) is a progressive disease of joints that lead to symptoms which are associated with gradual degeneration of the integrity of articular cartilage. Though

degeneration of articular cartilage is the key feature of OA, the entire joint is affected, including underlying bone and the synovial capsule (Bronner and Farach-Carson, 2007). Osteoarthritis can occur in all synovial joints (Fig. 2.1), most affected are the fingers, cervical and lumbar spine, hip, knee, and ankle joints. Of all joints, the knees have the highest prevalence of OA. Affected patients suffer from pain, joint stiffness, reduced mobility, and an overall loss of quality of life. Additionally, reduced activity can further promote cardiovascular weakening or disease (Hassenpflug, 2007).
Worldwide more than 250 million people are affected with knee OA. That is 3.6 % of the total population. Interestingly, women are more often affected (4.7 %) than men (2.6 %) (Vos et al., 2012). Above the age of 60, 10 % of men are affected and 18 % women (Glyn-Jones et al., 2015).
Interestingly, when controlling for age and body mass index (BMI), the prevalence for knee OA for postindustrial (late 20th to early 21th centuries) individuals is 2.1 time higher than for early industrial (19th to early 20th centuries) individuals (Wallace et al., 2017). Thus, increased BMI alone is not explaining the increased prevalence of OA. Other factors that changed significantly during the last century must also play an important role. This could be activity patterns, genetic changes, changes in diet or others (Wallace et al., 2017).
The economic burden of OA is remarkably high. Considering the treatment costs and indirect costs from loss of productivity the total amount in developed countries is estimated to be in the range of 1 - 2.5 % of the gross domestic product (Glyn-Jones et al., 2015).

Signs and progression of OA

OA is a complex disease which usually progresses over years and affects the entire joint, including cartilage, bone, and the synovium (Glyn-Jones et al., 2015). On the cartilage level it starts with the superficial destruction of the extracellular matrix when fibrillation occurs, i.e. the firm confinement of collagen fibers and proteoglycan become loose. This loss of integrity leads to reduced biomechanical durability. At this point, the patient usually does not notice any changes, has no pain nor a reduced range of motion. Therefore the joint is used and loaded as usual. However, the reduced biomechanical durability and the continued loading leads to further progression of cartilage loss. Thus, the cartilage layer degenerates more and more, until the end stage in which the subchondral bone is exposed.
Also, the changes in the subchondral bone are highly complex. In OA the cortical plate and trabecular bone change their structure due to the beginning of ossification processes the subchondral region remodels and vascularisation increases. Clear structural features of these changes are osteophytes and subchondral cysts (Glyn-Jones et al., 2015). Both chondrocytes in cartilage and osteoblasts in bone respond to mechanical changes with enhanced production of inflammatory cytokines and

matrix-degenerating enzymes (Glyn-Jones et al., 2015).
The synovium or synovial membrane is a thin layer of tissue containing cells, nerves, and vessels lining the inner joint space below the tissue of the joint capsule (Smith, 2011). Already in early-stage OA an inflammation of the synovium – synovitis – is common (Glyn-Jones et al., 2015). The inflammation is triggered by debris from the degeneration of the cartilage matrix and results in the release of inflammatory cytokines and additional matrix-degenerating enzymes.
Structural changes in the subchondral bone, degeneration of the cartilage extracellular matrix and joint wide inflammation responses render a positive feedback loop which constantly maintains the degenerative and inflammatory processes of OA (Smith, 2011; Glyn-Jones et al., 2015).
In early stage OA, affected patients do not suffer any symptoms and therefore do not seek medical advice. Since X-ray images only show mineralized tissue, OA only becomes visible after the joint space has already reduced. Unfortunately in this stage, OA has already progressed and is affecting the entire joint. Innervated bone and synovium generate pain, and swollen tissue decreases mobility. Therefore the symptoms of OA, pain and immobility, are generated by the inflammation of the osteoarthritic joint, but not directly from the degenerated cartilage (Glyn-Jones et al., 2015).

Causes of OA

OA can be classified into primary (or idiopathic) OA and secondary OA (Altman et al., 1986).
Primary OA occurs without any joint-affecting disease or prior events that altered the biomechanics of the joint. However, there are several risk factors known. A single risk factor is not very predictive, but a summation of several risk factors increases the likelihood of the development of OA. The strongest isolated risk factor is age, therefore it can be assumed that regenerative potential and summation of risk factors contribute to OA (Glyn-Jones et al., 2015). The theory that repeated overloading leads to degenerative changes has been well investigated (Willie et al., 2015) and it is known that some kinds of occupations when they are performed regularly, e.g. working in bent positions, also increase the risk for OA (Chaganti and Lane, 2011). Obesity, on the one hand, increases the load on the joints, while on the other hand, increased amount of inflammatory adipokines increases the susceptibility of joints (Glyn-Jones et al., 2015). Other risk factors for primary OA are genetic predisposition (Spector and MacGregor, 2004), hormone change after menopause (Linn et al., 2012), nutrition, and ethnicity (Chaganti and Lane, 2011).
A secondary OA is related to a traumatic injury, a disease, or bone or joint disorders (Altman et al., 1986). Focal cartilage defects or structural lesions of the cartilage layer can either occur during traumatic injuries, often sport injuries, or during the progression of a disease (Hunziker et al., 2015). Such lesions can arise

to the superficial layer of cartilage merely, affect the full-thickness cartilage layer or even include the subchondral bone. Non of these defects heal spontaneously in adult cartilage. The smaller the defect, the smaller the probability that the defect is diagnosed. However, with time such defects increase in size and depth and progress slowly to a manifested OA. Pathological changes in the musculoskeletal system like hip dysplasia, varus, and valgus knee alignment or leg length inequality cause infaust biomechanics and often lead to OA (Glyn-Jones et al., 2015). Similarly knee instability after meniscus tear or cruciate ligament injury also lead to altered biomechanics and with time to the development of OA (Willie et al., 2015).

2.1.3 Treatment and repair

Conservative treatment

Intra-articular injections of hyaluronic acid are the first choice for conservative treatment of OA. Lavage and shaving describe minimal invasive procedures were the joint is rinsed with physiological solutions or surfaces are mechanically smoothed. Debridement is a combination of both and can comprise the removal of the menisci, free bodies, or osteophytes. From non of these treatment healing be expected, operative methods like knee arthroplasty can be delayed, though. However, the biomechanical rationale behind it is highly questionable. Nevertheless, these treatments improve the quality of life for a lot of patients for several months (Hunziker, 2002; Wang et al., 2004).

Repair approaches

In contrast to the treatments mentioned above, repair approaches aim for improvement of the quality of life and restoration of the original cartilage layer. The current repair approaches can roughly be separated into strategies intended to foster the spontaneous repair response by bone marrow stimulation and in strategies based on graft transplantation.
Abrasion chondroplasty, Pridie drilling, and microfracturing are techniques that induce a spontaneous repair response triggered by bleeding from the subchondral bone into the cartilage defect. In all these techniques the subchondral bone plate is perforated to induce bleeding and subsequent blood-clot formation. The blood carries pluripotent stem cells and triggers a repair response. With time this develops into fibrocartilaginous repair tissue that fills the defect. Nevertheless, the biomechanical durability and the integration with adjacent healthy cartilage is very poor (Hunziker, 2002).
In the last decades, several techniques have been introduced that fill a defect in cartilage by implantation of a suitable graft. Usually, these grafts are either osteochondral cylinders or artificial cell-seeded grafts. Osteochondral autografts are cylinders of bone and cartilage that are removed from a non-load bearing region of

the joint and then implanted in the defect area. One option is the transplantation of a single large osteochondral cylinder, called osteochondral transfer. The second possibility is to harvest several small-diameter cylinders and use them to reconstruct the cartilage surface by mosaicplasty (Hunziker et al., 2015). The largest drawback of autologous grafting is the creation of new defects. Ideally, the donor sites are located in non-weight bearing regions and get filled by a suitable grafting material (Patil and Tapasvi, 2015). The second problem with unknown impact is the re-implantation of the osteochondral plug that is press-fitted by hammering. This could damage the matrix and chondrocytes and lead to early failure of the transplanted cartilage (Hunziker et al., 2015). Since the cartilage layer thickness within a joint is not constant, the donor site and target site do not match in thickness. When inserting the graft the surgeon tries to place the cartilage surfaces flush. However, it is not known whether the subchondral bone layers match or not (Koh et al., 2004; Latt et al., 2011).
The current state of the art in cartilage repair by transplantation is based on cell-seeded grafts. This area comprises several techniques that all have in common that chondrocytes are harvested in a first surgery, then cultivated in a laboratory and finally seeded on a suitable scaffold that is finally implanted into the cartilage defect (Gelse et al., 2010; Marquass et al., 2011; Hunziker et al., 2015).

Joint replacement

A joint replacement surgery is currently the gold standard for end-stage OA patients. It is a reliable surgical procedure to relieve patients from pain and to restore normal functionality of the joint and therefore significantly improve their quality of life (Witjes et al., 2016). In Germany, approximately 440,000 hips and knees got treated annually by arthroplasty (Ärzteblatt, 2019). In the last few years, the number of joint replacements has increased constantly (Maradit Kremers et al., 2015).

2.2 Clinical and experimental characterization of articular cartilage

2.2.1 X-ray

Radiography is a standard technique in clinical evaluation that uses the attenuation of X-rays to create plain images of the joints. The attenuation of X-rays depends on the X-ray energy, on the thickness, mass density and the atomic number of the material (Krieger and Petzold, 1998). Radiography provides high-resolution images of good contrast for bone. However, soft tissue contrast is very weak (see Fig. 2.4 b). Therefore, cartilage degeneration only becomes visible indirectly, by narrowing of the joint space. In advanced OA, osteophystes, i.e., changes in the subchondral

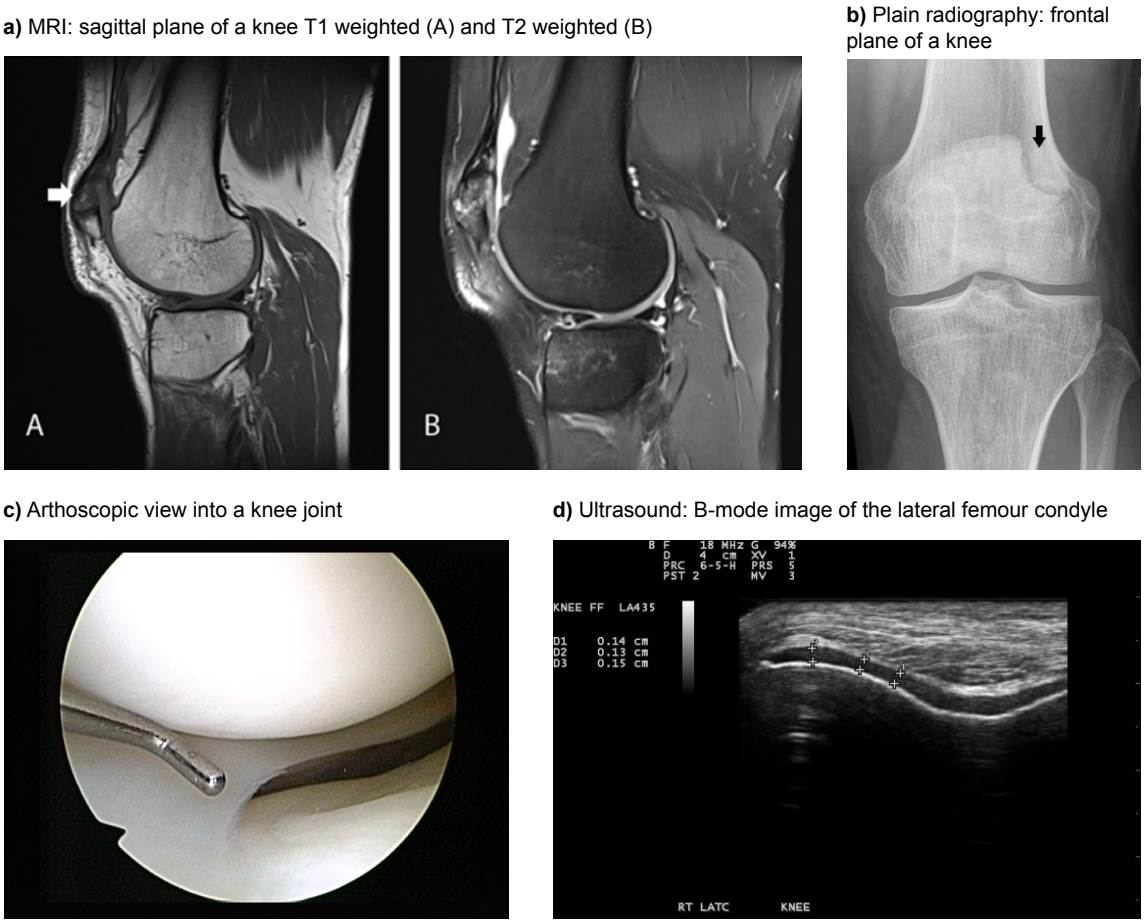

Figure 2.4 – Examples of clinical imaging methods on healthy articular cartilage. a) Sagittal MRI images of a knee with different relaxation time weightings.[a] b) Plain radiography of a knee in frontal plane.[b] c) Arthroscopic view into a knee joint showing cartilage of femur and tibia.[c] d) Ultrasound B-mode image of the lateral femur condyle. The anechoic zone represents the cartilage.[d]

[a] Images taken from (Vanhoenacker et al., 2016), distributed under CC-BY-SA 4.0.
[b] Image taken from (Vanhoenacker et al., 2016), distributed under CC-BY-SA 4.0.
[c] Image taken from https://commons.wikimedia.org/wiki/File:Lateral_meniscus_lateral_edge.jpg, distributed under CC-BY-SA 4.0 by user *Arthroscopist*.
[d] Image taken from (Abraham et al., 2011), distributed under CC-BY-SA 2.0.

bone, show up in radiography. The standard radiography based grading of OA is done following the scale proposed by Kellgren and Lawrence, which uses grades from 0 to 4 and is based on judgment of joint space narrowing and the occurrence of osteophytes (Neu, 2014). Computer tomography (CT) can provide additional structural information about the mineralized part of the joint, but the contrast is the same as for plain radiography.

2.2.2 Magnetic resonance imaging

Magnetic resonance imaging (MRI) is based on the principle of nuclear magnetic resonance, which describes the absorption and emission of electromagnetic radiation of atomic nuclei in an external magnetic field. This is only possible for isotopes with unpaired protons or neutrons. Such isotopes have an additional angular moment (spin) and a magnetic moment. Exposed to an external, static magnetic field, a torque is exerted to the magnetic moment of the particle. In combination with its angular moment it starts a precession movement with the so-called Larmor frequency about the direction of the external magnetic field. The Larmor frequency depends on the magnitude of the external magnetic field and the type of particle. Clinical MRI is usually proton based, where the Larmor frequency is in the MHz range for a 1 Tesla magnetic field. A patient is placed in a large static magnetic field, so all protons of his body precess with the same frequency except those who are aligned parallel to the external magnetic field. So far the dipoles are oriented according to the Boltzmann distribution and only a low magnetization into the longitudinal direction (parallel to the static magnetic field) can be measured. Then an external, high-frequency magnetic field is controlled perpendicular to the static magnetic field with a frequency in resonance with the Larmor frequency of the protons. This causes the magnetic dipoles to align perpendicular to the static field and get in phase. This creates a transversal magnetization which can be measured by coils. An additional static gradient field slightly changes the Larmor frequency to create spacial frequency differences which are used later for spacial separation of the signals.
The basic principle of the imaging process is to align the dipoles in longitudinal or transverse direction and measure the relaxation times until equilibrium is reached. Each tissue has different relaxation times which finally creates the contrast in the images. The relaxation of the magnetization in the direction of the static magnetic field is called spin-lattice relaxation or short T1. This is mainly depending on the surrounding atoms and the viscosity of the tissue. Spin-spin relaxation, or T2, is the relaxation of the magnetization perpendicular to the static magnetic field and caused by spin dephasing. The images can be T1- or T2-weighted in order to optimize the contrast for the tissue of interest (see Fig. 2.4 a). The combination of gradients and pulses for the high-frequency magnetic field are described in an MRI

sequence and eventually defines the appearance of the final MRI image, its acquisition time and resolution. There exists a plethora of MRI sequences developed for specific diagnostic needs for each organ and tissue and even to visualize molecular concentrations. MR imaging of the knee provides a very good distinction between all main structures of the joint: ligaments, menisci, bone and articular cartilage. So MRI is suitable for imaging of joint injuries and structural changes by certain diseases including OA (Neu, 2014). Common MRI sequences for cartilage imaging are T2 mapping, T1rho relaxion mapping, dGEMRIC, but there are several more (Guermazi et al., 2015). The T2 relaxation time in cartilage corresponds to the water content, collagen content and collagen orientation and increased relaxation times indicate cartilage degeneration (Guermazi et al., 2015). The regular structures of collagen make T2 measurements in cartilage prone to the magic angle effect and could cause artifacts. In the case the collagen fibers are oriented 55° to the static magnetic field the relaxation is delayed, resulting in increased relaxation time and finally in a increase brightness in the image (Guermazi et al., 2015). Since higher T2 is interpreted as degenerated cartilage, the magic angle artifact can result in a wrong diagnosis. T1rho belongs to the spin-lattice relaxation but is similar to the T2 relaxation. It is derived from multiple images with additional spin-lock pulses of different length. It has been shown that T1rho is sensitive to the proteoglycan concentration in cartilage. In general T1rho mapping shall be more sensitive to early stages of cartilage degeneration than T2 mapping (Guermazi et al., 2015). The concentration of GAG can be measured using dGEMRIC - *delayed gadolinium-enhanced MRI of cartilage*. This is a T1 based imaging method that requires the injection of gadolinium contrast agent. The contrast agent contains negatively charged ions of gadopentetate dimeglumine Gd-DTPA^{2-}. When distributing in cartilage, Gd-DTPA^{2-} is repelled by the negatively charged GAG and therefore shows a inverse distribution than the proteoglycans. MR imaging with gGEMRIC has been shown to be sensitive to osteoarthritic cartilage since the GAG concentration decreases in OA (Guermazi et al., 2015). However, currently the usage of gadolinium contrast agents is under discussion since there are indications for potential gadolinium retention in the human body. Some marketing authorisations for gadolinium contrast agents have been suspended in the European Union just recently (Dekkers et al., 2018).

MR imaging has also been thoroughly investigated for the evaluation of cartilage repair outcomes. The MOCART score (Magnetic Resonance Observation of Cartilage Repair Tissue) was introduced in 2004 to allow characterization of the repair outcome using 9 variables. The sequences that have to be used were also defined. Thus this method has become a standard in cartilage repair evaluation even if the reliability of the score is still under discussion (Marlovits et al., 2004; Blackman et al., 2013; Windt et al., 2013a).

Even though MRI provides a very good overview of all structures in the joint, the majority of orthopedic surgeons prefer an additional diagnostic arthroscopy when

treatments of the articular cartilage are required (AQUA, 2011).

2.2.3 Arthroscopy

Arthroscopy is a minimally invasive surgery where the surgeon brings an arthroscope and surgical instruments into the joint. The arthroscope is an optical device with a light source and camera that provides real-time insight into the joint. Additional tools are inserted depending on the current need. For diagnostics, the surgeon uses an arthroscopic probe, i.e. a metal rod with an angled tip, for direct perception of the structures inside the joint (see Fig. 2.4 c). For some treatments scissors, forceps or shavers can also be moved into the joint. There is a critical discussion about the solely diagnostic usage of arthroscopy because there is always the risk of joint infection along with the usual risks of surgery with general anesthetic (Moseley et al., 2002; Kim et al., 2011; Salzler et al., 2014). Any benefit of knee arthroscopy over a long term has been disproved. Nevertheless, knee arthroscopy is the most common orthopaedic outpatient surgery in the USA (Brignardello-Petersen et al., 2017).

2.2.4 Ultrasound in a clinical setup

Clinical ultrasound imaging is also used to investigate the condition of ligaments, synovium, menisci, and articular cartilage as well as bone abnormalities in joints (Keen and Conaghan, 2009; Neu, 2014). It is used to image shoulder, knee, feet, and finger joints with respect to changes caused by OA or rheumatoid arthritis (Keen and Conaghan, 2009). Healthy articular cartilage appears anechoic with the rather low frequencies used for transcutaneous ultrasound (see Fig. 2.4 d). In the last years the interest in ultrasound for the quantification of articular cartilage, especially of the knee joint, has increased and ultrasound based grading systems have been developed (Saarakkala et al., 2012; Riecke et al., 2014). It was shown that ultrasound based semi-quantitative assessment of tibio-femoral osteophytes, medial meniscal extrusion and degeneration of the medial femoral cartilage layer performs better than radiography (Podlipská et al., 2016). The diagnostic performance of ultrasound semi-quantitative scores with MRI based grading as reference was found to be excellent to good (Podlipská et al., 2016). Ultrasound imaging is restricted to soft tissue that is not covered by bony tissue. Therefore, the ultrasound imaging access to the joint space and articular cartilage is limited. By flexion of the joint, the accessible range can be changed (Keen and Conaghan, 2009). However, in the case of advanced OA the maximum flexion is maybe already limited and the accessible region is further restricted (Podlipská et al., 2016). Ultrasound imaging is a method where the physician directly investigates the patient, which is in great contrast to X-ray, MRI and histology. On one hand, the clinicians need to get trained and they need to have the time to conduct ultrasound examinations. On the other hand,

ultrasound examination could reduce cost and shorten the time for the diagnostic process (Podlipská et al., 2016).

2.2.5 Histology

The determination of the histological quality is the gold standard when concerning the evaluation of microscopic structures of cartilage and cartilage repair tissue. Histological slides are usually prepared from animal models in experimental or preclinical studies or from human biopsies obtained in second-look arthroscopy during a clinical trial. The sample preparation comprises fixation, decalcification, embedding, cutting, and staining (Willbold and Witte, 2010). Therefore, histology is a destructive and time-consuming method. However, the detail of information about the structural and chemical composition of the material is superior to all other methods. Histological slides are usually graded based on classification systems to quantify the outcomes (Rutgers et al., 2010). Scoring systems especially for articular cartilage have existed for several decades and increased to a total of 21 classification systems since the 1990s (Rutgers et al., 2010). Classification systems are designed to either describe osteoarthritic cartilage or cartilage repair tissue. A further discrimination is made between scores developed for animal studies or for human samples. In animal studies, the entire joint is sectioned and thus the evaluation of a repair site allows for the comparison with the surrounding healthy tissue. This allows for detailed assessment of the thickness of the repaired tissue and the shape of the subchondral bone (e.g. O'Driscoll (O'Driscoll et al., 1988)). In contrast, in-vivo samples from human are obtained from a 2-mm diameter biopsy taken from the central site of the defect. Therefore, the samples provide only a confined insight into the defect and different scores are required than for a section of the entire joint.

2.2.6 Other experimental methods

The methods explained so far are used in daily clinical routine for cartilage diagnostics and follow-up. The following methods are purely experimental and all aim to improve the characterization of articular cartilage and cartilage repair outcomes. Near-infrared spectroscopy (NIRS) was shown to correlate with cartilage degeneration (Spahn et al., 2007). In NIRS measurements the reflection of a broad infrared spectrum on a sample is compared to a reference spectrum acquired from an idealized perfect reflector. The near-infrared spectrum describes the short-wavelength infrared light which is known to be absorbed by small molecules. Thus, the difference spectrum between sample and reference is reduced in some frequency bands. The near-infrared absorption at cartilage indirectly correlates to the water content. Spahn et al. developed an arthroscopic NIRS sensor that became the only medical device for cartilage quantification with CE approval. They showed that the near-

infrared absorption for healthy cartilage is significantly smaller than for cartilage with signs of degeneration (Spahn et al., 2007, 2008, 2010, 2013).
Optical coherence tomography (OCT) is another optical method which has been applied for cartilage characterization. It is basically based on a Michelson interferometer and a broadband source of coherent light with short coherence length. The light is split into a reference and a sample path. The light of the sample path is emitted to the sample and backscattered light is guided back to the interferometer where it is merged with the reference path. The merged light is modulated by destructive and constructive interference depending on the path difference and the wavelength. By changing the path length of the reference path an interference pattern is created. This allows to precisely measure the distances of light backscattering sources in the sample along the light beam axis (Huang et al., 2011). By scanning the light of the sample path over the sample, 2D cross-sectional images or 3D data can be acquired very similar to ultrasound scanning (Nebelung et al., 2015). Similar to ultrasound, OCT data on healthy cartilage show a strong signal on the surface (reflection) and backscattering from below the surface (Han et al., 2003). However, the maximum penetration depth in cartilage is below 2 mm (Puhakka et al., 2016).
It has already been shown that OCT is able to visualize structural changes in cartilage surface and matrix caused by degeneration (Han et al., 2003). Measurements of cartilage thickness showed very good agreement with thickness estimations based on histology (Han et al., 2003). Cartilage quantification based on OCT signal intensity from the surface and based on surface roughness has been shown to differentiate between intact and degenerated cartilage surfaces (Huang et al., 2011). Also inclination effects have been investigated and found to have a significant influence (Huang et al., 2011). Other OCT studies demonstrated the quantification of cartilage matrix based on OCT backscatter signal homogeneity, irregularity and attenuation. It was found that the derived parameters depend on the degree of cartilage degeneration (Nebelung et al., 2015). Since the promising results of cartilage imaging and quantification based on OCT, the application of arthroscopic OCT measurements has also been investigated and demonstrated its feasibility (Puhakka et al., 2016).
Fourier-transform intrared spectroscopy (FTIR) can quantify the relative PG and collagen concentrations in cartilage. The measurements are performed in transmission on histological sections with high spatial resolution (Camacho et al., 2000). Similar to OCT, a Michelson interferometer is used, but the sample is placed in the recombined light path between beam splitter and detector. The infrared spectrum is acquired and compared to a reference spectrum acquired without the sample. The absorption in specific frequency bands depends on the concentration of certain molecule structures. So, it is known that the Amide I band (wave number 1740 - 1585 cm^{-1}) is related to the collagen concentration and the Carbohydrate band (wave number 1140 - 984 cm^{-1}) relates to the PG concentration (Rieppo et al., 2012; Männicke et al., 2016). By scanning through the histological slides and evaluate the absorption spectrum at each point, images of PG and collagen concentration

can be created and further quantified (Rieppo et al., 2012).

With the broad efforts made to understand the biomechanical behavior of articular cartilage in laboratory settings, several ideas came up to bring biomechanical testing to the in-situ application. The first devices were very cumbersome to use and harmful to the cartilage and bone (Tkaczuk, 1986; Athanasiou et al., 1995). Other groups worked on devices that were designed to be used arthroscopically. Some of them use vibration to estimate cartilage biomechanical competence (Uchio et al., 2002; Appleyard et al., 2001), other methods were based on manually exerted indentation (Lyyra et al., 1995; Laasanen et al., 2002; Niederauer et al., 2004). Duda et al. introduced a hand-held device that performed the deformation of cartilage by a water jet (Duda et al., 2004). All of these methods, except the device introduced by Laasanen et al., derive device-specific stiffness values only and are therefore not comparable to the results of experiments with different devices.
One commercially available device measures streaming potentials (Arthro-BST, Biomomentum (Sim et al., 2014)). These are little currents induced by ionic flow caused by water movements when compressing cartilage. The device is also designed for arthroscopic application. Electrodes in the tip measure potentials and finally provide a device-specific value. It was shown that this value decreases with cartilage degeneration (Abedian et al., 2013).
The state of the art in experimental ultrasound for characterization of articular cartilage is explained at the end of the next section after the ultrasound basics have been described.

2.3 Ultrasound

2.3.1 Physical principles

Ultrasound is a mechanical wave with a frequency beyond the audible range of humans. By definition ultrasound has a frequency above 20 kHz. The technical application of ultrasound, e.g. nondestructive evaluation (NDE), uses a broad range of frequencies from 50 kHz to several GHz (Shull, 2016). In contrast to electromagnetic waves, ultrasonic waves require a medium to propagate. The characteristics of a sound wave propagating through a medium are strongly affected by the material properties of the medium. This correlation of wave propagation behavior and material properties makes ultrasonic investigations very attractive for nondestructive testing in industry and medicine. The features of wave propagation that are of interest are velocity, reflexion, and attenuation (Shull, 2016).
For the following description, we assume sound propagation in a homogeneous, elastic, and isotropic material. Ultrasonic waves are differentiated in *transverse* and *longitudinal* waves. In a transverse wave, the particles oscillate perpendicular to

the direction of the wave propagation. These motions are induced by shear stresses, therefore transverse waves are also called *shear waves*. Based on the required shear stress, shear waves do not occur in low-viscosity fluids or gases. However, in high-viscosity fluids, biological tissue, and solid matter shear waves exist and are of high interest for material characterization as well as in medical investigation (elastography) (Shull, 2016; Ophir et al., 1991; Tzschätzsch et al., 2012, 2015). Most applications of ultrasonic wave use longitudinal waves. There, the particles oscillate in parallel to the direction of sound propagation. This causes a periodic change in pressure and density, thus the longitudinal waves are also denoted as *pressure waves* (Shull, 2016). Mathematically the wave can be described by the linear wave equation:

$$\frac{\partial^2 u}{\partial x^2} - \frac{1}{c^2}\frac{\partial^2 u}{\partial t^2} = 0. \tag{2.1}$$

A solution of this differential equation is a harmonic wave in the form:

$$u(x,t) = u_0 \cos(kx + \omega t), \tag{2.2}$$

where $u(x,t)$ is the time-dependent displacement of a single particle along the dimension x, the wavenumber k and the angular frequency ω are connected via the speed of sound by $c = \frac{\omega}{k}$. The amplitude of the oscillation is u_0 (Shull, 2016).
Assuming the propagation of an ultrasonic wave through a long, thin rod of base area A, the propagation direction should be in parallel to the long axis of the rod. Thus the wave creates periodic spots of high and low pressure and density. These local imbalances causes forces $F_{\text{imbalance}}$ that can be expressed as

$$F_{\text{imbalance}} = \left(\frac{\partial \sigma}{\partial x}\mathrm{d}x\right) A. \tag{2.3}$$

Newton's second law states that an imbalanced force causes acceleration of a mass m according to

$$\begin{aligned} F &= m \cdot a \\ &= m \cdot \frac{\partial^2 u_x}{\partial t^2}. \end{aligned} \tag{2.4}$$

Substituting the mass m by the density ρ multiplied with the infinitesimal volume ($\mathrm{d}xA$) Eq. 2.3 becomes

$$\begin{aligned} \left(\frac{\partial \sigma}{\partial x}\mathrm{d}x\right) A &= m\frac{\partial^2 u_x}{\partial t^2} \\ &= \rho(\mathrm{d}xA)\frac{\partial^2 u_x}{\partial t^2} \\ \frac{\partial \sigma}{\partial x} &= \rho\frac{\partial^2 u_x}{\partial t^2}. \end{aligned} \tag{2.5}$$

Now we can take Hooke's law $\sigma = E\epsilon$ and assume the rod experiences only changes in length but not in diameter, Eq. 2.5 becomes

$$\frac{\partial^2 u_x}{\partial x^2} = \frac{\rho}{E}\frac{\partial^2 u_x}{\partial t^2}. \tag{2.6}$$

This is the same equation as Eq. 2.1, even though the term $\frac{1}{c^2}$ is replaced by $\frac{\rho}{E}$. (Shull, 2016) This gives one of the most important relations between the acoustic property longitudinal speed of sound c and the material properties Young's modulus E and mass density ρ:

$$c = \sqrt{\frac{E}{\rho}}. \tag{2.7}$$

This equation is only valid for the model of *bar wave propagation*, where the bar diameter is small compared to the sound field diameter and therefore the entire cross section of the bar is exited by the wave (Rho, 1996). When considering a material with a geometry way larger than the sound field diameter, the sound wave is not confined laterally, then this model explains the *bulk wave propagation* (Davis, 2000). In this case the sound velocity is related to the bulk modulus B:

$$c = \sqrt{\frac{B}{\rho}}. \tag{2.8}$$

For completeness it should be stated that the correlation between the shear wave velocity c_s and the shear modulus μ follows the same structure (Shull, 2016):

$$c_s = \sqrt{\frac{\mu}{\rho}}. \tag{2.9}$$

Reflection theory

Since this study predominantly evaluates ultrasound signals that originating from reflection, the basics of ultrasound reflection should be explained here. We consider two homogeneous and isotropic materials with a planar interface and a sound wave that propagates from one material into the other. At the interface a fraction of the sound wave gets reflected back in the first material and the remaining part transmits into the second material. The stress amplitudes of the reflected wave R and the transmitted wave T sum up to 1, but R has a negative sign since the reversal of propagation direction:

$$-R + T = 1. \tag{2.10}$$

R is called the reflection parameter and for planar interfaces and perpendicular incident of the sound wave R depends only on the acoustic impedances of both

materials:

$$R = \frac{Z_2 - Z_1}{Z_2 + Z_1}, \tag{2.11}$$

where Z_1 and Z_2 are the acoustical impedances of the of the materials with the definition that the sound wave comes from material 1 and gets reflected from material 2. The acoustic impedance is the product of mass density and speed of sound:

$$Z = \rho c, \tag{2.12}$$

but with Eq. 2.7 it becomes more clear, that the acoustical impedance is a material property:

$$Z = \sqrt{\rho E}. \tag{2.13}$$

From Eq. 2.11 we see that the reflected wave amplitude becomes smaller the closer the acoustic impedances of both materials are. (Briggs, 1992). No reflection occurs when the impedances of both materials are the same. This is important for Study III, where a clear reflection is required from an elastomer-cartilage interface (see 5.2.2).
For the experiments of UBM as performed in Study I and Study II, the ultrasonic pulses were reflected at a cartilage sample or a solid reference sample. Since Study I investigates the effect of surface inclination it needs to be stated here that Eq. 2.11 is only valid for perpendicular incident. For oblique incident at a fluid-solid interface shear effects become important (Briggs, 1992). If the sample material has longitudinal and shear waves, it also has longitudinal impedance Z_l and shear impedance Z_s. They are defined as

$$\begin{aligned} Z_l &= \frac{\rho_2 c_l}{\cos\theta_l} \\ Z_s &= \frac{\rho_2 c_s}{\cos\theta_s}, \end{aligned} \tag{2.14}$$

where θ_l and θ_s are the transmission angles of both wave types. The impedance of the coupling fluid is now also influenced by the angle θ of the incident wave

$$Z = \frac{\rho_1 c_1}{\cos\theta}. \tag{2.15}$$

The relation between sound propagation angles and velocities follows Snell's law:

$$\frac{\sin\theta}{c_1} = \frac{\sin\theta_l}{c_l} = \frac{\sin\theta_s}{c_s} \tag{2.16}$$

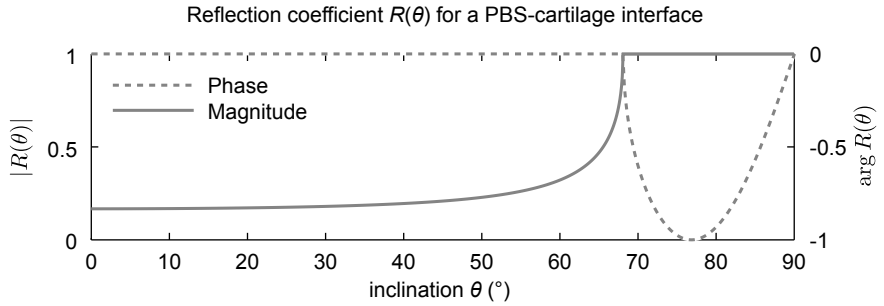

Figure 2.5 – Reflection coefficient $R(\theta)$ for a PBS-cartilage interface. Above an inclination of 68° the entire energy of the incident wave is reflected (total reflexion) and the reflected wave experiences a phase shift up to $-\pi$ at a inclination of 77°. Used cartilage values: $\rho = 1300\,\mathrm{g/cm^3}$, $\nu_l = 1660\,\mathrm{m/s}$ (based on impedance values provided by Leicht and Raum 2008), $\nu_s = 50\,\mathrm{m/s}$ (Lopez et al., 2008).

Finally, the reflection coefficient R is becomes a function of the inclination angle θ (Briggs, 1992):

$$R(\theta) = \frac{Z_l \cos^2 2\theta_s + Z_s \sin^2 2\theta_s - Z}{Z_l \cos^2 2\theta_s + Z_s \sin^2 2\theta_s + Z}. \tag{2.17}$$

For high θ the reflection coefficient $R(\theta)$ can become complex. Above the critical angles for θ_l and θ_s possible effects are total reflection, a longitudinal wave in parallel to the surface, and phase shifts (Briggs, 1992). However, these critical angles are higher than inclination angles used within this study. Figure 2.5 shows $R(\theta)$ for a PBS-cartilage interface. The critical angle is at approximately 68° and in the range of 0-20° inclinations effects on the reflection coefficient of a PBS-cartilage interface can be neglected. As shown later in Study I, inclinations plays an important role on the received signal intensity, but caused by a different reason. It should be noted that for different material interfaces the reflection coefficient $R(\theta)$ can show more irregularities as shown in Fig. 2.5, especially when shear waves play a more important role than in cartilage. The longitudinal and shear transmission coefficients $T_l(\theta)$ and $T_s(\theta)$ behave with similar complexity as $R(\theta)$ but are not explained here in detail because in this study all ultrasound measurements are done in pulse-echo mode and therefore only measure the reflected wave components (Briggs, 1992).

Attenuation

Attenuation, defined as loss of sound amplitude, can be caused by i) absorption ii) scattering iii) divergence of the beam and iv) speed of sound dispersion (Shull, 2016). In some materials speed of sound can be frequency dependent (dispersion). In this case, a short pulse disassembles since the different frequency components, which are first all in phase, propagate with slightly different velocities. With time the pulse

becomes wider and of lower intensity. The divergence of the beam is a geometrical effect and causes an amplitude reduction according to $\frac{1}{r^2}$ for a spherical wave, where r is the distance from the sound source. In the following the emphasis shall be placed on scattering and absorption. Scattering occurs when the propagation medium contains structures that are in the dimension of the wavelength or below. This causes a distribution of the wave components in all directions. Absorption of a sound wave is the dissipation of sound energy into thermal energy. The intensity reduction caused by attenuation can be described by an exponential decay function:

$$I(x) = I_0 e^{-\alpha x}, \tag{2.18}$$

where x is the length of the propagated path. The attenuation coefficient α is defines the attenuation caused by scattering and absorption.

Absorption There are two theories to explain the cause of absorption: by classical absorption or by relaxation processes (Wells, 1975). According to the classical theory, absorption is created by frictional forces between particles when they follow the periodic motion induced by the pressure wave. In fluids the internal friction is described by the viscosity η. The absorption α_a then depends on the viscosity η as well as the frequency to the power of two:

$$\alpha_a = \frac{8\pi\eta f^2}{3\rho c^3}. \tag{2.19}$$

The theory of relaxation processes explains the absorption by relaxation processes that occur since the pressure wave displaces particles out of their equilibrium position. The frequency dependence of this absorption theory can be described as a Gaussian function. As long as the frequency of the wave is low and does not interfere with the relaxation process, the absorption is low. With increasing frequency, the wave interferes with the material relaxation and some energy becomes absorbed. After reaching a maximum absorption at a certain frequency, the absorption decreases with further increase in frequency, since the periodic excitations of the medium is much faster than the relaxation processes. (Wells, 1975).
These theories have only been confirmed by experiments on aqueous solutions or idealized tissues. The results of experiments on biological tissue does not agree with the theories. In soft biological tissues the absorption can be approximated by

$$\alpha = a f^b, \tag{2.20}$$

where a and b depend on the tissue, but b is usually only slightly above 1 (Wells, 1975). Attenuation experiments on polymers reported a frequency dependence with a power between 0.98 and 1.47 (Guess and Campbell, 1995).

Scattering Ultrasound waves scatter when they propagate through inhomogeneous tissue that contains structures whose dimensions are in the range of the wave length. In contrast to specular reflexion, scattered waves propagate in all directions. Assuming a homogeneous tissue contains only one scatterer, than the scattered wave creates an axisymmetric pressure field around the scatterer. The local intensity distribution is depending on the frequency, scatterer size, and scatterer geometry and also from the impedance difference to the surrounding medium (Jensen, 1991; Mamou et al., 2011). Usually an inhomogeneous material contains multiple scatterers. The resulting pressure field is the result of the interaction of all scattered waves, whereby also the scatterer density and their spatial distance gets important (Mamou et al., 2011). In ultrasound pulse-echo imaging, only the scattered components that are scattered back to the transducer contribute to the acquired signal. This signal is denoted as *backscatter*.
To characterize scattering, the product of the scatterer dimension a and the wave number k is used, the so-called ka-value:

$$ka = \frac{2\pi \cdot a}{\lambda}. \tag{2.21}$$

For $ka \ll 1$ the scatterer dimensions are much smaller than the wave length, which causes *Rayleigh scattering*. In the range of Rayleigh scattering the ka-value causes an exponential increase of the backscatter intensity. For $ka \gtrsim 1$ the scatterer dimensions are similar to the wave length or slightly larger. This causes *Mie scattering*, which shows fluctuations of backscatter intensity with increasing ka values (Shull, 2016).

2.3.2 Ultrasound creation and detection

Ultrasound transducers convert electrical signals into mechanical waves and vice versa. This conversion is based on the *piezoelectric effect*. Piezoelectric materials have electric dipole moments between their molecules. Deformation of the material shifts the dipoles and causes polarization at the molecular level and an electric field over the entire material. This piezoelectric effect is reversible and can also have an opposite effect. The *inverse piezoelectric effect* explains the deformation of a piezoelectric material when applying an external electrical field (Demtröder, 2004). The piezoelectric materials of ultrasound transducers are mostly crystals or ceramics.
Besides the commonly known piezoelectric effect, some other effects for ultrasound creation are existing: magnetostrictive (Mattiat, 2013), electrostatic (Haller and Khuri-Yakub, 1996), capacitive (Ladabaum et al., 1998) and photoacoustic effects (Zhang et al., 2008; Cox et al., 2012).
To emit ultrasound pulses the transducer is excited by short electrical pulses. The electrical pulses are so short that the piezoelectric elements start to vibrate in their natural frequency which is determined by the thickness. This vibration is trans-

ferred onto the surrounding material and propagates as sound wave.
Ultrasound experiments are either done in *through-transmission* or *pulse-echo* mode. In through-transmission, one transducer emits a sound wave that is detected by a second transducer that is placed opposite the first one. Then one transducer acts as the emitter and the other as the receiver. Changes of the sound wave allow for characterization of samples placed between both transducers.
Within this study, all ultrasound experiments were conducted in the pulse-echo mode. This uses one transducer that acts as both emitter and receiver. The transducer receives parts of its earlier emitted sound wave that is reflected or backscattered from a sample and propagates back to the transducer (Demtröder, 2004).
In both modes, the ultrasound wave is detected as an electrical signal. The voltage V of that signal is directly proportional to the pressure amplitude P of the sound wave

$$V \propto P. \tag{2.22}$$

The intensity of a sound wave is proportional to the square of the pressure amplitude:

$$I \propto P^2 \propto V^2. \tag{2.23}$$

Intensities in ultrasound signal evaluation are often provided in decibels (dB). Based on Eq. 2.22 and 2.23 the decibel intensity is calculated from

$$\frac{I}{I_0} = 20 \log \frac{V}{V_0}, \tag{2.24}$$

where V_0 is a reference voltage, e.g. 1 V. (Shull, 2016)

2.3.3 Focused and unfocused sound field

Ultrasound transducers are usually made specifically for certain investigations, e.g. imaging of the heart, flaw detection in non-destructive evaluation of materials, or high-frequency scanning. The sound field characteristics are mainly defined by the parameters frequency and aperture diameter as well as the focusing of the transducer.
A single element transducer with a plane aperture face creates an unfocused sound field. This is separated in the near field and the far field. When applying the Huygens-Fresnel wavelet principle to the flat sound emitting area of the transducer, each point of its surface is the source of a spherical wave. All the spherical waves are emitted at the same time and added up, they created the original wave front of the transducer. In the near field the path length differences between different spherical waves are multiples of $\lambda/2$, whereas destructive and constructive interferences occur. This causes spotty intensity fluctuations for what reason the near field is not suitable for the most ultrasound applications. At the begin of the far field, the path length differences are smaller than $\lambda/2$, thus the interferences vanish and the sound

intensity becomes smooth in lateral and axial direction. The far field is characterized by a constant decrease of the intensity with distance from the transducer and by divergence cause by diffraction originating from the emission at the transducer aperture. The length of the near field N can be calculated based on wave length λ and aperture diameter d:

$$N = \frac{d^2}{4\lambda}. \tag{2.25}$$

This equation is only an approximation for the assumption that the wave length is much smaller than the aperture diameter. (Shull, 2016)
Focusing of the sound field is achieved by equipping the transducer with a convex lens, Fresnel zone plate, or liquid-filled lenses, or by using a convexly shaped piezoelectric foil. Phased array transducers use different delays of the excitation pulses to create focused sound fields. A focused sound field is characterized by its focal length, axial beam width (depth of field), lateral beam width (lateral resolution) and the numerical aperture $N.A.$ The $N.A.$ is defined as the sinusoidal of the half subtended angle of the sound field at the focus and basically describes the degree of focusing. The larger the $N.A.$ the more the sound field is focused. A more focused sound field provides higher resolution and sensitivity, in return the depth of field decreases. (Briggs, 1992; Shull, 2016)

2.3.4 Scan modes

In ultrasound imaging common terms for the different scan modes have established. The modes explain which dimension the acquired ultrasound data have. The simplest mode describes a pulse-echo setup of a single-element transducer. The acquired data is the time-resolved signal of the sound waves received by the transducer. Since these one-dimensional data are usually plotted as *amplitude*, this mode is denoted as A-mode (Fig. 2.6 a). Because the recorded signal is an alternating electric current, a single A-mode signal is also denoted as RF signal (from radio frequency).
By adding a spacial component, the data become two-dimensional. This can either be achieved by using multiple single-element transducers arranged in an array or by moving one transducer and acquiring A-modes at regular spacial distances. The resulting data are usually displayed as gray-scale image, whereas signal intensity is converted into *brightness*. Therefore, this mode is called B-mode. It is also often denoted as B-scan when using a scanner to move a single-element transducer as shown in Figure 2.6 b).
The C-mode, or C-scan, corresponds to a B-scan extended by one spatial dimension. In this case, a single-element transducer is moved along a x-y plane and acquires pulse-echoes along the z-direction (Fig. (2.6 c)). Other options are to move an array of single-element transducers or to use a 2D array (Shull, 2016). A special case is the M-mode, which is basically an A-mode recorded multiple times at the same position. This creates a 2D dataset, which can be used to visualize deformation over

time. This mode is often used in medicine to visualize structures of the heart during the phases of the cardiac cycle.
A-, B-, and C-scans are sometimes repeated for different distances to the sample. Then these scans are denoted as Az-, Bz,-, and Cz-scans, respectively.

2.3.5 Ultrasound surface parameters for the quantification of articular cartilage

The quantification of articular cartilage based on ultrasound is currently mainly done experimentally. It has been shown that ultrasound can be used for diverse approaches of quantification. The non-destructive measurement of articular cartilage thickness was one of the first ideas and was shown to be very reliable as long as the estimated speed of sound is correct (Jurvelin et al., 1995; Töyräs et al., 2003). The majority of the approaches aim for the detection of OA-induced changes based on certain parameters. It was shown by Leicht and Raum (Leicht and Raum, 2008) that the depth-dependent acoustic impedance differs for healthy articular cartilage and degenerated cartilage. For this approach, however, the cartilage samples have to be cut, which makes a clinical application improbable.
In contrast, ultrasound surface parameter can be obtained from the intact cartilage. Ultrasound surface parameters have proven their suitability in the characterization of articular cartilage surfaces in several studies (Adler et al., 1992; Chérin et al., 1998; Saarakkala et al., 2004b; Kaleva et al., 2009a; Laasanen et al., 2006). The common surface parameters are the *ultrasound reflection coefficient* R, *integrated reflection coefficient* IRC and the *ultrasound roughness index* URI. Both R and IRC quantify the signal amplitude of the signal from the cartilage surface. However, R is based on the intensity of the RF signal, whereas IRC is calculated in the frequency domain and therefore less susceptible to low SNR. Based on their similarity, excellent linear correlations are expected and have already been reported (Saarakkala et al., 2006). In this thesis, only IRC is used, not R.
Quantification of the roughness expressed as URI is based on the spatial distribution of surface positions within a certain area. This can only be achieved from B-Mode or C-Mode data since they provide an additional spacial dimension. Basically, the roughness is calculated by the root-mean-square of the difference between the actual surface profile and a smoothed representation of the surface.

Calculation of the Integrated reflection coefficient (IRC)

The *integrated reflection coefficient* (IRC) is a measure of the spectral intensity of the reflected ultrasound wave from the surface of the sample. In comparison to scanning acoustic microscopy, where the reflection intensity is derived from the peak of

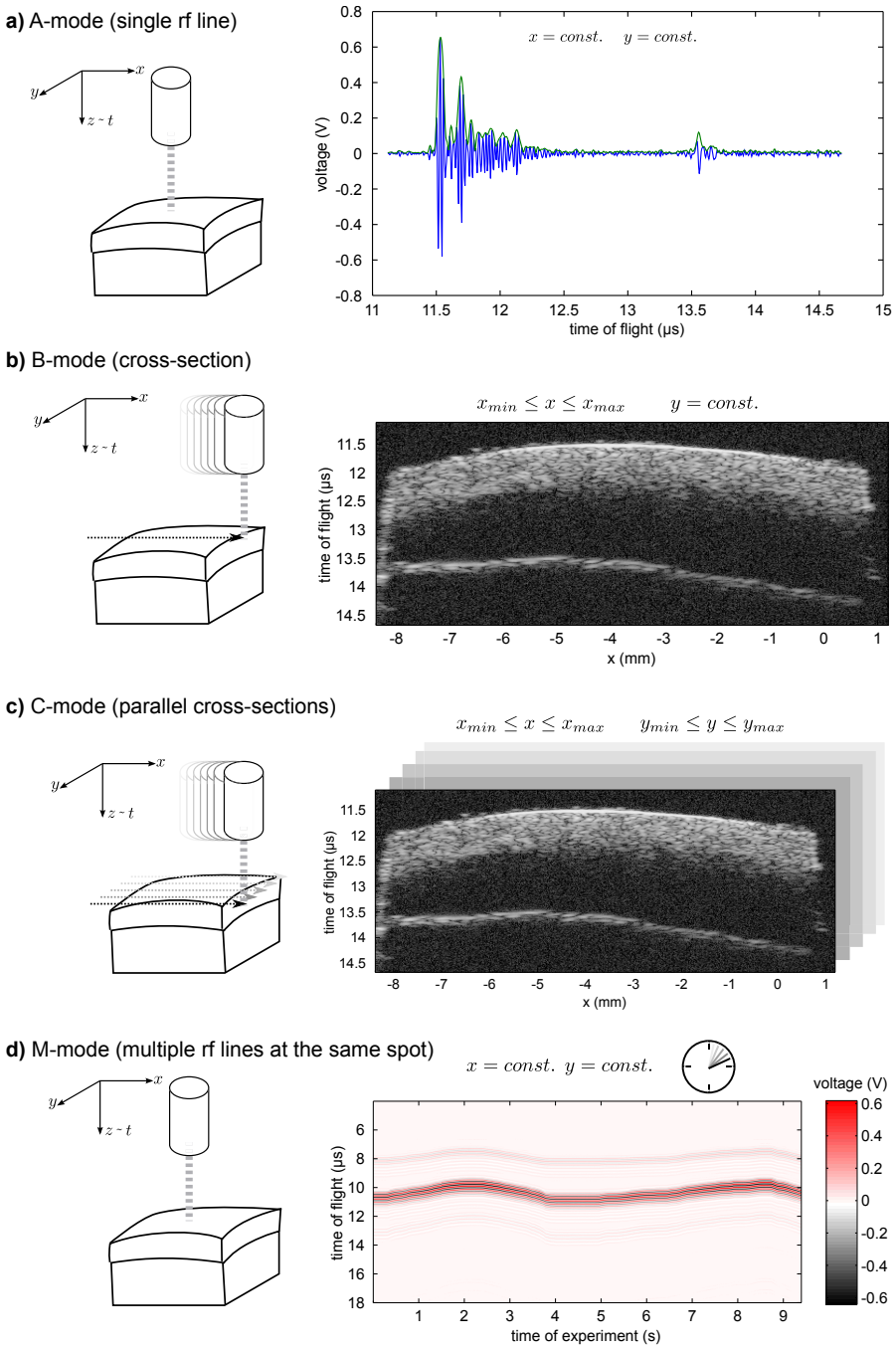

Figure 2.6 – Schematic illustration of ultrasound scan modes. a) A-mode: A single pulse-echo is acquired on a certain position. b) B-mode: The transducer is moved along a line and with constant increment pulse-echoes are acquired. The resulting data are two-dimensional (x and t). c) C-Mode: The transducer is scanned on a two-dimensional plane over a sample and at a defined increment for x and y pulse-echoes are recorded. The obtained data are three-dimensional ((x, y) and t). d) M-mode: Describes repetitively measures of A-modes over a certain time resulting in two-dimensional data (t and $t_{experiment}$).

the envelope of the RF signal, IRC is derived from the mean intensity of the frequency spectrum of a signal window around the surface.
The estimation of IRC includes a normalization to a reference spectrum to exclude influence from the ultrasonic system and defocus effects. Thus, the IRC values become comparable between studies with different equipment and ultrasound transducers. Usually, a time-of-flight matched spectrum obtained from a planar reflector of known acoustic properties is used as reference (Chérin et al., 1998; Kaleva et al., 2009a; Gelse et al., 2010). First, the difference spectrum S_{diff} is calculated by normalizing the spectrum of the surface signal $W(f, x, y)$ to the reference spectrum $S_{\text{ref}}(f, z)$ with the same distance to the transducer:

$$S_{\text{diff}}(f, x, y) = \frac{W(f, x, y)}{S_{\text{ref}}(f, z)}. \tag{2.26}$$

In Fig. 2.7 the steps to obtain the difference spectrum are illustrated. Finally, IRC is obtained from average intensity within Δf, the -6-dB frequency range of the transducer:

$$IRC(x, y) = \frac{1}{\Delta f} \sum_{\Delta f} 10 \cdot \log_{10} \langle |S_{\text{diff}}(f, x, y)|^2 \rangle. \tag{2.27}$$

Additional spectral analysis

The frequency dependence of the surface signals should be distinctly different for reflection and scattering. It has been assessed by a linear fit to the difference spectrum $S_{\text{diff}}(f, x, y)$ (see Eq. 2.26 and Fig. 2.7d):

$$S_{\text{diff}}^{\text{fit}}(f) = m \cdot f + b \tag{2.28}$$

in the frequency range Δf. For $m = 0$, high and low frequency components are distributed equally. When high frequencies dominate, m becomes positive, and vice versa.

Calculation of the Ultrasound roughness index (*URI*)

The URI has been introduced by (Saarakkala et al., 2004b) as the root-mean-squared distance between high-pass filtered surface profile values $z(x_i, y_i)$ and its mean position $\langle z(x_i, y_i) \rangle$ estimated in k scan lines:

$$URI(x, y) = \sqrt{\frac{1}{k} \sum_{i}^{k} \left(z(x_i, y_i) - \langle z(x_i, y_i) \rangle \right)^2}. \tag{2.29}$$

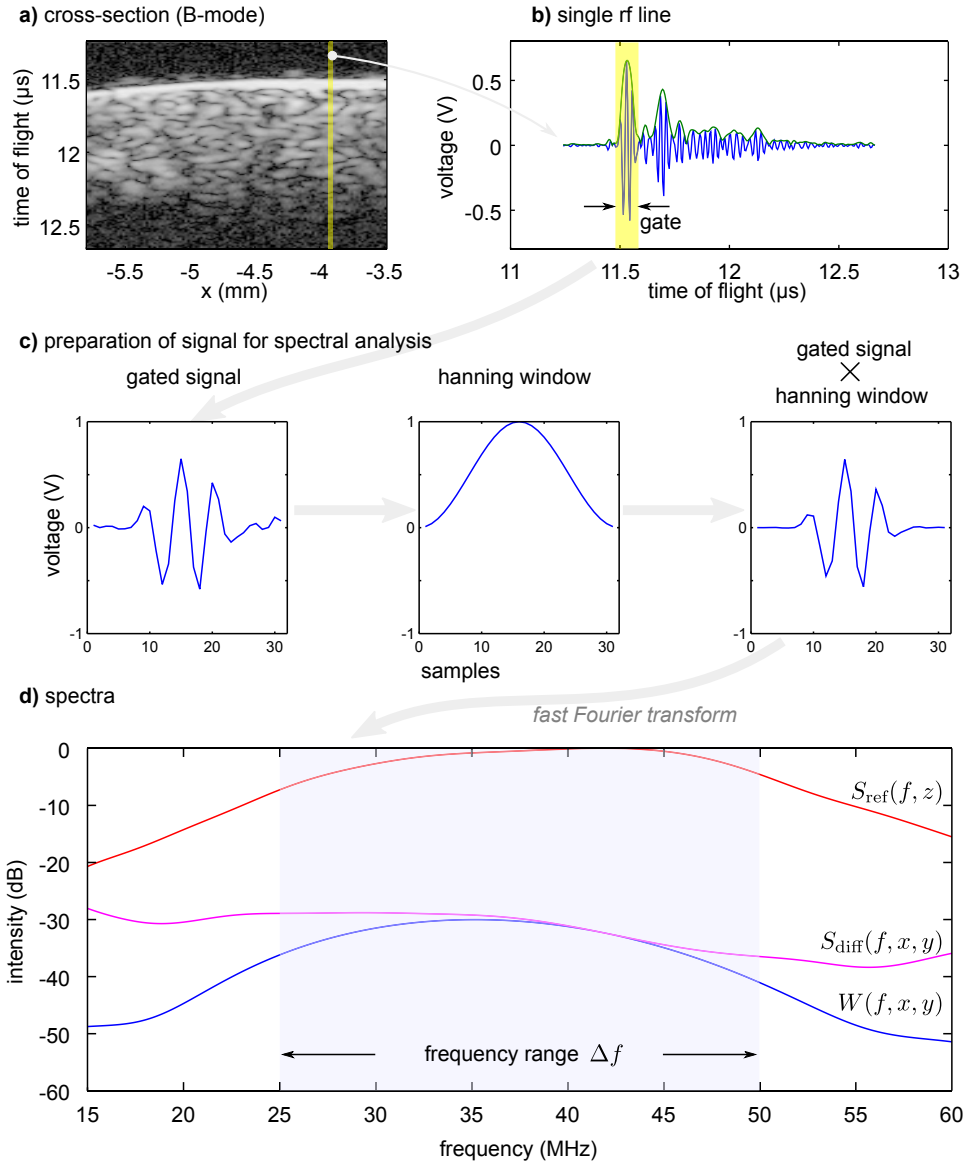

Figure 2.7 – Example of data processing of the surface signal. a) and b) The signal in the time domain. Each rf line is evaluated individually. First the surface is detected and based on the surface position the gate for further evaluation is defined. c) The gated signal is multiplied with a Hanning window function to reduce spectral leakage. d) The spectrum of the sample is normalized to the reference spectrum resulting in the so-called difference spectrum which is then used for the calculation of IRC or the spectral slope m.

Surface parameter under oblique wave incident

The effect of ultrasound beam inclination on the surface parameters IRC and URI at different surface roughness was investigated first by Kaleva et al. (Kaleva et al., 2009a). On intact cartilage, they reported a reduction of IRC and increase of URI with increasing inclination. However, with increasing roughness of the cartilage surface, caused by superficial fibrillation, the inclination dependence of IRC and URI was not observed. They proposed an explanation based on a different contribution of specular reflection and scattering. Similar effects were reported by Chiang et al. (Chiang et al., 1994). They investigated the signal intensity on acrylic samples of different roughness at different angles of incidence. The found a strong inclination dependence that was strongest with the smooth surfaces and reduced for rough surfaces. However, the inclination dependence of the rough samples was very similar, independent from surface roughness. Similar to the knowledge of electromagnetic waves, they suggested the detected signal intensity as the sum of coherent (reflection) and incoherent (scattering) signals as the reason (Chiang et al., 1994). These investigations were performed under highly controlled conditions with a goniometer to align the transducer (Chiang et al., 1994) or the sample (Kaleva et al., 2009a). Characterization of articular cartilage based on IRC and URI have been performed based on single pulse-echoes or B-mode data. The alignment between transducer and sample was controlled manually by checking the amplitude of the pulse echo. Either the "cartilage surface was manually adjusted perpendicularly to the ultrasound transducer by searching for maximum echo amplitude" (Saarakkala et al., 2006) or the region "most perpendicular to the scanning axis" (Laasanen et al., 2005) was selected for evaluation of a 1D scan line.

2.3.6 Backscatter analysis

Whereas in clinical ultrasound imaging with frequencies around 10 MHz or below, healthy articular cartilage appears anechoic (Saarakkala et al., 2006), with frequencies above 20 MHz the upper third of the cartilage layer shows clear backscatter signal (Chérin et al., 1998). It is known that the OA induced changes in the cartilage matrix lead to a different appearance of the ultrasound backscatter in high-frequency imaging (Kim et al., 1995). Therefore, a lot of research has been performed on the quantification of ultrasound backscatter on articular cartilage in order to detect degenerative changes (Chérin et al., 1998; Pellaumail et al., 2002; Wang et al., 2010) and to better understand the origin of the backscatter in cartilage (Männicke et al., 2016; Rohrbach et al., 2017). For data evaluation of the backscatter diverse methods have been used, e.g. spectral methods, amplitude based methods or pattern analysis. Mild degeneration of cartilage does not much effect the ultrasound backscatter qualitatively. But based on sophisticated signal analysis, spectral backscatter parameters

have been proposed that are very sensitive to the first changes of cartilage degeneration (Männicke et al., 2014a,b). Furthermore, it has been shown that the typical backscatter pattern of high-frequency ultrasound in articular cartilage is mainly evoked by the chondrocytes followed by the collagen and its alignment (Männicke et al., 2016). Latest findings indicate, that a regular chondrocyte spacing causes a component of coherent scattering in the frequency range of 23 to 56 MHz. The coherent scattering creates a peak in the frequency spectrum, whose mean frequency depends on the average cell spacing in the superficial layer of cartilage (Rohrbach et al., 2017). These experimental results were found to be in agreement with sound propagation simulations through consecutive interfaces of cells and extracellular matrix (Rohrbach et al., 2017).
Compared to healthy cartilage, an increased backscatter for fibrotic repair cartilage has been reported. Therefore, ultrasound imaging and quantification is also used for characterization of cartilage repair (Laasanen et al., 2006; Gelse et al., 2010).

2.3.7 Challenges to apply ultrasound based quantification in patients

To bring all these methods to the patients, the ultrasound transducer must be placed in close contact with the articular cartilage. When using transcutaneous ultrasound, several limitation are given. First of all, the frequency needs to be lower in order to reach enough penetration depth. But with lower frequency the resolution decreases and there will be no backscatter signal (see Fig. 2.4 d). Based on the bony structures, not all areas of the cartilage surface can be reached and the areas that can be reached, may not be measured from ideal direction, when applying ultrasound from outside of a joint. Furthermore, the cartilage surface will be covered by the synovial capsule and additional soft tissue. Therefore, the surface will not present a distinct interface in the ultrasound data. Consequently, cartilage roughness cannot be quantified correctly. The ultrasound wave has to pass through several layers of soft tissue before being reflected on the cartilage layer. These layers will attenuate the wave differently for each patient. Therefore, a correct reference spectrum as required for spectral quantification cannot be defined. Caused by all of these problems, for precise quantification it is required to bring the ultrasound probe into the joint space. It has been demonstrated that intra-articular ultrasound during arthroscopy is clinically feasible Kaleva et al. (2011); Liukkonen et al. (2014). Even if the ultrasound data are acquired by rotation and not by linear scanning, the same data evaluation methods can be applied in principle. In consequence, the known methods of ultrasound-based quantification of cartilage can potentially be transferred into clinical application.

2.4 Biomechanics

2.4.1 Basics of mechanics

One way to determine the mechanical properties of a material is to exert a force to a sample of the material and analyze the resulting deformation. The required parameters are stress σ, defined as force F acting on the area A, and strain ϵ as the relative change in thickness. Depending on the direction of the acting force with respect to the surface normal, either tensile stress, compressional stress or shear stress is applied. The following explanation is given for compression as mostly used for cartilage testing. In compression the force F acts perpendicularly to the area A of the sample, which results in the compressional stress

$$\sigma = \frac{F}{A}. \tag{2.30}$$

The resulting strain is defined based on the relative change of the thickness d as follows:

$$\epsilon = \frac{d_0 - d}{d_0}. \tag{2.31}$$

Here, d is the current thickness and d_0 is the initial thickness before the force was applied. With this definition a strain of 5% would indicate the reduction in thickness of 5%.
In the basic linear elastic model, the relation between the applied stress and the resulting deformation is determined by the Young's Modulus E:

$$E = \frac{\sigma}{\epsilon}, \tag{2.32}$$

which describes the stiffness of an isotropic elastic material as so-called *Hooke's law*. In other words, in a stress-strain curve the slope corresponds to the stiffness of the material. The strict linear correlation is only found in linear-elastic materials and only for small ranges of deformation. For increasing strain, above the linear range, non-linear effects take over and finally the material deforms irreversible and eventually breaks.
The mechanical behavior of viscoelastic materials, as rubber and cartilage, comprises elastic and viscous behavior. In the resulting stress-strain curve, the stress during the loading phase in above the values of the unloading phase. The area between the loading and unloading curve corresponds to energy that is dissipated during the deformation. This means, a portion of the deformation energy is transferred into thermal energy. In contrast, in purely elastic materials no energy dissipates during deformation, the loading and unloading curves are overlapping.
Tensile or compressional deformation not only cause axial strain ϵ_{axial} (Eq. 2.31), but also transversal strain ϵ_{trans} perpendicular to the acting force. The ratio between

transversal and axial strain, is defined as the Poisson's ratio ν:

$$\nu = -\frac{\epsilon_{trans}}{\epsilon_{axial}}. \tag{2.33}$$

The most materials have a Poisson's ratio between 0 (cork) and 0.5 (ideal elastomer). A Poisson's ratio of 0.5 indicates incompressibility, since the volume is not changing under deformation.
It should be noted, that the most materials exhibit a different behavior under tension than under compression. For biological tissue this is highly reasonable, since the materials highly specialized for certain tasks, e.g. cortical bone is around three time stiffer under compression than in tension (Skedros et al., 1994). Nevertheless, the formulas for the quantification are the same for both directions of deformation, only strain is defined that is starts at 0 under tension. (Gere and Goodno, 2012)

2.4.2 Biomechanics of articular cartilage

The biomechanical behavior of articular cartilage is highly complex and has been investigated for decades (Hayes et al., 1972). Nowadays the triphasic mixture theory is the most accepted theory, which describes articular cartilage as a porous, viscoelastic material whose biomechanical behavior is determined by the interaction between solid, fluid, and ion phases (Lu and Mow, 2008; Lu et al., 2010). The solid phase consists of collagen and proteoglycans. The interstitial water represents the fluid phase and dissolved electrolytes the ion phase. The biphasic model is also often used, comprising only the solid and fluid phases.
The interplay of these three phases results in a complex response when loading or unloading articular cartilage. The PGs attract water caused by there high polarity and in combination with repulsive forces between the negative charged groups the PGs tend to swell. However, the collagen fibers and their arcade-like alignment prevent swelling and are therefore under tensile prestress (Mow et al., 1984). In equilibrium, when swelling force and tensile stress are balanced, the cartilage layer is under steady hydraulic pressure of approximatively 0.2 MPa (Lu and Mow, 2008). Therefore, the equilibrium stiffness of cartilage is the sum of the stiffness of the solid matrix and the osmotic pressure. The density of the fixed charges not only strongly affects compressive resistance of cartilage but also determines the permeability of cartilage for water (Mow et al., 1984). Since the fixed charges attract water, they also cause a high frictional drag against fluid flow, whereas the mechanical deformation of cartilage is strongly time-dependent (Lu and Mow, 2008; Mow et al., 1984). When a constant external load starts to act on articular cartilage (Fig. 2.8 a), a pressure gradient is created and water flows along the gradient, away from the spot where the load is applied. This is a time-dependent process since the water flow is restricted by the attraction from the PGs. Experimentally this behavior has often been expressed by the permeability of cartilage and values in the magnitude

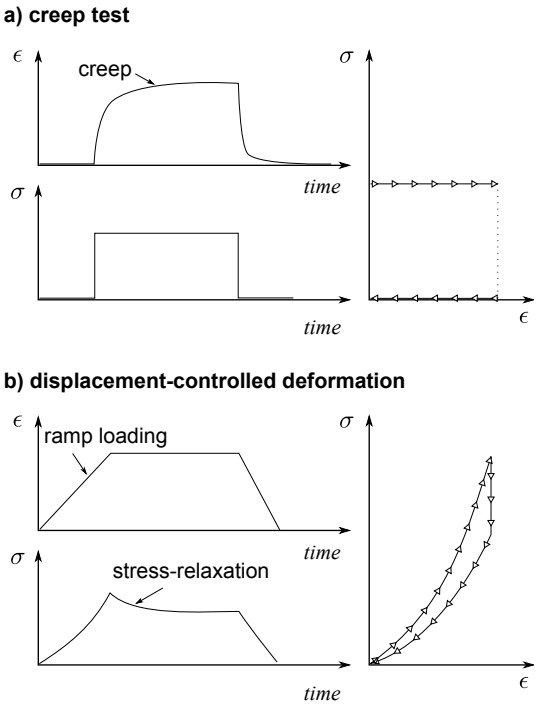

Figure 2.8 – Idealized examples of cartilage loading and testing. a) Creep test with constant load and displacement recording. b) Displacement-controlled test with defined deformation and recording of the resulting force.

of $10^{-15}\,m^4/Ns$ were reported (Saarakkala et al., 2004a). After a certain time, the external load and the internal forces are equalized and water flow and deformation stop. This mechanical process is denoted as *creep* and is physiologically most comparable to steady standing (Lu and Mow, 2008).
In biomechanical testing, the applied load can be measured while deforming the cartilage layer under displacement control (Fig. 2.8 a). During deformation the recorded force increases simultaneously. At that point where the deformation stops, a stress peak is observed, followed by a fast reduction of stress, called *stress-relaxation*. The molecular processes in cartilage can nicely be described with the biphasic and triphasic model: when deforming cartilage is displacement controlled, the required force has to surpass the osmotic pressure, the matrix stiffness, and the frictional drag of water flow. Even when the deformation is stopped, the pressure gradient remains and the water flows continuously until all forces are in balance (Lu and Mow, 2008). Based on this time-dependent behavior it becomes clear that a single value is not sufficient to describe articular cartilage stiffness. The most common values are the equilibrium modulus, the stiffness after relaxation, and the instantaneous modulus, the stiffness during deformation. However, the instantaneous modulus also depends on the deformation speed (strain rate) which should always be considered when comparing stiffness values (Li and Herzog, 2004).

2.4.3 Biomechanical testing of cartilage

Biomechanical testing of articular cartilage can be performed in confined compression, unconfined compression, and indentation (Korhonen et al., 2002). The experiments with confined or unconfined compression require cylindrical samples of osteochondral cylinders or cartilage cut off the subchondral bone in full thickness. The excision of the sample from the articular cartilage layer leads to an altered water flow and to a loss of the integrity of the collagen network. Theoretically, indentation experiments could be performed on the uncovered cartilage of the joint without any further preparation. However, in practice, the samples must be prepared to fit into the rigid setup of the material testing machine. In most cases, they consist of an in-line assembly of an actuator, load cell, and indenter. Therefore, a small sample must be prepared to allow for proper fixation and alignment below the indenter.
The current biomechanical experiments based on compression or indentation are experimentally very sophisticated and allow for detailed investigation of parameters like dynamic stiffness, relaxation behavior, equilibrium stiffness, aggregate modulus, hydraulic permeability, and Poisson's ratio (Mow et al., 1989; Julkunen et al., 2008b; Korhonen et al., 2002; Laasanen et al., 2003). All these experiments have been very important to understand the cartilage biomechanics as well as the mechanobiology of the chondrocytes in detail (Silver and Bradica, 2002; Turunen et al., 2012).
In a clinical setup such biomechanical experiments are too complex and time-consuming. Nevertheless, cartilage stiffness is clinically an interesting parameter since early signs of degeneration are softening or swelling (Hosseini et al., 2013). With time, a reduced cartilage stiffness causes degeneration which eventually progresses to cartilage loss and OA. During arthroscopic evaluation of a joint, the surgeon uses an arthroscopic probe to perform a manual palpation of the cartilage layer. This examination is purely based on the surgeon's subjective perception and his experience and does not provide any comparable measure. Spahn et al. conducted a survey with experienced arthroscopic surgeons. Around 50 % of them agreed that there is a need for improvement in the differentiation between the grades of degeneration. And more than 75 % confirmed that an objective measurement would be "somewhat useful" or even "very useful" (Spahn et al., 2009). Spahn et al. also revealed poor inter-observer reliability of arthroscopic cartilage grading according to the ICRS guidelines (Spahn et al., 2011). Another problem is that for manual palpation the material thickness cannot be taken into account. Therefore, the thinner the cartilage layer is, the stiffer it will "feel". Taken together, there is a clinical need for fast and objective quantification of the cartilage biomechanical quality during open joint surgery or arthroscopy.
Caused by the requirements of the sample's preparation, fixation, and the time needed to conduct a single experiment of conventional biomechanical cartilage testing, these experiments are not suitable for application on an opened joint, neither experimentally nor during surgery.

2.4.4 Strain estimation based on ultrasound time of flight

Ultrasound time-of-flight measurements can be used to determine strain during mechanical deformation (Nieminen et al., 2006). In pulse-echo mode the sound propagates twice through the sample of thickness d before being detected by the transducer. Therefore, the sample thickness equals the half of the product of speed of sound c and required time $\Delta t = t_2 - t_1$:

$$d = \frac{1}{2} c \Delta t. \tag{2.34}$$

The times t_1 and t_2 are the times of the reflections at the sample top and sample bottom, respectively. Based on Eq. 2.34 strain can be estimated during biomechanical testing based on ultrasound time-of-flight:

$$\epsilon_{true} = \frac{c_0 \Delta t_0 - c_1 \Delta t_1}{c_0 \Delta t_0}. \tag{2.35}$$

Here, c_0 and Δt_0 are the initial values before any compression, and c_1 and Δt_1 are the speed of sound and time-of-flight through the cartilage layer at a certain state of load, respectively. When estimating strain based on ultrasound, it is often assumed that the SOS remains constant under deformation, which makes the measures strain independent from speed of sound:

$$\epsilon_{meas} = \frac{\Delta t_0 - \Delta t}{\Delta t_0}. \tag{2.36}$$

However, Nieminen et al. (Nieminen et al., 2006) reported slight changes of articular cartilage speed of sound under mechanical stress. By using a value for the relative speed of sound change $m = c_1/c_0$, equation 2.35 can be expressed as

$$\epsilon_{true} = \frac{\Delta t_0 - m \Delta t_1}{\Delta t_0}. \tag{2.37}$$

To estimate the error caused by m, we can rearrange equation 2.37 to

$$\Delta t_1 = \frac{1 - \epsilon_{true}}{m} \Delta t_0. \tag{2.38}$$

By putting this into equation 2.36 we gain an expression for the effect of m to the measured strain:

$$\epsilon_{meas} = 1 - \frac{1 - \epsilon_{true}}{m}. \tag{2.39}$$

This function is plotted for different m values and different ϵ_{true} in Fig. 2.9. It

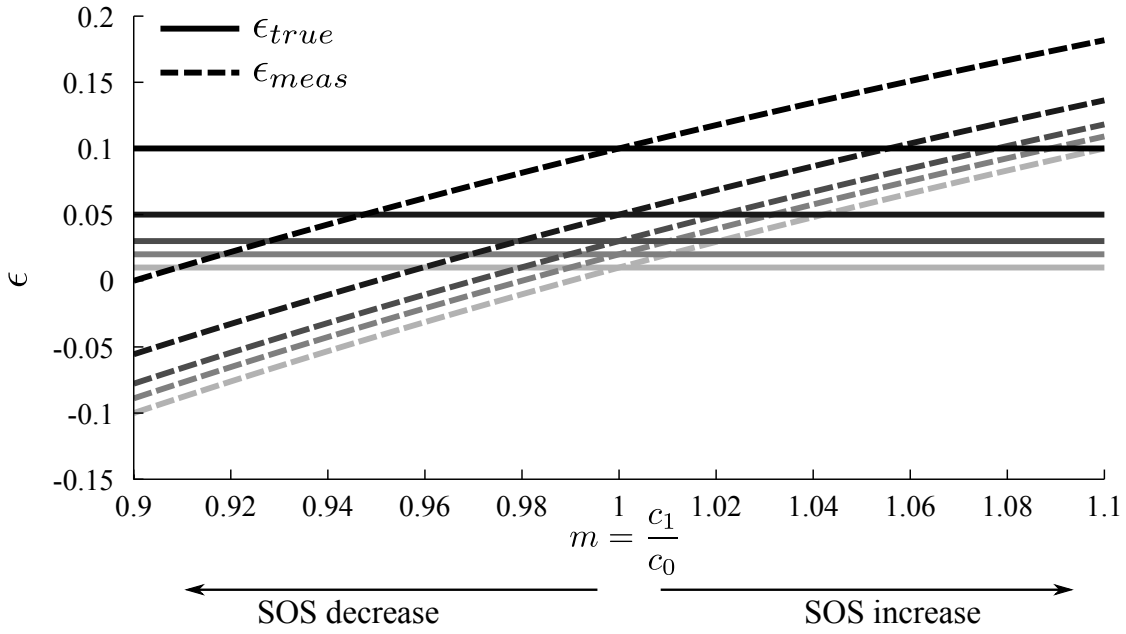

Figure 2.9 – Strain when assuming no speed of sound change ϵ_{meas} and including speed of sound change ϵ_{true} during palpation.

shows that even small changes in speed of sound cause large variations in the estimated strain.
Nieminen et al. (Nieminen et al., 2006) reported speed of sound decrease during ramp compression with 1 $\frac{\mu m}{s}$ of cartilage samples from different species. Later it was shown that the SOS reduction during compression is independent from the strain rate in the range of 0.1 to 10 $\%/s$ (Nieminen et al., 2007). Below 0.1 $\%/s$ the effect is reduced, probably caused by simultaneous relaxation processes (Nieminen et al., 2007). However, the SOS decrease was shown to be strongly correlated to the true strain (Lötjönen et al., 2009). Figure 2.10 is a reprint from Lötjönen et al. (Lötjönen et al., 2009), showing the speed of sound decrease from -1.0 % to -2.2 % for the strain range of 2.4 % to 14.4 % (2.10 A). According to eq. 2.39 this leads to underestimations of ϵ_{meas} from -38.6 % to -13.1 %, which is in agreement with Fig. 2.10 B. So, even the effect of SOS decrease is lowest for small strains ϵ_{true}, the error in the measured strain ϵ_{meas} is highest.
Lötjönen et al. (Lötjönen et al., 2009) demonstrated a correction of speed of sound changes during mechanical load based on their measured values, which led to a reduction of the errors, especially for the low strains. However, after correction, they still had standard deviations in the measured strain ϵ_{meas} of more than 17 % for 2.5 % true strain.
The strong influence of speed of sound change during mechanical load at the mea-

sured strain makes further investigation and experiments necessary. Furthermore, a comparison of these effects on healthy and degenerated cartilage is required, in order to decide if a correction can be applied or would cause more uncertainty.

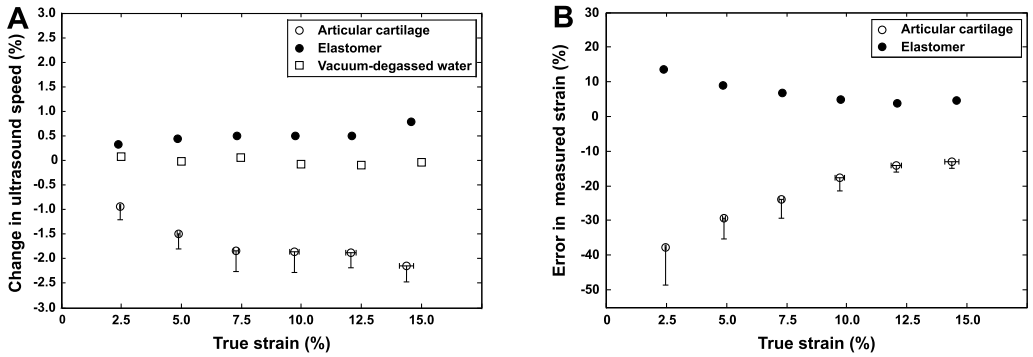

Figure 2.10 – Decrease of speed of sound in relation to the true strain ϵ_{true} (A) and the influence to the measured strain ϵ_{meas} (B). Taken from Lötjönen et al. (Lötjönen et al., 2009), reuse granted.

2.4.5 Hayes correction

In 1972 Hayes et al. (Hayes et al., 1972) published "a mathematical analysis for indentation tests of articular cartilage". It was developed for indentation tests with plane-ended cylindrical indenters and spherical indenters. Their intention was to present a theoretical solution which considered the layered structure of the cartilage-bone sample and the edge effects caused by the indenters with diameters similar to cartilage thickness.
In their analysis, they assume an "infinite elastic layer bonded to a rigid half-space" (Hayes et al., 1972) representing the cartilage layer, with a fixed connection to the subchondral bone. They started with the formulation of a mixed boundary value problem of the theory of elasticity. The infinite elastic layer is deformed by the axial force F acting on an axisymmetric indenter normal to the surface. Shear between indenter and layer are assumed negligible since cartilage presents very low friction. They present an equation (Eq. 2.40) describing the shear modulus G as function of applied force F, Poisson's ratio ν, and indentation depth ω_0. Furthermore, the correction factor κ is correcting for the ratio of indenter radius and layer thickness $\frac{a}{h}$, which is different for each experiment.

$$G = \frac{F(1-\nu)}{4\kappa a\omega_0}. \tag{2.40}$$

For isotropic materials, the shear modulus G and Young's modulus E are not independent from each other:

$$E = 2G(1 + \nu). \tag{2.41}$$

Therefore, the Hayes correction can also be written for the Young's modulus E

$$E = \frac{F(1 - \nu^2)}{2\kappa a \omega_0}. \tag{2.42}$$

This form (Eq. 2.42) of Hayes correction is usually used in indentation testing of cartilage (Zhang et al., 1997; Kleemann et al., 2005; Julkunen et al., 2008a).
At this point, it is important to consider that the response of articular cartilage under mechanical load is not linearly elastic and depends strongly on the speed of deformation. Thus, Young's modulus is not an appropriate parameter for articular cartilage. Therefore, in this work and usually in the literature the term *stiffness* is used.

3 Study I - Ultrasound surface parameters of healthy and degenerated cartilage

The content of this chapter is published in the journal *Ultrasound in Medicine and Biology* (Schöne et al., 2013).

3.1 Background

In the present work, the inclination dependence of the surface parameters was investigated on C-mode scans. Such scans allow for the calculation of the surface inclination in post-processing. This requires detection of the cartilage surface based on the ultrasound signals and the spatial relation of the scan position to reconstruct the surface in 3D. Furthermore, based on the large data set the inclination dependence of the surface parameters can be averaged over a larger number of measurements.
In the following sections, the surface detection and reconstruction will be explained. Subsequently, the calculation of surface inclination is demonstrated that corresponds to the inclination of the ultrasound beam. Then, the estimation of the surface parameters IRC and URI is shown and methods of optimization are proposed. Finally, the inclination dependence of IRC and URI is investigated.

3.2 Materials and methods

3.2.1 Samples

Spherical phantoms

To adapt the convex shape of most of the articulating surfaces, spherical phantoms were used to investigate the inclination dependence of surface parameters IRC and URI. Based on different materials and different finish of the surfaces, three phantoms with different backscatter properties were selected: (i) smooth surface and scattering particles (referred to as phantom 1), (ii) rough surface and scattering particles (phantom 2) and (iii) smooth surface and no scattering particles (phantom

3). The acoustic properties of these phantoms were obtained experimentally (Table 3.1) and found to be close to those reported for cartilage tissue (Leicht and Raum, 2008; Nieminen et al., 2009). According to Chiang et al. (Chiang et al., 1994) the effect of different sample radii should be insignificant as long the focal spot size is small in comparison to the sample radius. The spherical shape of the phantoms allows for measurement of a continuous range of inclination. In the common scan geometry with the transducer moving on a horizontal plane above the sample, the highest point of the spherical phantom always complies with a surface inclination of 0° to the ultrasound beam axis. These spherical phantoms were made from durable elastomer materials enabling homogeneous material properties ensuring the derived surface parameters only depend on the surface inclination. In this respect, they were appropriate cartilage-mimicking phantoms.

Table 3.1 – Properties of the tissue-mimicking phantoms.

Property	**Phantom I**	**Phantom II**	**Phantom III**
Material	Polybutadiene	Polybutadiene	TPU
Mass density [kg/cm^3]	896.56 ± 7.55	971.09 ± 9.85	1305.7 ± 8.19
Speed of sound [m/s]	1516.9 ± 4.2	1462.3 ± 4.8	1616.0 ± 3.6
Acoustic impedance [MRayl]	1.36 ± 0.02	1.42 ± 0.02	2.11 ± 0.02
Diameter [mm]	36	30	46
Surface	smooth	rough	smooth
Scattering (@40 MHz)	yes	yes	no

Cartilage samples

Human cartilage samples were obtained during routine surgery of patients scheduled for knee replacement. A collaborating clinician performed the surgery that includes complete removal of the condylar ends of the femur. From the removed condyles, osteochondral biopsy samples with mild signs of cartilage degeneration (no or partial surface fibrillation) were removed ($N = 26$). Additionally, $N = 12$ punch biopsies were obtained from human cadavers where no cartilage degeneration was expected. Immediately after excision, the samples were stored at -32°C. Before conducting the ultrasound measurements, the samples were thawed and immersed in PBS at 25°C. This procedure was performed in the same way for all samples to maintain comparability. Approval for the experiments was granted by the ethics commission of the Martin-Luther University Halle–Wittenberg, and informed consent for the study was obtained from all human subjects.

Spectral reference and defocus correction

Tissue-mimicking agar-graphite phantoms (Lakshmanan et al., 2012) and a smooth polymethylmethacrylate (PMMA) block were measured in Bz-mode and provide

reference data of pure backscatter signal and planar reflection, respectively.

3.2.2 Ultrasound biomicroscopy

The ultrasound data were acquired at the custom scanning acoustic microscope SAM200Ex (Leicht and Raum, 2008; Gelse et al., 2010). It consists of a three-axis high precision scanning stage, a 200-MHz pulser/receiver (Panametrics 5900PR, Waltham, MA, USA) and a 500 MSs^{-1} A/D-card (Gage CS8500, Gage Applied Technologies Inc., Lachine, QC, Canada). All components were controlled by a custom software (SAMEx, Q-BAM, Halle, Germany) running on a standard personal computer. The scan axis was equipped with a spherically focused 40-MHz lithium niobate transducer (f-number: 2.66, aperture diameter: 3 mm; NIH Resource Center for Ultrasound Transducer Technology, Los Angeles, CA, USA). The spatial and temporal sound field characteristics of the transducer were measured using the wire technique (Raum and O'Brien, 1997). The confocal resolutions in lateral and axial directions were found to be 120 μm and 50 μm, respectively, and the pulse length was 60 ns. The center frequency was 37.5 MHz and the -6-dB range was 25-50 MHz, which corresponds to a fractional -6-dB bandwidth of 65 %.
During ultrasound scans, the samples were completely immersed in a temperature-controlled tank filled with PBS at 25°C. The scan area was selected according to the sample geometry based on coarse pre-scans. In the region of 0° inclination, the distance between sample and transducer was adjusted such that the focus lays slightly ($<$ 1 mm) below the cartilage surface. Fine C-scans were performed with a scan increment of 20 μm in x- and y-direction. The pulse echoes were digitized time-resolved with 200 MSs^{-1} and stored for later offline processing.
Data processing was performed by custom software tools written in C++ and Matlab R2009b (The Mathworks Inc., Natick, MA, USA). For each scan, surface parameter maps were calculated with the same resolution as the scan area. These surface parameters are surface position z (mm), surface inclination θ (°), ultrasound roughness index (URI in μm), integrated reflection coefficient (IRC in dB) and frequency dependence of the surface reflection m (dB/MHz). Since the maps of these surface parameters have all the same size, the parameters can easily be correlated.

3.2.3 Surface position

The reconstruction of the cartilage surface was done in two subsequent steps of surface detection. First, a threshold-based method was applied to the envelope of each pulse echo, providing a simple approximation of the surface position:

$$t_{th}(x,y) = \min_t\{t|s_{env}(x,y,t) > \beta\} \tag{3.1}$$

where $s_{env}(x,y,t)$ is the time-resolved envelope curve of the signal at the position x,y. The variable β is a suitable threshold that was manually set and verified on

4-6 cross-sectional B-mode images individually for every sample.
In the second step, this surface map $t_{th}(x, y)$ was smoothed by a locally weighted scatterplot smoothing filter (Cleveland, 1979), modified for use on 2D maps. This step removed outliers and resulted in a surface map that smoothly followed the positions of the first occurring signals and was denoted as $t_{sm}(x, y)$. The span of the filter kernel was set manually for each sample by adjusting them on cross-sectional B-mode images. The conversion from pulse-echo time of flight to a spatial distance z (called *defocus distance*, whereas $z_0 = 0$ mm is defined as focal plane) was performed with the *a priori* measured speed of sound in the coupling medium ($c_0 = 1540\ \mathrm{ms}^{-1}$).

3.2.4 Surface inclination

The method described here for the calculation of the local surface inclination was developed by Nils Männicke (Männicke, 2018). For every scan position, the surface positions z within a 240 $\times$ 240 $\mu\mathrm{m}^2$ neighborhood were involved to compute the covariance matrix. This dimension was set as twofold the confocal beam width, which ensured the incorporation of a sufficient number of independent measurement points. The local inclination $\theta(x, y)$ was determined as the angle between the major eigenvector of the covariance matrix and the z-axis. The occasionally irregular surface of degenerated cartilage entails locally high variations of θ. Thus, the inclination distribution $\theta_{global}(x, y)$ for an idealized (smooth) surface was assessed by a 2D polynomial fitted to the entire surface map.

3.2.5 Theoretical considerations about the inclination dependency of the detected reflection intensity

Assuming the focused sound field as an isosceles triangle with height s and width $2r$, the base of the triangle represents the transducer surface and the apex the focus of the sound field (Fig. 3.1). The transducer surface and the sound field distribution in the axial plane are assumed as circle of the radius r (receiving and sound field area).
Without inclination (0°), the angle between incident and the reflected sound field is 0° (receiving and sound field area are congruent), resulting in a detection of the entire reflected pulse echo (Fig. 3.1a). By increasing the inclination θ, the angle between incident and reflected sound field increases with 2θ (Fig. 3.1b) and the distance d between receiving and sound field area increases according to:

$$d = s \cdot \tan 2\theta. \tag{3.2}$$

The detected signal intensity depends on the overlapping area of the receiving and sound field areas, which is the sum of two circular segments with the height b:

$$b = r - \frac{d}{2}. \tag{3.3}$$

Therefore the overlapping area A is:

$$A = 2\left[r^2 \cos^{-1}\left(1 - \frac{b}{r}\right) - \sqrt{2br - b^2}(r - b)\right]. \tag{3.4}$$

The detected intensity is can now be written as depending on the overlapping area

$$I \propto 20 * \log \frac{A}{A_0} + I_0, \tag{3.5}$$

where A_0 and I_0 are the overlapping area and intensity at perpendicular incidence ($\theta = 0°$), respectively. For a planar reflector the intensity I_0 depends on the reflection coefficient R, defined by the material the sound wave is propagating in and the material that causes the reflection. It should be noted that R also depends on the angle of incidence of the incoming wave (Briggs, 1992). However, for this simple model here, this dependency should be neglected. Figure 3.1d shows examples of the inclination dependency for different sound field geometries.

3.2.6 Calculation of maps of surface parameters

The basic calculation for the surface parameters URI, IRC, and the spectral slope m was performed similarly to other studies as described in section 2.3.5.
In previous studies, URI has been estimated from single B-mode scans (i.e., from 1D surface profiles). Because the surface profile in this study was measured in two dimensions, it was possible to extend the estimation to 2D. For each (x, y) position, the calculation include the surrounding neighborhood with a kernel size of 120 × 120 μm^2 , which corresponds to the confocal beam width of the sound field. The representative URI value for a sample was obtained from the maximum position of the URI histogram for inclination range $\theta_{\text{global}} \leq 5°$.
Also the spectral parameters IRC and the spectral slope m have been estimated for the 2D map of the scan positions of the C-scans. To estimate the exact gate position for the spectral analysis, I used a sliding window technique to determine for each scan position x, y within a z-interval of 650 μm around the estimated surface position $z_{sm}(x, y)$ the gate position resulting in the maximum mean spectral intensity. The gate width was set to one pulse-length (60 ns) to have the gate of the surface reflection being unaffected by subsequent backscatter signal. The lower limit of the spatial shift between adjacent gates was defined by the sampling interval (5 ns). The position of the time gate resulting in the largest mean spectral intensity

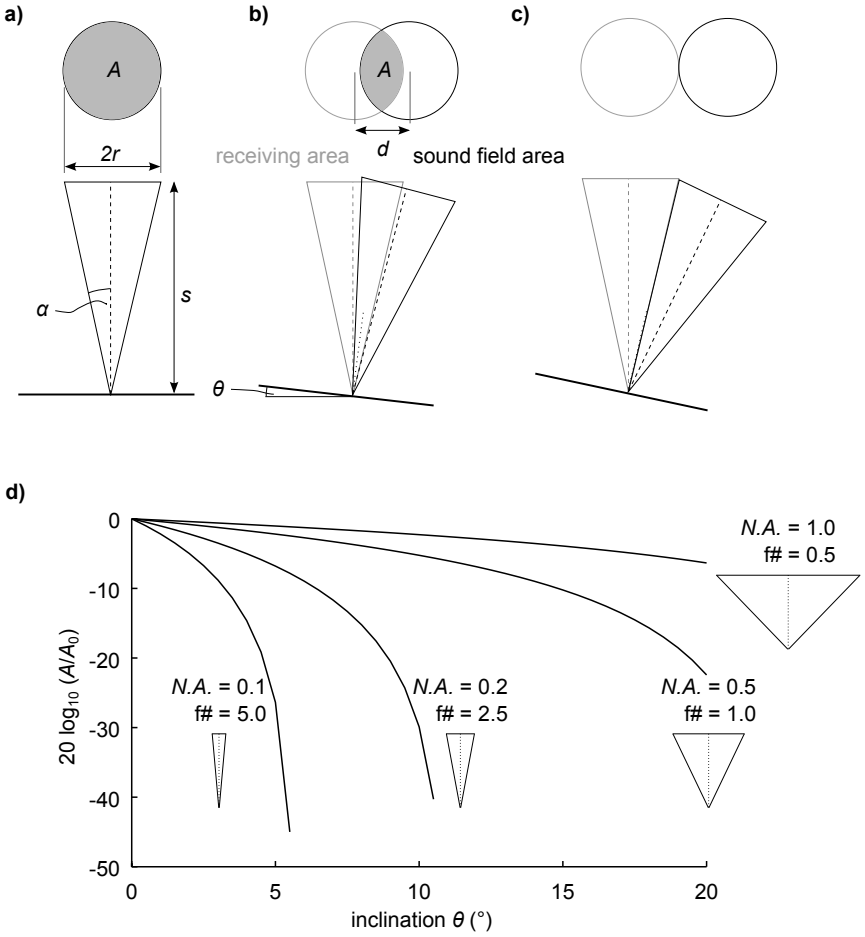

Figure 3.1 – (a-c) The effect of inclination of the sound field (triangle) and the detected intensity determined by the overlap of receiving and sound field areas (circles). d) Examples of inclination dependency for different numeric apertures ($N.A.$). The less focused sound fields exhibit more inclination dependency.

was then used for the calculation of IRC and URI.
When comparing the axial intensity profiles of a purely scattering material (graphite phantom) and a planar reflector exhibits huge differences (Fig. 3.2). Especially in the near field, the intensity drop is remarkable for the planar reflector, whereas the intensity decrease in the scattering material is smoother and only half that of the planar reflector. I postulated the assumption that the reflection of a focused sound field on a planar reflector in the near field includes destructive interferences caused by path length differences between the central and the lateral sound field. Therefore, the summed up signal detected by the transducer will be reduced in amplitude and will display a significantly modified spectrum. Compared to a planar reflector, a cartilage surface is usually not perfectly flat, maybe fibrillated and includes a scattering component. Therefore, the time-of-flight matching signal of a planar reflector is not always good reference for cartilage surface signal, especially when measuring defocused. In this case, the estimated IRC would strongly be affected by the time-of-flight dependent differences between cartilage and the planar reflector and would render the comparability between different measurements impossible. I proposed an alternative approach to avoid such risks. There, only *one* reference spectrum originating from the confocal reflection at a planar reflector is used and the defocus correction is done according to the axial intensity profile of the scattering phantom. A similar approach has been proposed by other authors in the formulations of backscatter coefficients and the extraction of spectral parameters (Insana et al., 1990; Lizzi et al., 1983). The use of one confocal reference spectrum is sufficient if evaluated pulse echoes are within the focus of the transducer (Lizzi et al., 2003). This condition was satisfied in our study, because all analyzed time gates were within the focal zone of the transducer (-6-dB axial intensity distribution of the graphite phantom). We used the confocal reflection of a planar PMMA reflector to measure the reference spectrum $S_{\mathrm{ref}}(f, z_0))$. The reflection coefficient R_{PMMA} = 0.281 and the relative intensity of surface backscatter intensity from a graphite scattering phantom with respect to defocus position z were used to describe the reference spectrum

$$S_{\mathrm{ref}}(f, z) = \frac{S_{ref}(f, z_0)}{R_{\mathrm{PMMA}}} \cdot \frac{I_{\mathrm{graphite}}(z)}{I_{\mathrm{graphite}}(z_0)}. \tag{3.6}$$

The power spectrum $W(f, z, x, y)$ of the sample at the surface position $z(x, y)$ was obtained by averaging the spectra (Insana and Hall, 1990) within a 40-μm neighborhood, which corresponds to 25 waveforms.

$$W(f, x, y) = \frac{1}{N_l} \sum^{l} S_{x_l, y_l}[f, z_{\mathrm{surface}}(x, y)], \tag{3.7}$$

where S_{x_l, y_l} are the individual spectra of the neighborhood of (x, y). The time gate length was set to the 2.5-fold pulse length (150 ns), centered around the detected

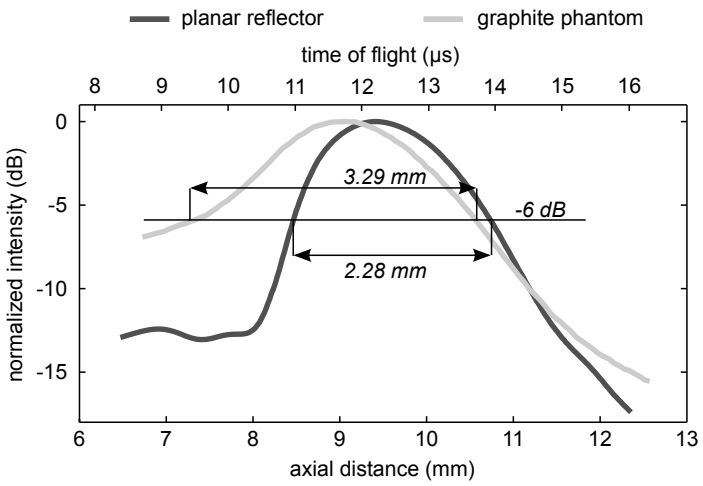

Figure 3.2 – Normalized axial intensity profiles of reflection on planar reflector and backscattering of superficial layer of graphite phantom.

surface position $z_{\text{surface}}(x, y)$ and multiplied with a Hanning window prior to fast Fourier transform. All subsequent steps of calculation the difference spectrum, IRC, and the spectral slope m where based on $S_{\text{ref}}(f, z)$ and $W(f, x, y)$ as described before (sec. 2.3.5).
Finally, based on the map of $IRC(x, y)$ two parameters were extracted within the global surface inclination range $\theta_{\text{global}} \leq 5°$: (i) the median value ($IRC_{\text{median}}$) and (ii) the interquartile range (ΔIRC). Similar to IRC, the median value (m_{median}) and the interquartile range (Δm) were obtained from the spectral slope map $m(x, y)$.

3.2.7 Histology

The histological preparation was performed by an experienced technical assistant. After de-mineralization, paraffin-embedded sections were prepared followed by routine histological processing and staining for Safranin-O and haematoxylin and eosin stain (H&E) (Nieminen et al., 2002; Tunis et al., 2005). Two trained clinicians scored the degeneration of the cartilage samples based on the histology slides individually, according to the modified Mankin score (Table 3.2, (van der Sluijs et al., 1992)). Samples of different scores were revised.

Table 3.2 – Modified Mankin score used within this study (van der Sluijs et al., 1992).

Structure	
Normal	0
Irregular surface, including fissures into the radial layer	1
Pannus	2
Superficial cartilage layers (≥ 6) absent	3
Slight disorganization (cellular rows absent, some small superficial clusters)	4
Fissures into calcified cartilage layers	5
Disorganization (chaotic structure, clusters, osteoclast activity)	6
Cellular abnormalities	
Normal	0
Hypercellularity, including small superficial clusters	1
Clusters	2
Hypocellularity	3
Matrix staining	
Normal/slight reduction	0
Staining reduced in radial layer	1
Reduced in interterritorial matrix	2
Only present in pericellular matrix	3
Absent	4

3.2.8 Statistical analysis

Statistical analysis was carried out using Matlab R2009b (The Mathworks). One-way analysis of variance was used to evaluate differences in the described parameters with respect to the structural Mankin score. Post hoc multiple comparison Tukey tests were used to identify differences among subgroups. Correlations between ultrasonic and histological parameters were analyzed using linear regression. Adjusted R^2 values are provided as measures of the goodness of fit. A significance level $\alpha = 0.05$ was used for all statistical tests.

3.3 Results

3.3.1 Phantoms

The spherical rubber phantoms with different surface structure and different backscatter properties are ideal samples to investigate the effects of surface inclination on the derived surface parameters. Figure 3.3 shows representative cross-sectional B-mode images of the three phantoms and typical pulse echoes of a low and high surface inclination region. The phantoms 1 and 2 show backscatter signal, whereas phantom 3 is free of scattered signal. Reflection is observed in phantoms 1 and 3 as a bright stripe at the very surface of the samples. Phantom 2, with the rough surface,

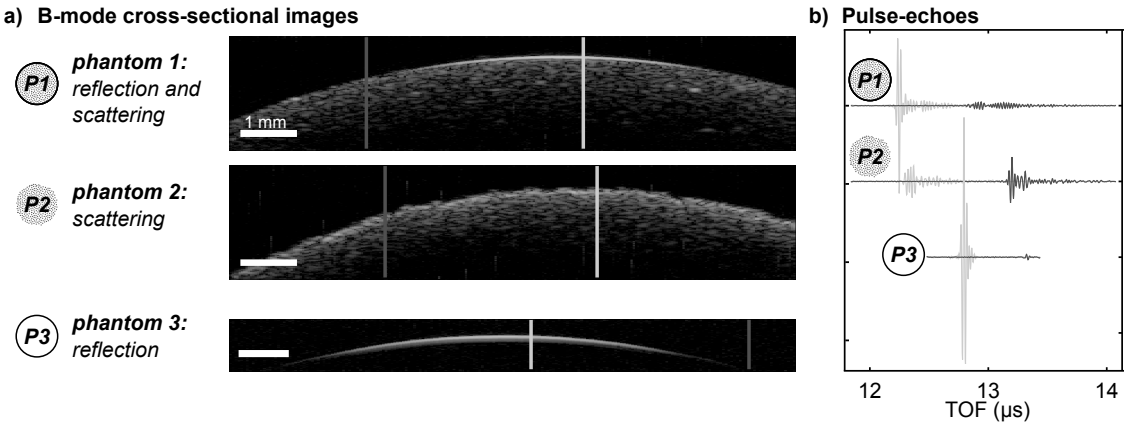

Figure 3.3 – a) B-mode cross-sectional images of the three different phantoms. Phantom 1 exhibits reflection at the surface and backscatter signal, whereas phantom 2 shows only backscatter and phantom 3 only reflection. b) Representative pulse echoes for low and high inclination for all three phantoms.

does not show any reflection. When comparing the pulse echoes in Fig. 3.3 b), the reflected signals are recognized by their huge amplitude. For regions of high surface inclination the reflection vanishes, phantoms 3 shows no further signal. In contrast, the amplitudes of the scattered signals appear to be independent of the surface inclination. Figure 3.4 shows the quantitative inclination dependence of IRC, URI and spectral slope m. The phantoms showing reflection components show higher IRC that is strongly decreasing with increasing inclination (Fig. 3.4 a). In contrast, the IRC of the scattering phantoms is smaller and fairly inclination independent. The URI is smallest for both phantoms with the smooth surface but increased for phantom 1 at high inclination. For phantom 2 the URI values show no inclination dependency (3.4 b). The average values of the frequency dependence m are very similar, however, the variation of m is much smaller for phantom 1 and 3 at a low surface inclination.
All three surface parameters have a transition zone between low surface inclination (0° - 8°) and high inclination (> 10°). For each parameter, first- or second order polynomial fits were conducted to describe the inclination dependence for both inclination ranges qualitatively (3.4).
The theoretical inclination dependency and the comparison to phantom 3 are shown in Fig. 3.5. The calculation of the theoretical curve was performed by usage of the f-number of 2.66 and aperture diameter of 3 mm, provided from the manufacturer of the transducer. The intensity of the theoretical curve was equalized to the IRC of phantom 3 at 0° of inclination. Both curves show a good agreement and the intensity vanishes close before $\theta = 10°$.

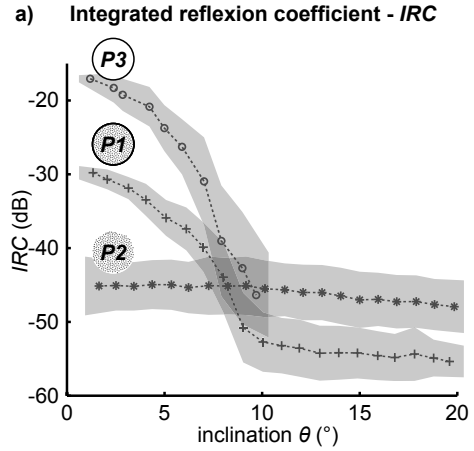

$IRC(\theta)$ =	$0° \leq \theta \leq 8°$	$10° \leq \theta \leq 20°$
P1	$-0.26 \cdot \theta^2 - 29.56$ ($R^2 = 0.98$)	$-0.20 \cdot \theta - 51.37$ ($R^2 = 0.82$)
P2	$-0.17 \cdot \theta - 44.28$ ($R^2 = 0.87$)	$-0.25 \cdot \theta - 42.97$ ($R^2 = 0.96$)
P3	$-0.35 \cdot \theta^2 - 16.45$ ($R^2 = 0.99$)	no signal

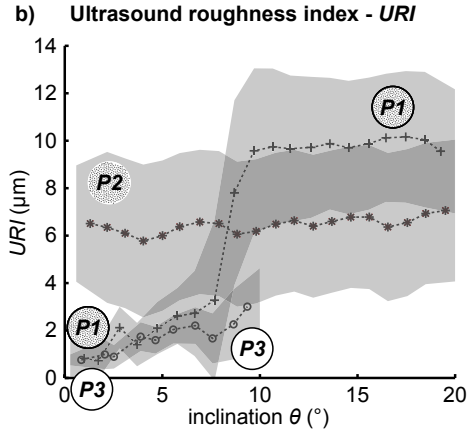

$URI(\theta)$ =	$0° \leq \theta \leq 8°$	$10° \leq \theta \leq 20°$
P1	$0.36 \cdot \theta + 0.43$ ($R^2 = 0.88$)	$0.03 \cdot \theta + 9.35$ ($R^2 = 0.82$)
P2	$0.03 \cdot \theta + 6.14$ ($R^2 = 0.05$)	$0.06 \cdot \theta + 5.78$ ($R^2 = 0.44$)
P3	$0.20 \cdot \theta + 0.65$ ($R^2 = 0.69$)	no signal

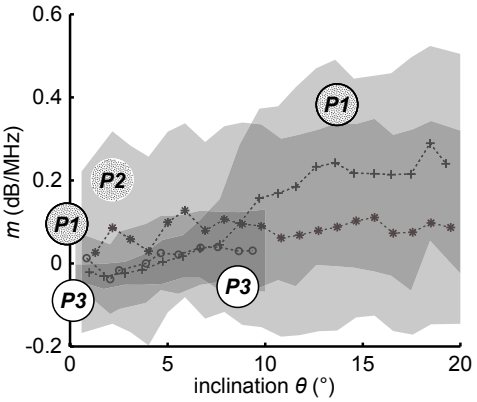

$m(\theta)$ =	$0° \leq \theta \leq 8°$	$10° \leq \theta \leq 20°$
P1	$0.012 \cdot \theta - 0.048$ ($R^2 = 0.90$)	$0.008 \cdot \theta + 0.109$ ($R^2 = 0.39$)
P2	$0.010 \cdot \theta + 0.031$ ($R^2 = 0.31$)	$0.002 \cdot \theta + 0.048$ ($R^2 = 0.09$)
P3	$0.009 \cdot \theta - 0.026$ ($R^2 = 0.49$)	no signal

Figure 3.4 – Inclination dependence for a) the surface reflection expressed as IRC b) the surface roughness expressed as URI and c) the frequency dependence m and regression analysis in the frequency ranges $0° \leq \theta \leq 8°$ and $10° \leq \theta \leq 20°$ for all three phantoms.

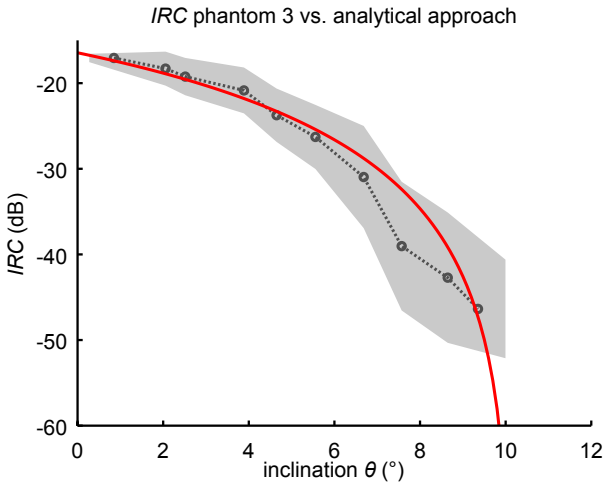

Figure 3.5 – Comparison of the IRC inclination dependency and the theoretical model. The theoretical curve was calculated from the f-number = 2.66 and aperture diameter = 3 mm, provided from the manufacturer of the transducer.

3.3.2 Cartilage

Figure 3.6 shows a cross section and the surface parameter maps of IRC, URI, surface position z, inclination θ and spectral slope m measured on a representative healthy cartilage sample (structural Mankin score = 0). Even though the five surface parameter maps show all different parameters, they have something in common. They all have a central area with more homogeneous values that are different from those surrounding them. This area is the same for all parameters and represents that range where the signal is comprised of reflected and scattered signal components. Based on the knowledge from the spherical phantoms, this is the area of low surface inclination, here confirmed when comparing the inclination map (Fig. 3.6 e). For high surface inclination, above the transition zone, IRC, URI, m and θ change remarkably. Similar to the spherical phantoms, IRC is highest, URI is smallest and m shows less variation for low surface inclination. The surface detection on areas dominated by scattered signal results in more uneven surfaces (Fig. 3.6 c) and finally in more variations of the surface inclination (Fig. 3.6 e).

For degenerated cartilage samples the cross-sectional view and surface parameter maps look remarkably different (Fig. 3.7). The samples are representative of a structural Mankin score of 2 and 4, respectively. In both cross-sectional views, the smooth surface as in Fig. 3.6 a) is vanished and dominated by an irregular interface from PBS to cartilage (Fig. 3.7 a-b). Theses irregularities also affect the derived maps of IRC and URI (Fig. 3.7 c-d). Apparently, both examples do not show any reflection on their surfaces, even at low inclination.
The inclination dependency plots for IRC and URI of representative healthy and

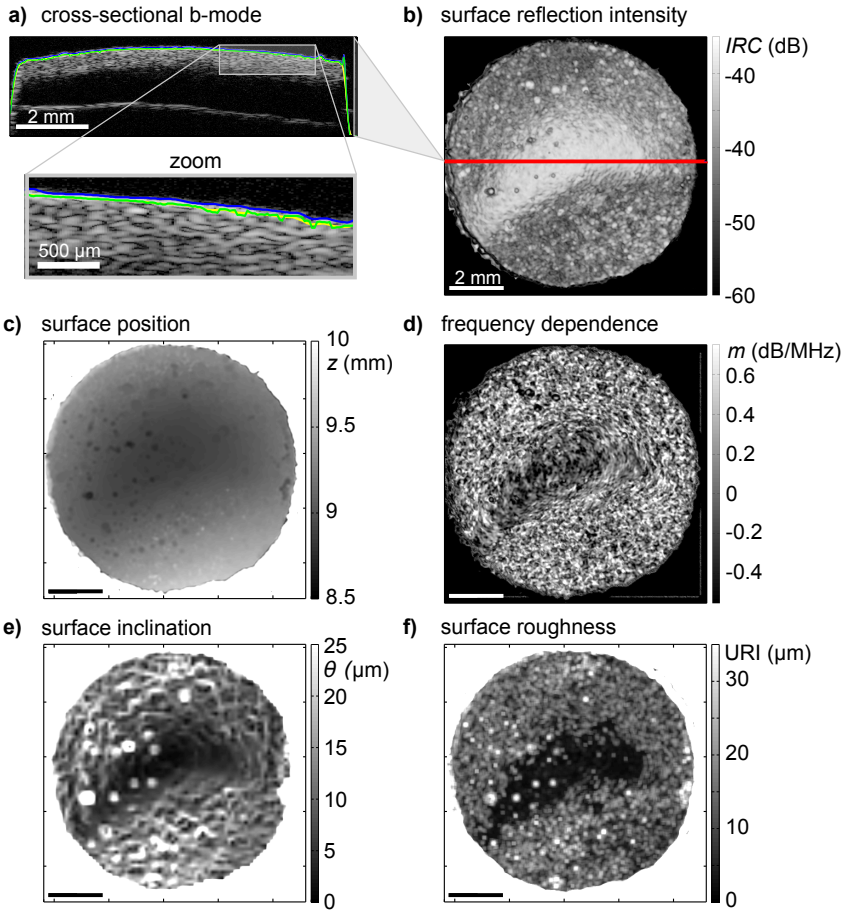

Figure 3.6 – Representative illustrations of a healthy articular cartilage sample. a) Cross-sectional B-mode image and a zoom of superficial area. The three lines represent the position of the detected surface. Blue: t_{th}. Yellow: t_{sm}. Green: z. b) Map of the surface reflection intensity $IRC(x, y)$. The red horizontal line marks the position of the cross-section in a). c) Map of the surface position $z(x, y)$. d) Map of the frequency dependence of the surface signal $m(x, y)$. e) Map of the surface inclination $\theta(x, y)$. f) Map of the surface roughness $URI(x, y)$.

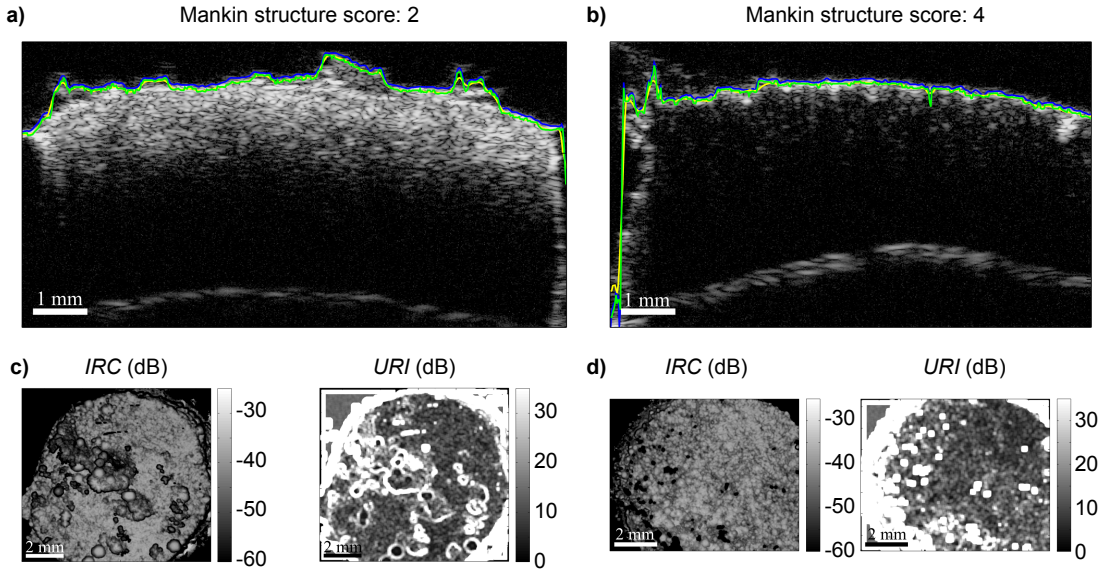

Figure 3.7 – Representative cartilage samples of Mankin structure score 2 (a,c) and 4 (b,d). Cross-sectional B-mode images of cartilage samples (a,b) and the corresponding parameter maps for IRC and URI (c,d). Note the strong differences of the backscatter intensity in the upper third of the cartilage samples.

degenerated cartilage samples (Fig. 3.8) follow similar trends as those found in phantoms 1 and 2, respectively. For healthy cartilage, IRC shows a clear transition from high values at a low inclination towards constant and lower values above 10° (Fig. 3.8 a). URI behaves in exactly the opposite way (Fig. 3.8 c). For degenerated cartilage the transition zone is lost and IRC and URI decrease and increase constantly with increasing inclination, respectively (Fig. 3.8 b+d).
The transition zone of healthy articular cartilage was less sharp than in the spherical phantoms, i.e. the loss of IRC in the range 0° - 5° was less steep in cartilage. Therefore, the inclination range of 0° - 5° was chosen as ideal range for extraction of representative IRC and URI values for the samples. This range is a trade-off between the number of measurement points for averaging and negative inclination effects on the surface parameters. An estimation of the maximum errors induced by pooling the data in this inclination range is given in the following. For phantom 1 with a smooth surface and subsurface scattering the changes in IRC and URI from 0° to 5° were -6.5 dB and +1.5 μm, respectively. For the healthy cartilage sample, these maximum errors are smaller:

$$\begin{aligned} IRC_{5^\circ} - IRC_{0^\circ} &= -3.75 \text{ dB} \\ URI_{5^\circ} - URI_{0^\circ} &= 1.30 \ \mu\text{m} \end{aligned} \tag{3.8}$$

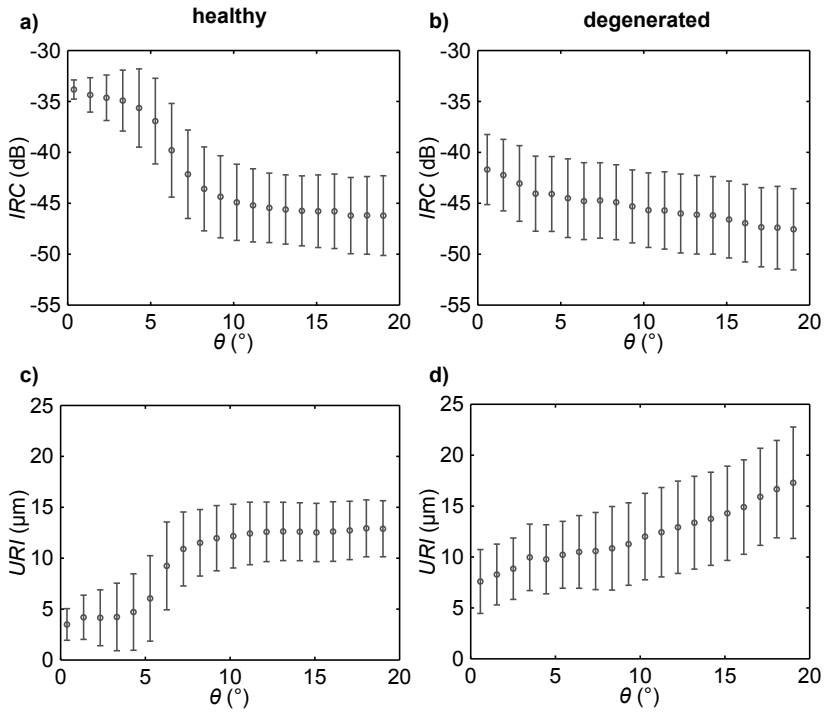

Figure 3.8 – Inclination dependence for IRC and URI for a healthy cartilage sample (a,c, Mankin structure score 0) and a degenerated cartilage sample (b,d, Mankin structure score 4). Plotted are the mean values in small ranges of inclination and their standard deviations.

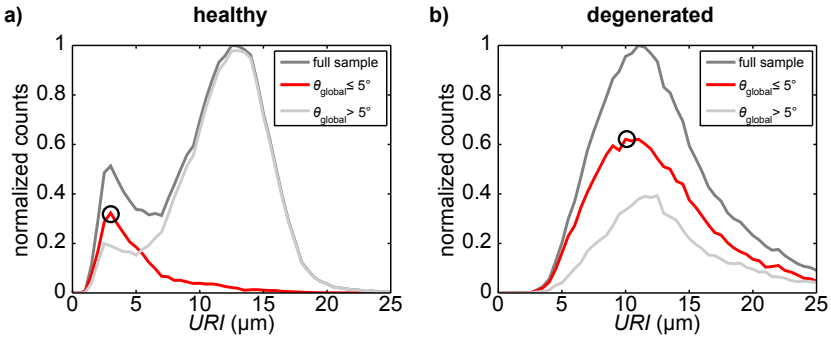

Figure 3.9 – Histograms of URI values and effect of restriction to inclinations below 5 degrees for representative a) healthy (Mankin structure score 0) and b) degenerated (Mankin structure score 4) cartilage samples. Circles highlight the peak position used as representative URI value for each sample.

The bimodal distribution of URI in healthy cartilage becomes very obvious in a histogram. In Fig. 3.9 the URI histograms for a healthy cartilage samples and a degenerated one are shown. Additionally, the histograms for URI at a global inclination below and above 5° are included. In the healthy sample, the peak of low URI is mainly contributed from regions of low inclination (Fig. 3.9 a). In degenerated cartilage a differentiation of two peaks is no longer possible (Fig. 3.9 b).

3.3.3 Ultrasound parameter variations with respect to cartilage degeneration

In total 38 cartilage biopsy samples were evaluated by ultrasound biomicroscopy and histological scoring. The Mankin structure score of these samples was in the range from 0 to 4 (*normal* to *slight disorganization*) with an average of 2.1 ± 1.5. Based on these scores, statistical evaluation was performed. Figure 3.10 shows boxplots for IRC_{median}, ΔIRC and URI_{peak} grouped according to the Mankin structure score and includes F-numbers and highlights for significant different groups. The values for IRC_{median} were significantly lower for samples scored higher than 1 compared to samples scored with 0 or 1 (Fig. 3.10 a). With increasing degeneration and decreasing IRC_{median} the variation within the IRC values within a sample increases, expressed as ΔIRC (Fig. 3.10 b). The URI_{peak} values were significantly increased for samples with a Mankin structure score above 0, however, further degeneration showed no further increase of URI_{peak}. The parameters of the frequency dependence m_{median} and Δm did not show any significant differences between the samples.

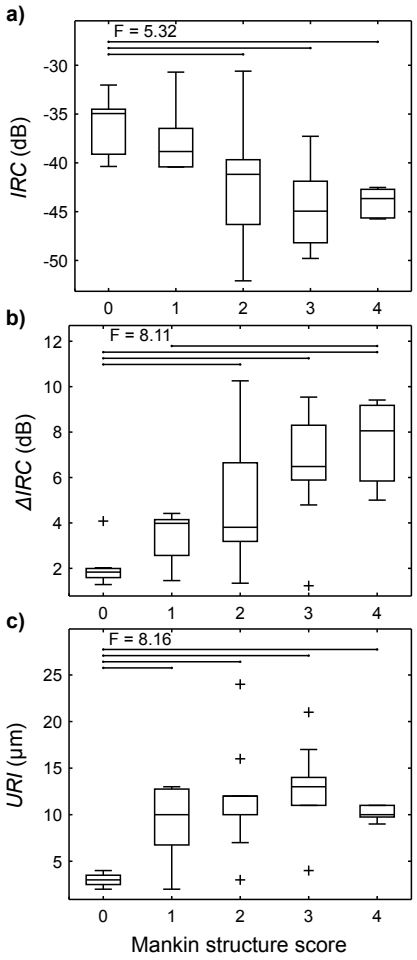

Figure 3.10 – Boxplots and results of ANOVA for a) IRC, b) ΔIRC and c) URI with the structural Mankin score as a categorical factor. Statistical differences between groups are highlighted by horizontal lines ($p < 0.05$). Progressive degeneration is associated with decreasing IRC as well as increasing ΔIRC and URI.

3.4 Disscussion

Within this work, ultrasound base surface parameters describing the acoustic reflectivity (IRC) and the surface roughness (URI) were examined using high-definition 3D ultrasound biomicroscopy (UBM). Both parameters are commonly used for ultrasound-based characterization of articular cartilage samples by high-frequency ultrasound. Tissue-mimicking phantoms were used to investigate the signal composition of reflection and backscatter components and their contribution to the detected signal with respect to the surface inclination. These findings on ideal samples were confirmed on samples of healthy and degenerated articular cartilage. The determination of the surface inclination in post-processing allowed for discrimination of areas of low inclination to improve the validity of the derived surface parameters.

The investigation of tissue-mimicking phantoms revealed, that the signals originating from the sample surface can be composed of both specular reflection and matrix backscatter as previously hypothesized (Kaleva et al., 2009a). Specular reflection can only occur on smooth surfaces. With increasing roughness, the reflection component changes into a scattered component as already shown by Chiang et al. (Chiang et al., 1994). Only the reflected component shows strong inclination dependency. As shown in the experiments and the theoretical description, the loss of intensity with inclination is mainly caused by the scan geometry that does not enable the transducer to receive the reflected component at high inclination. In contrast, the intensity of the backscattered signal shows no inclination dependency in agreement with the scatter theory (Jensen, 1991). When samples show reflection and scattering, the reflected components can only be detected at low angles of inclination. As demonstrated with the spherical phantoms, a reliable estimation of ultrasound surface parameter IRC and URI is only possible at areas that provide reflected signal components. URI and IRC have to be interpreted differently depending on local surface roughness and inclination. For a smooth surface measured at normal incidence, the IRC is related to mechanical stiffness in the direction of the beam axis, whereas URI represents local variations of the surface elevation. With increasing surface roughness or inclination, acoustic backscatter becomes dominant. In the case of complete absence of specular reflections, IRC is proportional to the size and material properties of superficial scatterers. In this case, URI loses its physical meaning, because the detected signal is composed of contributions of surface and subsurface scatterers. Therefore, controlling the inclination is crucial for the estimation of reliable surface parameters.
As shown in the theoretical considerations, the loss of specular components based on surface inclination can be estimated from the aperture of the transducer. This could be used to assess the expected inclination dependency for each transducer individually before the experiments.

Some studies found moderate correlation between IRC and mechanical stiffness of degenerated cartilage (Virén et al., 2012) and cartilage repair tissue (Gelse et al., 2010). From scanning acoustic microscopy a direct relation between reflection intensity and material stiffness is known (Raum et al., 2006). However, as the data of the current work and the interpretation of other literature (Kaleva et al., 2009a) showed, the largest IRC differences are found between reflected and scattered signal. For a material of constant acoustical impedance, the transition from reflection to scattering can either be caused by an increase of inclination or increased roughness. When controlling the inclination, for example as shown within this work, roughness is the main contributor to IRC reduction. Therefore, IRC and URI correlate negatively with each other, as shown by Saarakala et al. (Saarakkala et al., 2004b). Thus, a correlation between IRC and stiffness in cartilage is perhaps an effect of the usual structural changes in cartilage during degeneration. On one hand, surface fibrillation increases the roughness and therefore reduces IRC. On the other hand, softening of cartilage is induced by proteoglycan depletion and loosening of the collagen network. Therefore, stiffness and IRC reduction are measures of cartilage degeneration, but both parameters have no causal relation.

In spot measurements or B-mode scans, the inclination can only be controlled by visual alignment (Saarakkala et al., 2004b). On the irregular tomography of articular cartilage, such a procedure can be difficult and does not allow for estimation of the true local inclination. The advantage of C-scans is their 2D scan plan that allows 3D reconstruction of the surface and estimation of local inclination in post-processing. That allows control of the evaluation of surface parameters with respect to the inclination after the scan. Here, the inclination threshold was set to 5°, which causes errors estimated to be in the order of 1 dB for IRC, which is much smaller than the measured difference between healthy and degenerated samples.
The ultrasound signals from healthy articular cartilage are composed of components of specular reflection and matrix backscatter. The main aim of ultrasound investigations of articular cartilage is to detect early signs of degeneration in a state without apparent surface fibrillation. Therefore, this work focused on the improvement of IRC and URI estimation. The 2D estimation of the surface inclination improved the sensitivity to small URI values by excluding areas of high inclination. Kaleva et al. (Kaleva et al., 2009b) reported average roughness values obtained with optical microscopy (4.8 ± 1.7 μm) and 50-MHz ultrasound URI (5.8 ± 2.1 μm) for bovine cartilage. The URI values for healthy cartilage found in this study were slightly lower (2.9 ± 0.7 μm). The quantification of surface roughness is not simple and the results depend on the methods, equations, and span. The URI parameter is defined by the root-mean-squared difference of a smooth baseline and the actual surface positions. However, this values gives no information about the frequency of surface ups and downs in the investigated span. In the present study, the span dimension was set to the lateral confocal beam width of the transducer. The span

size, however, is a tradeoff between spatial resolution of URI and sensitivity to local irregularities. A larger span will cut off the high URI tail of the histogram but the peak positions will remain. In fact, span variations within the range of 0.5- to 2 times the beam width did not show significant differences in the URI estimates.

The gate size for the calculation of IRC was kept short to reduce incorporation of subsurface scattering. The major difference to the conventional calculation of the IRC was the use of a scattering phantom as an approximation of the axial intensity profile and a single confocal spectrum of a planar reflector for spectral correction. In contrast to the results obtained by this approach, the conventional algorithm resulted in a considerable overestimation of the IRC for surfaces closer in the near field. The use of a scattering medium as a reference reduces phase cancellation effects that occur for reflectors. Because the cartilage surface is not perfectly flat, these effects are highly dependent on surface curvature, beam inclination, and defocus distance. Therefore, the scattering phantom appeared to be a more robust estimator of the axial intensity distribution. The IRC values of the current study measured in healthy human samples were comparable to values found in intact bovine cartilage (-34.2 $\pm$ 4.1 dB; (Kaleva et al., 2009b)). Few data are available for human articular cartilage, and values measured by 40-MHz unfocussed ultrasound in humans (-22.0 dB - 40.7 dB, (Kaleva et al., 2011)) and other species (Virén et al., 2010; Viren et al., 2011; Virén et al., 2012) appear to be higher. A biological reason for differences in IRC can lay in the biomechanical differences between species and anatomical site (Laasanen et al., 2003). However, the systematic effect of specific measurement conditions (frequency, numerical aperture), sample preparation (freeze-thaw cycle) and data processing steps also needs to be considered. When establishing ultrasound surface parameters, e.g. IRC and URI, to clinical diagnostic measures, their estimation needs to be standardized.

In this study, the well-established Mankin grading score was used to assess tissue degradation based on histological cross sections. Since the ultrasound-based surface parameters only refer to structural changes, only the Mankin structure subscore was used, whereas the subscores related to chondrocyte population, proteoglycan staining, and tidemark integrity have been neglected. In agreement with previous studies, a decrease of IRC and an increase in URI have been observed for cartilage samples with increasing osteoarthritic signs (Kaleva et al., 2009a; Saarakkala et al., 2006). The strong differences between samples of healthy cartilage and samples with clear signs of degeneration (Mankin structure score ≤ 2) are also attributed to the loss of specular reflection components caused by increased surface fibrillation. Strikingly, URI was able to significantly differentiate healthy samples from samples of first signs of degeneration (Mankins structure score ≥ 1). However, higher stages of degeneration did not show further increase of URI, caused by the mentioned reasons of unreliable values from a scattered signal. Most important is that

a surface roughness 3 μm and 10 μm can hardly be differentiated by conventional optical arthroscopy. Detecting such early signs of cartilage degeneration supports the potential of ultrasound biomicroscopy as a complementary arthroscopic tool.

4 Study II - Characterization of cartilage repair outcomes

The content of this chapter is published in the journal *European Cells and Materials* as Schöne et al. (Schöne et al., 2016). Some additional information and investigations are added in the context of this thesis. This work was embedded in a large animal study whose main purpose was to prove the safety of a new cartilage repair method. A team of experienced physicians, veterinarians, study managers, and assistants were involved in this study. My part was focused on the acquisition of the UBM data, their evaluation and statistical analysis with inclusion of the scores given by the clinicians.

4.1 Introduction

In the last 10 years there has been high research activity in the field of cartilage repair and several new, mainly cell-based, approaches have been introduced. The characterization of cartilage repair outcomes is usually performed based on the macroscopic evaluation, magnetic resonance imaging (MRI) and histological preparation. For each method, appropriate scoring systems were developed and some of these were validated.
Intraoperatively, the surgeon can assess a cartilage lesion arthroscopically and can score the depth of the defect either according to the Outerbridge score (Outerbridge, 1961) or by the newer and more specific system created by the International Cartilage Repair Society (ICRS, (Buschmann and Saris, 2011)). For the evaluation of cartilage repair outcomes, the specific Cartilage Repair Assessment (CRA) scoring system was recommended in the ICRS Cartilage Injury Evaluation Package. This score is divided into three categories: "degree of defect repair", "integration to border zone", and "macroscopic appearance".
However, it has already been shown that subjective scoring of cartilage lesions can be accompanied by poor inter-observer reliability (ICRS score (Spahn et al., 2011)) or only moderate accuracy (Outerbridge, (Cameron et al., 2003)). Additionally, under arthroscopic evaluation, the thickness of the cartilage layer cannot be assessed unless the bone is exposed locally. For cartilage repair tissue the evaluation of the surface is not sufficient since undesirable malformation of the subchondral bone plate is not visible. However, the importance of the subchondral bone plate as one important

aspect of cartilage repair has been known for several years (Gomoll et al., 2010).
MRI-based evaluation of cartilage repair tissue is recommended by the ICRS according to the 2D Magnetic Resonance Observation of Cartilage Repair Tissue (MOCART) scheme (Marlovits et al., 2006; Ebert et al., 2014). So far, the finding of MRI-based scores in correlation to clinical outcomes is very contradictory (Blackman et al., 2013). Correlations have been found for a single item of the MOCART score and some other MRI-based measures with clinical outcomes after cartilage repair (Blackman et al., 2013; Windt et al., 2013b). However, this correlation was only found for a certain type of repair approach and not for others. Therefore, the current status can be summarized like so: "No current MRI classification system has been shown to correlate with clinical outcomes after all types of cartilage repair surgery" (Blackman et al., 2013) and "there remains a critical lack of conclusive evidence to determine whether morphological MRI is reliable in predicting clinical outcomes after cartilage repair" (Windt et al., 2013a).
The common problem of scoring systems is their predisposition to typical systematic errors, e.g. detection bias, information bias, selection bias, and observer bias (Delgado-Rodríguez and Llorca, 2004). Therefore, the responsible authorities, i.e. the U.S. Food and Drug Administration (FDA) (Food and Drug Administration, 2009) and the Committee for Advanced Therapies (CAT) of the European Medicines Association (EMA) (Eurpoean Medicines Agency, 2010), still recommend patient-based outcome measures such as KOOS (Roos et al., 1998) or IKDC (Irrgang et al., 2001) as primary or co-primary endpoints in pivotal clinical trials, since there is a "current lack of other outcome measures that are both sensitive and objective" (Food and Drug Administration, 2009).
In this work, the feasibility of ultrasound biomicroscopy (UBM) as an objective method for morphometric analysis of cartilage repair outcomes was investigated. UBM scans provide a three-dimensional data set with a spatial resolution in the tens of microns range and carry reflection and backscatter signal from cartilage surface, extracellular matrix structure, and the subchondral bone.
This study uses a custom-made UBM to scan cartilage repair outcomes in sheep one or two years postoperatively. This mobile measurement system allowed for measurements directly after the sacrifice of the animals. The acquired data were evaluated in post-processing comprising surface reconstruction of the cartilage layer in 3D and volumetric evaluation of the former focal defect and the current repair tissue. A shape reconstruction algorithm was used to estimate the initial cartilage surface and cartilage-bone interface in the defect area. We hypothesized that the volumetric parameters obtained from UBM correlate with standard scoring systems. Thus, the comparison to individual categories and cumulative scores of 6 classification systems for gross macroscopy, MRI, and histopathological grading were performed.

4.2 Materials and methods

This study was a conducted within the frame of a prospective, double-blind, randomized cartilage repair study (TVV number 42/08) on 32 adult female Merino sheep.

4.2.1 Surgical procedure

The sheep were treated in accordance with the German Animal Protection Act (*Tierschutzgesetz*, Paragraph 8, Section 1) and authorization was granted by the local legal representative. A bilateral study design was chosen, i.e. left and right legs were treated. The study team is experienced in animal treatment and the surgical procedure has been described before (Zscharnack et al., 2010; Marquass et al., 2011). The preparation of the chronic full-thickness cartilage defects was explained by Hepp et al. (Hepp et al., 2009) and is in compliance with the recommendations of the ICRS for preclinical trials on cartilage repair (Hurtig et al., 2011). Briefly, surgery is done in two stages. In the first operation, bone marrow was harvested from the iliac crest from anesthetized sheep. Additionally, both knees underwent open surgery to create one cylindrical critical-sized, full-depth, focal cartilage defect on the weight-bearing area at each medial femoral condyle. The defect was set by using a 7-mm diameter biopsy punch. Care was taken to avoid damage to the subchondral bone which would be indicated by bleeding. The second surgery was performed 42 days later to treat the cartilage defect of the right knee. After reopening and debridement, the cartilage defect was either treated with an autologous mesenchymal stem cell (MSC) seeded collagen-I-scaffold ($n = 16$) or with a cell-free hyperdense collagen-I-scaffold ($n = 16$). The cartilage defects of the left knee were not treated and acted as controls ($n = 32$).

4.2.2 Sample acquisition and scoring

Half of the animals ($n = 16$) were sacrificed one year after the cartilage repair surgery. After death, the legs were explanted and imaged by standard MRI methods (1.5 T, Avanto Syngo MR B17 with Numaris/4, Siemens, Erlangen, Germany, equipped with a micro-imaging unit) and subsequently scored by an experienced radiologist[1] according to the modified 2D MOCART grade. The applied MR pulse sequences are listed in Table 6.4. MR imaging was performed in 23 minutes for each joint. Following this, the knees were carefully dissected by a surgeon and gross-macroscopically assessed and graded according to the Outerbridge and ICRS-CRA scales (Tables 6.1 and 6.2). Subsequently, UBM scans were acquired as described below. The time between opening the joint and finalizing the UBM scans was always kept below one hour. Phosphate buffered saline (PBS, Biochrom, Berlin, Germany) was used to

[1]Dr. Stefan Conradi of the ZRN Leipzig

keep the exposed cartilage surface moist throughout the investigations. Finally, the samples were fixed by immersion in 4 % formalin (Roth, Karlsruhe, Germany).
Histological preparation began with cutting the condyles centrally through the cartilage defect into two halves. The cut was aligned individually in each sample to always include the apparently worst outcome. Then two histological slides of 45 μm maximum thickness were prepared from one half block in routine fashion by the cutting-grinding technique according to a modified Technovit 9100 protocol (Willbold and Witte, 2010) based on the methyl methacrylate-based embedding resin system. Two experienced pathologists graded the histological images according to the O'Driscoll (Table 6.5), ICRS-I (Table 6.6), and ICRS-II (Table 6.7) scoring systems.
All investigations were done in a blind fashion by the radiologist, surgeon, both pathologists and myself. The remaining animals were killed one year later and the cartilage repair tissue was investigated identically, except for the MRI scan.

4.2.3 Ultrasound biomicroscopy

The ultrasound biomicroscopy (UBM) measurements were performed by a custom and portable device developed by our group. It comprises an industrial computer (ACME II, ACME Portable Machines, Azusa, CA, USA) equipped with an AD-card (CompuScope 14200, Gage Applied Technologies Inc., Lachine, QC, Canada). A spherically-focused, single-element lithium niobate transducer (f-number: 2.66, aperture diameter: 3 mm; NIH Resource center for Ultrasonic Transducer Technology, Los Angeles, CA, USA) is mounted on a compact, external 2-axis scanner unit. The scanner was moved by a DC motor on the x-axis and a stepper motor on the y-axis, controlled by an internal card and an external stepper motor driver, respectively. The ultrasound transducer was excited by an external pulser-receiver (DPR500, JSR Ultrasonics, Pittsford, NY, USA). The 2-axis scanner covered a scan area of 12.5 mm times 9.5 mm, with a resolution of 22.4 μm and 24.9 μm in x and y direction, respectively. The transducer characteristics were measured using planar PMMA reflectors and the wire method (Raum and O'Brien, 1997). The center frequency was 37.5 MHz and the -6-dB range was 25-50 MHz, which corresponds to a fractional -6-dB bandwidth of 65 %. Focus distance and focal length were 9 mm and 3.3 mm, respectively.
The muscles and tendons were removed from the femur followed by removal of the proximal shaft. Then the distal femur was completely immersed in a PBS filled jar that was placed in a water tank whose temperature was kept at $36.1 \pm 0.9\,^{\circ}\mathrm{C}$. The condylar end of the femur was aligned upwards so that the cartilage repair region was on top. The scanner unit was mounted on a construction of two laboratory stand bases connected by rods and bossheads to enable a very flexible alignment. The scanner was oriented in such a way that the scan area included the defect area centrally and parallel to its surface. The distance between the transducer and sam-

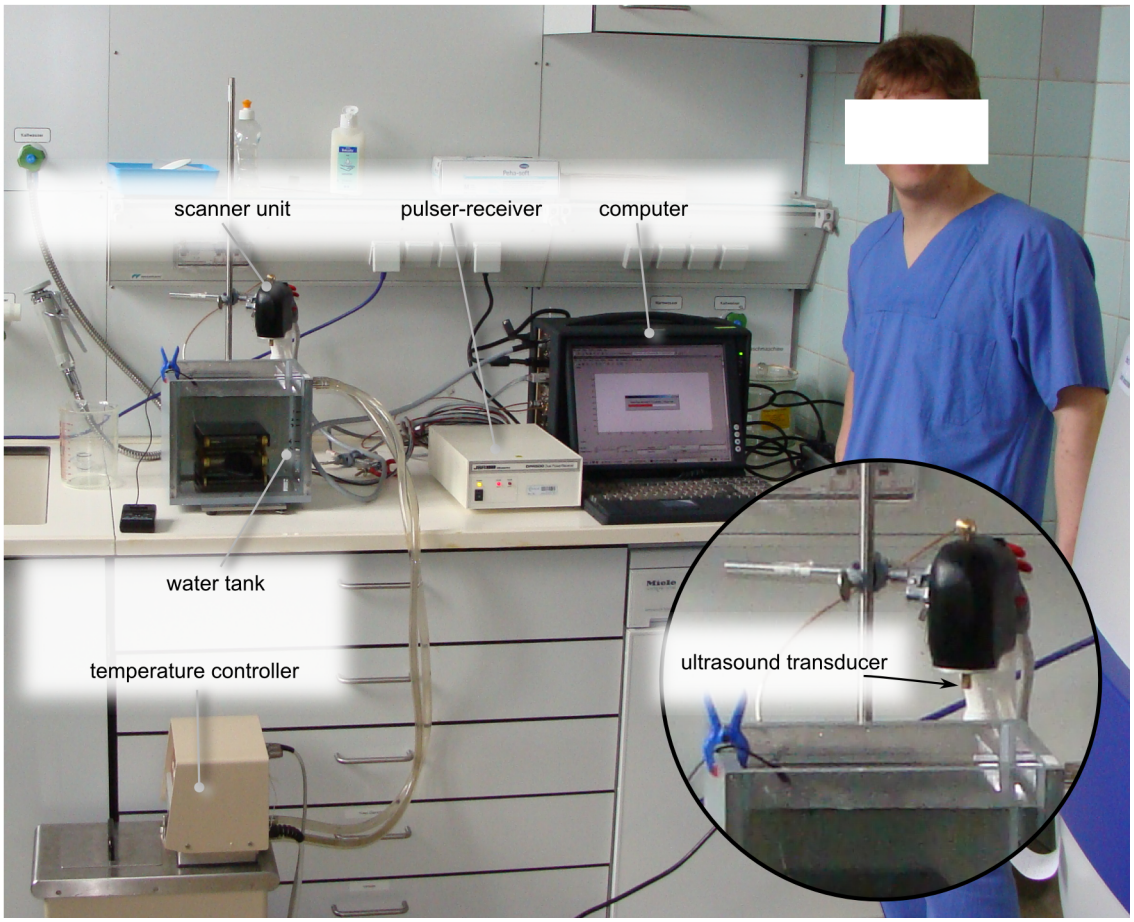

Figure 4.1 – Setup of the UBM in the laboratory next to the room where the sheep were prepared.

ple surface was controlled according to the appearance of the surface signal between 11.0 and 11.5 μs (corresponds 8.5 - 8.9 mm). The alignment was visually controlled with continuous updated B-mode images provided by the UBM system. Then, a C-scan was acquired with a digitization of 200 MS/s at 14-bit resolution and stored for post-processing.
The evaluation of the ultrasound data was performed with custom developed software in MATLAB (The Mathworks Inc., Natick, MA, USA). First, an overview image was computed by the integral of the signal envelope at each scan position (Backscattered Amplitude Integral - BAI (Raum et al., 1998)). The surface detection was done in the same fashion as described in Study I (Section 3.2.3). The required manual input for threshold and filter span were verified at 2D cross-sections and varied between -52 dB to -47 dB and 3 % to 6 %, respectively. The calculation from ultrasound time of flight into the spatial distance was performed by using the

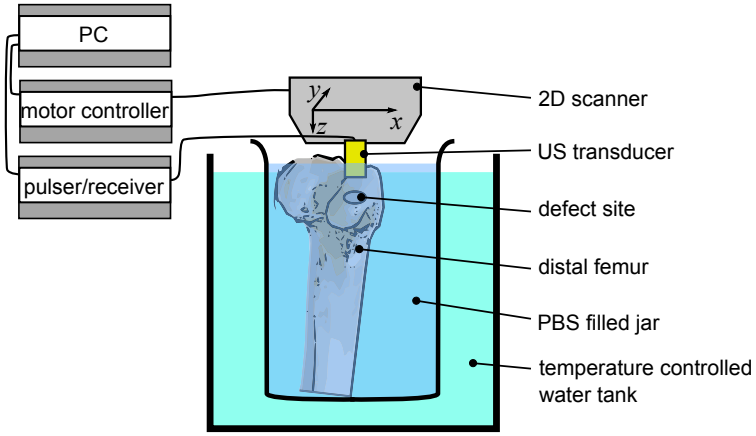

Figure 4.2 – Schematic setup of the measurements on a femur condyle with the custom-made ultrasound biomicroscope (UBM)

speed of sound for PBS at 36°C, 1540 m/s.
The evaluation of these data also comprised the detection of the cartilage-bone interface. Since the signal of the cartilage-bone interface was often weak, the envelope curves of 8 adjacent signals along the x-axis were averaged, followed by detection of the peak below the surface peak. The speed of sound below the cartilage surface was assumed constant with 1660 m/s for the calculation from time-of-flight differences into spatial thickness.
Finally, the maps for cartilage surface and cartilage-bone interface were downsamples from the scan resolution to a coarser grid size of 400 μm in the x-y-plane. This reduced the number of points per map to 744 (Fig. 4.3a-b). This coarse grid was the basis for the upcoming interface estimations and volumetric calculations.
The next steps required manual input that was done blind, i.e. without knowledge of the treatment approach to the current cartilage defect. First, the initial defect boundary was defined by adjustment of a 7-mm diameter circle to fit best to the BAI top view image (Fig. 4.3c). The inner part of the circle excluding a fringe of 0.25 mm, defines the "defect area" and the outer part the "healthy area". Then the automatically defined cartilage surface and cartilage-bone interface were revised and adjusted if necessary. For this, blue markers for cartilage surface and red markers for cartilage-bone interface on the coarse grid, respectively, were displayed over cross-sectional ultrasound images. The user could now adjust the vertical position if required. When a marker could not be assigned to a correct position, the marker was moved to the very top. Thus, the software excluded this marker in further calculations. These steps were first done by a physician and afterward controlled by me.

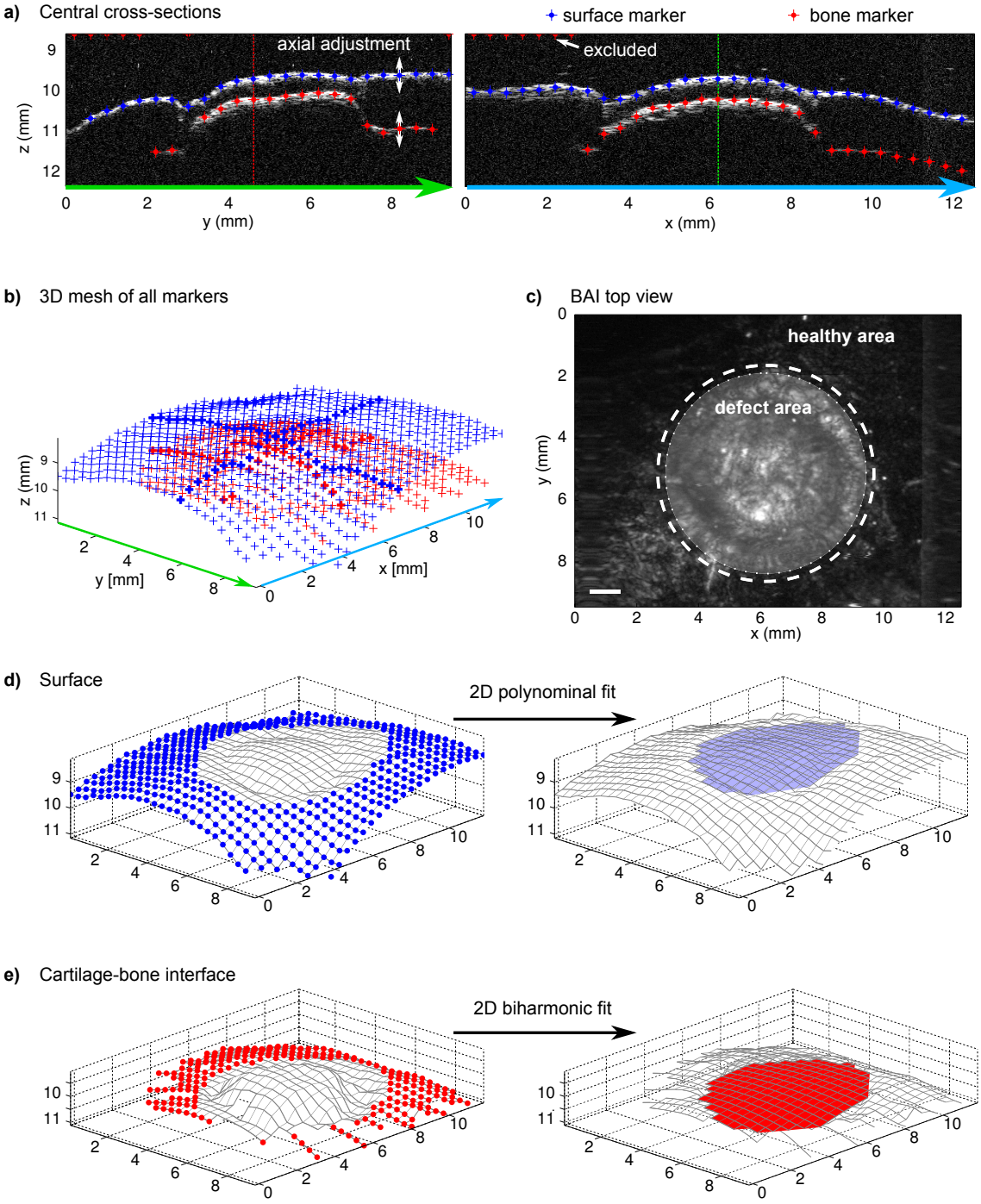

Figure 4.3 – Example of interface fitting of cartilage surface (blue) and cartilage-bone interface (red). a) Two central orthogonal cross-sections with the markers for cartilage surface and cartilage-bone interface. b) 3D visualization of all surface and cartilage-bone interface markers. The bold markers correspond to the cross-sections of Fig. 2a. c) Ultrasound BAI top view image and the manual positioned circle of 7 mm diameter to separate the healthy and defect areas. (d-e) Markers of the healthy area (left) are used to estimate the original surface d) and cartilage-bone interface (e) in the defect area (right).

Interface fitting
For each sample, an estimation of the cartilage layer shape before the defect was set was created. For this, a 2D polynomial fit of the surface position grid on the healthy area was conducted to estimate the original surface in the defect area. The femoral condyles, in general, have a convex shape. This was well represented by a 2D polynomial of 4th order excluding the 3rd order terms. In average, the positions of 372 ± 34 (Fig. 2d) surface markers were used for fitting the surface (Fig. 4.3d). The reduced intensity of the cartilage-bone signal reduced the average number of markers to 254 ± 69 for fitting. Thus, a more robust model was required for the estimation of the initial cartilage-bone interface. This was enabled by 2D biharmonic interpolation (a built-in function of MATLAB).

Calculation of thickness and volumetric parameters
For the defect area, the thickness, as well as certain volumetric parameters, were calculated based on the actual surface position and cartilage-bone interface and the corresponding estimated original interfaces (Fig. 4.4a). The average amount of grid points was 227 ± 28. From the difference between original cartilage surface and initial cartilage-bone interface the minimum, maximum and average cartilage thickness Def.Th were estimated (Fig. 4.4b). By comprising the grid spacing, the volume of the defect Def.V was obtained (Fig. 4.4b).
Cartilage defects and their repair often involves the subchondral bone. Remodeling, irregular structure, loss (cysts) or growth are often observed. Here we quantified the bone volume below the initial bone level as bone loss, BV- (Fig. 4.4c). All tissue above the initial cartilage-bone interface was denoted as defect filling DefFill.V. This could further be differentiated into soft repair tissue, RepT.V (Fig. 4.4e) and bony overgrowth, BV+ (Fig. 4.4f). For inter-sample comparison the volumes of defect filling DefFill.V, repair tissue RepT.V and bone loss BV- were normalized to the individual defect volume Def.V. Note that the parameter abbreviations are based on the system of Parfitt et al. (Parfitt et al., 1987) for bone histomorphometry.

4.2.4 Verification of interface fitting

To verify the interface fitting methods described above, UBM scans of human cartilage samples were used from Study I. Six scans of samples with smooth and intact surfaces were selected. The detection of surface and cartilage-bone interface was conducted in the same way as for the data on cartilage repair outcomes. The scan area acquired from the human samples was smaller than the scans from the current study. Thus, the defect area diameter was reduced to 3 mm and the coarse grid was set to $200 \times 200\ \mu m^2$. A virtual defect was placed centrally to define the defect area and the healthy area (Figure 4.3c). Then the fitted surface and cartilage-bone interface were calculated as described above from 2D polynomial fit and 2D biharmonic interpolation, respectively (4.2.3). The overall intact surface and cartilage-bone interface

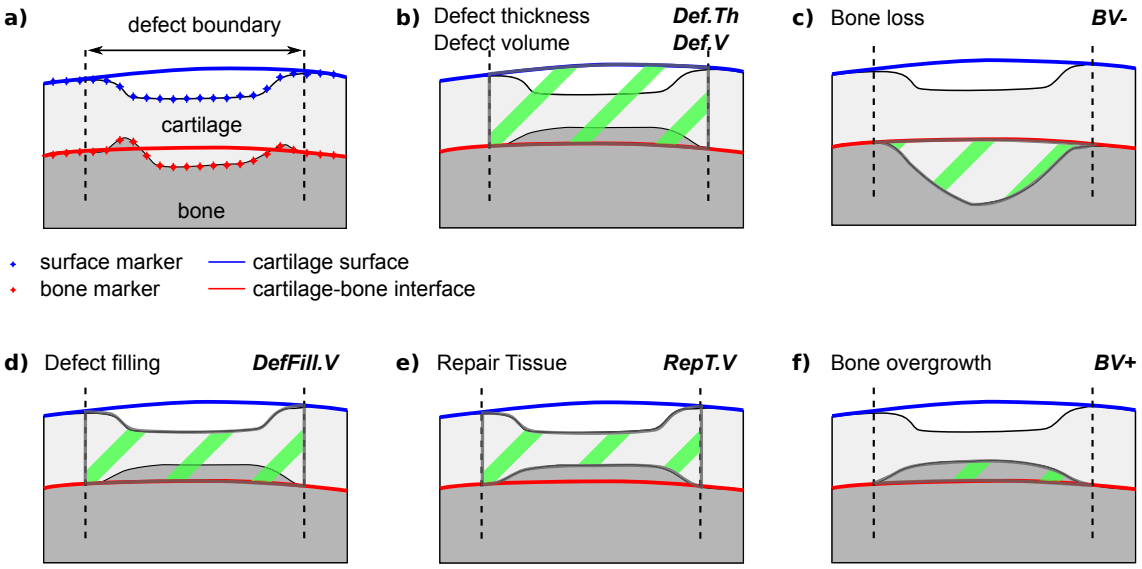

Figure 4.4 – a) Schematic cross sections of cartilage defects as seen in the ultrasound images including the markers and the estimated interfaces. b-f) Schematic explanation of the calculation of the derived parameters.

now allowed for direct comparison of the fitted interfaces with the true interfaces. First, the correlation coefficient r according to Pearson was calculated for the linear correlation between the interface z-positions $z_{true}(x, y)$ and $z_{fitted}(x, y)$ for surface and cartilage-bone interface. Second, the root-mean-square error was computed between $z_{true}(x, y)$ and $z_{fitted}(x, y)$. These calculations were only performed for the interface positions in the defect area. Furthermore, the defect thickness Def.Th and defect volume Def.V were calculated from the spatial differences between the surface and the cartilage-bone interface for the true and fitted positions. These steps from interface fitting to comparison of true and fitted surfaces were repeated for reduced grid resolutions of 400×400 μm^2 and 600×600 μm^2.

4.2.5 Statistical analysis

All statistical analyses were performed in Matlab (MATLAB 2011b, The MathWorks). Most results were found to show non-normal distribution. Thus, non-parametric analysis of variance was performed by Kruskal-Wallis tests with subsequent Mann-Whitney U post-hoc tests to reveal significant differences between groups of a single item of the classification systems. Additionally, tests for statistical differences were performed on the cumulative scores of all classification systems, except for Outerbridge. For ICRS-II the average values of all 14 items were calculated. The correlations between the volumetric UBM data to the cumulative scores were quantified by Spearman's rank correlation coefficient ρ. Based on the multitude

of statistical tests, Bonferroni-Holm correction was applied with a global significance level of $\alpha = 0.05$.

4.2.6 Inclusion and exclusion criteria

The inclusion and exclusion criteria are explained schematically in Figure 4.5a). These criteria were defined before any statistical analysis. The first criterion "entire defect imaged?", verifies whether the entire defect area is covered by the ultrasound scan. If not, the second criteria "reasonable interface fitting?" was consulted. Samples that fulfill the first criteria allowed for reliable estimation of all parameters and were denoted as PP^{abs} ($n = 49$). Samples that dissatisfy the first criteria but satisfy the second criteria still allowed for reliable estimation of thickness and the relative volumetric parameters (defect filling DefFill.V, repair tissue RepT.V and bone loss BV-). They were denoted as PP^{rel}. Failure to meet both criteria led to total exclusion from further statistical analysis ($n = 6$). Statistical values and analysis on cartilage thickness (mean, minimum and maximum) as well as the relative volumetric parameters DefFill.V, RepT.V, and BV+ were obtained from the samples of the set PP^{abs} + PP^{rel} ($n = 58$). The absolute parameters Def.V and BV- were analysed for the samples of PP^{abs} ($n = 49$). Since MR images were only available for the 1-year follow-up samples, 26 samples remained for statistical analysis of the 2D MOCART scores after application of the inclusion and exclusion criteria.
Figure 4.5b-c shows representative images of ultrasound data for the fulfillment or failure of both criteria.

4.3 Results

4.3.1 Verification of interface fitting

The verification was performed on six samples of intact and smooth cartilage layer for three different grid resolutions of 200 × 200 μm^2, 400 × 400 μm^2 and 600 × 600 μm^2 (short: 200, 400 and 600). A representative example is shown in Figure 4.6. The average number of points in the defect area were 177, 44, and 20 for decreasing grid resolutions (200, 400, 600). The comparison of the fitted interfaces to the true interfaces is shown in Figure 4.7. No significant differences for Pearson's r and the root-mean-square error (RMSE) were found between the grid resolutions (Figure 4.7a). Figure 4.7b) shows that the estimated defect volume Def.V was found to be independent from the grid resolution. Only the absolute value of the differences increased, but not significantly. The number of points available in the healthy area for fitting decreased from 1215 to 138 for the surface and from 1050 to 117 for the cartilage-bone interface with decreasing resolution. Therefore these data show that only slightly more than 100 points are sufficient to reliably rebuild the surface and cartilage-bone interface and for estimation of the defect volume, even at the lowest

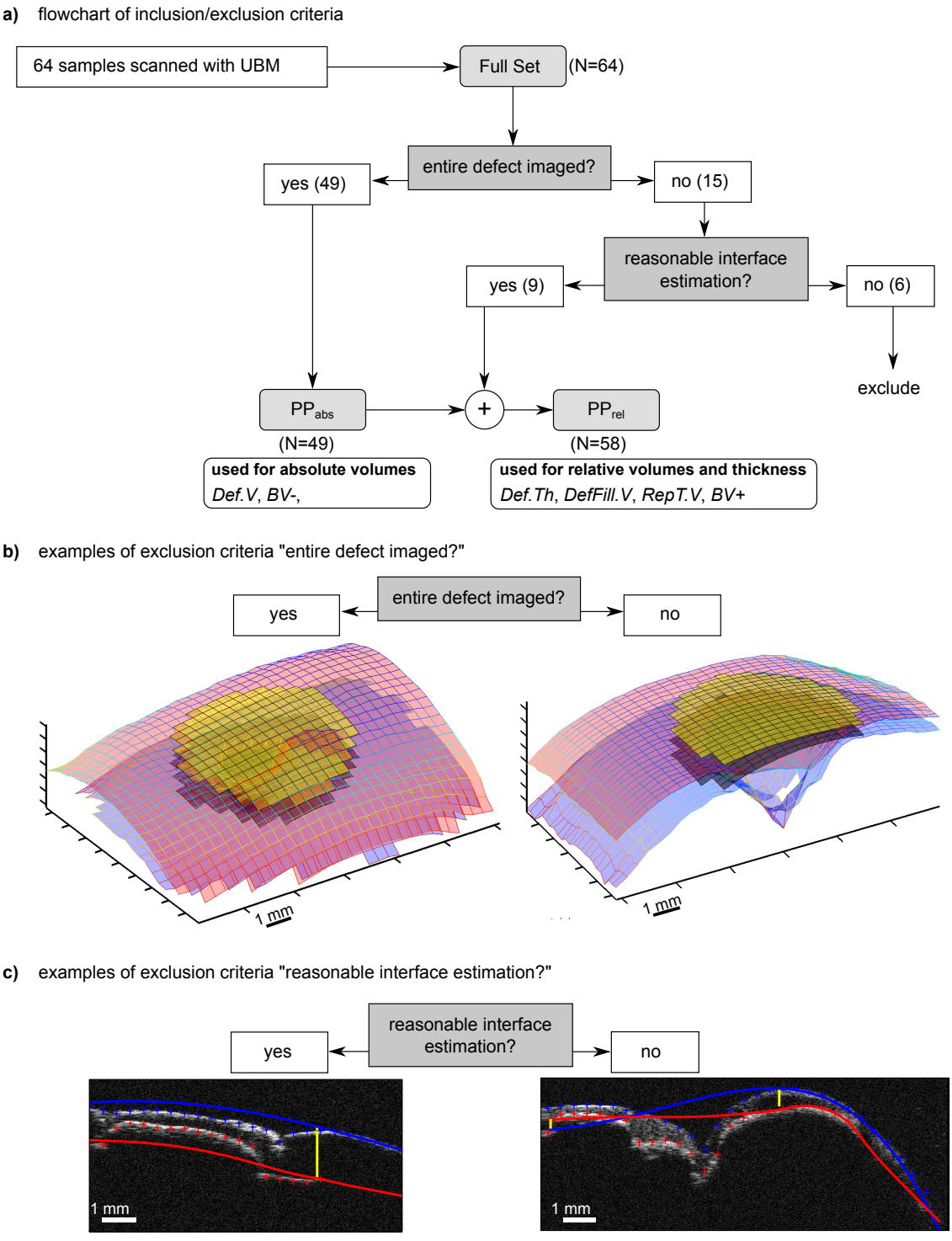

Figure 4.5 – a) Flowchart of inclusion/exclusion criteria. (b-c) Four different samples to demonstrate the inclusion/exclusion criteria. b) 3D reconstructions of the interfaces of cartilage and bone as well as the estimated interfaces at the defect region. The right figure clearly shows that a peripheral part of the former cartilage defect was not acquired. c) 2D cross-sections of the central region with reasonable (left) and not reasonable (right) interface fitting.

resolution. Note that the values for defect thickness behave the same way but are not shown here. Figure 4.8 shows the defect volume Def.V normalized to the values of the finest grid for decreasing grid resolution. The relative changes of the individual samples are very similar for true and fitted origin. With decreasing grid resolution the deviations from the finest grid reach ±4 %.

4.3.2 Comparison of histopathological images to ultrasound cross-sections

The UBM scans consist of several parallel scan lines, each providing a cross-section through the sample. This allows for reconstruction of cross-sectional images in any arbitrary direction in post-processing. Figure 4.9 shows a selection of interesting cases of cartilage repair outcomes. The ultrasound cross-sectional images are reconstructed to represent the same slide as in the corresponding histology slides.
Figure 4.9a) shows a photograph of a repair outcome with peripheral good filling but with a deep cyst in the center. The histological images and the ultrasound images indicate bone overgrowth in the regions of good defect filling. Please note, the histological slides do not represent the true seriousness of the cyst. Only the toluidine blue-stained image shows a small fraction of a gap. Apparently, the final histology slides were not obtained from the central defect region. Two ultrasound cross-sections were reconstructed - one centrally through the defect and one with 1.5 mm distance. They show repair situations with remarkable differences. The central cross-section represents the full dimensions of the cyst of approximately 2 mm in depth and diameter. In contrast, the shifted cross-section shows an almost filled defect and subchondral overgrowth and is therefore similar to the hematoxylin and eosin (HE) stained histology slide. Apart from this, the ultrasound cross-sections show pronounced backscatter from the repair tissue, whereas the surrounding hyaline cartilage is free of backscatter.
A deeper cyst is shown in Figure 4.9b. As indicated in the histology slide, the cyst is filled with soft tissue and the dimension increases below the subchondral bone plate. The ultrasound data are not able to visualize the cyst below the bone structures. Only the not closed subchondral bone lamella is an indicator that the cyst progresses deeper.
A cyst that is totally covered by subchondral bone is shown in Figure 4.9c. Again, ultrasound imaging is not able to visualize structures below covered by bone. Only the breach of the cyst through the bone plate was found and acts as an indicator for a subjacent cyst.
Figure 4.9d shows a defect that is totally empty and the subchondral bone is exposed. The histology slide indicates that the superficial structure of the subchondral bone is changed in the defect area, possibly caused during the first surgery. The ultrasound cross-section shows increased signal intensity from the subchondral bone when not covered by attenuating soft tissue. Furthermore, the bone level in the

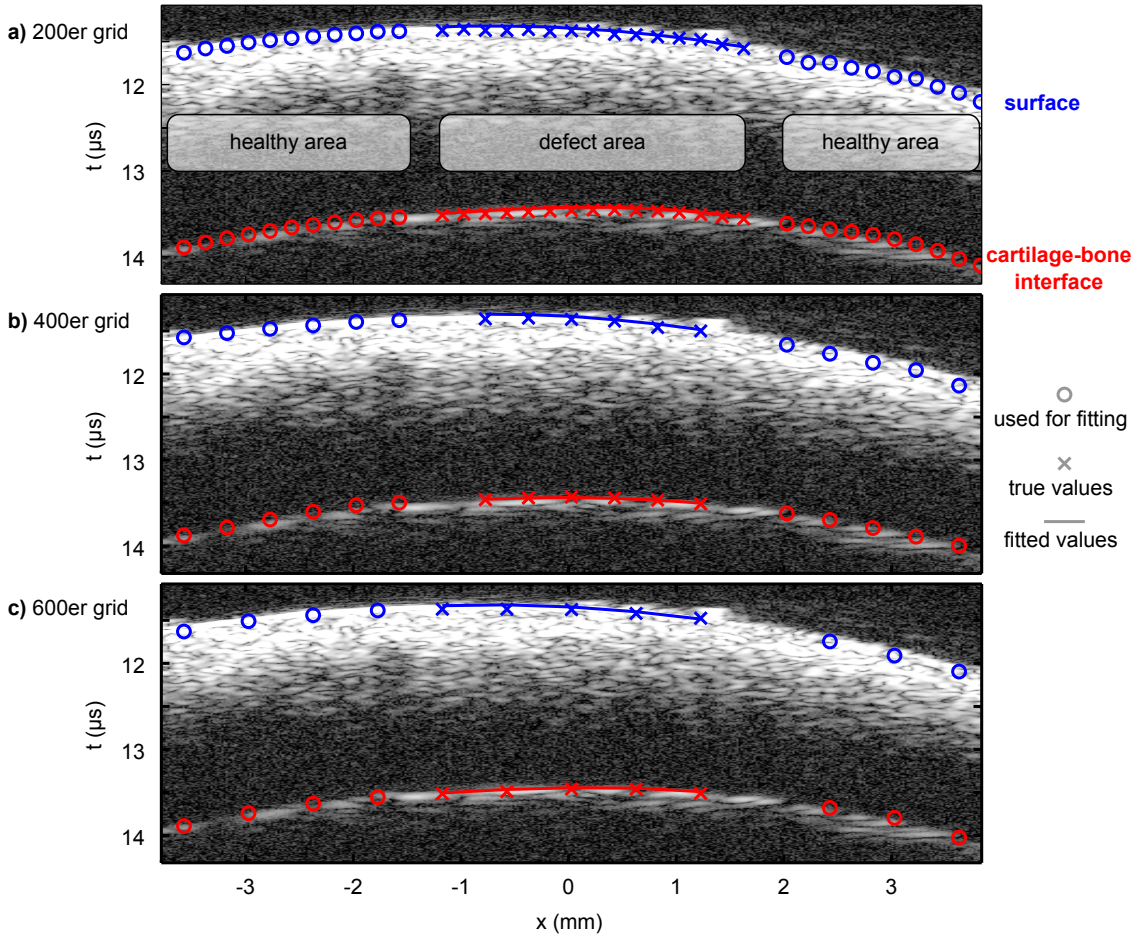

Figure 4.6 – Visualization of surface and cartilage-bone interface markers for verification experiments on a representative intact cartilage layer. a-c) Shown are the same data with different resolutions of the grid. Round markers are used for fitting, the crossed markers represent the true interfaces, and the solid line shows the fitted interface. Note that this is only a 2D cross-section view of a map of markers in the $x - y$ plane.

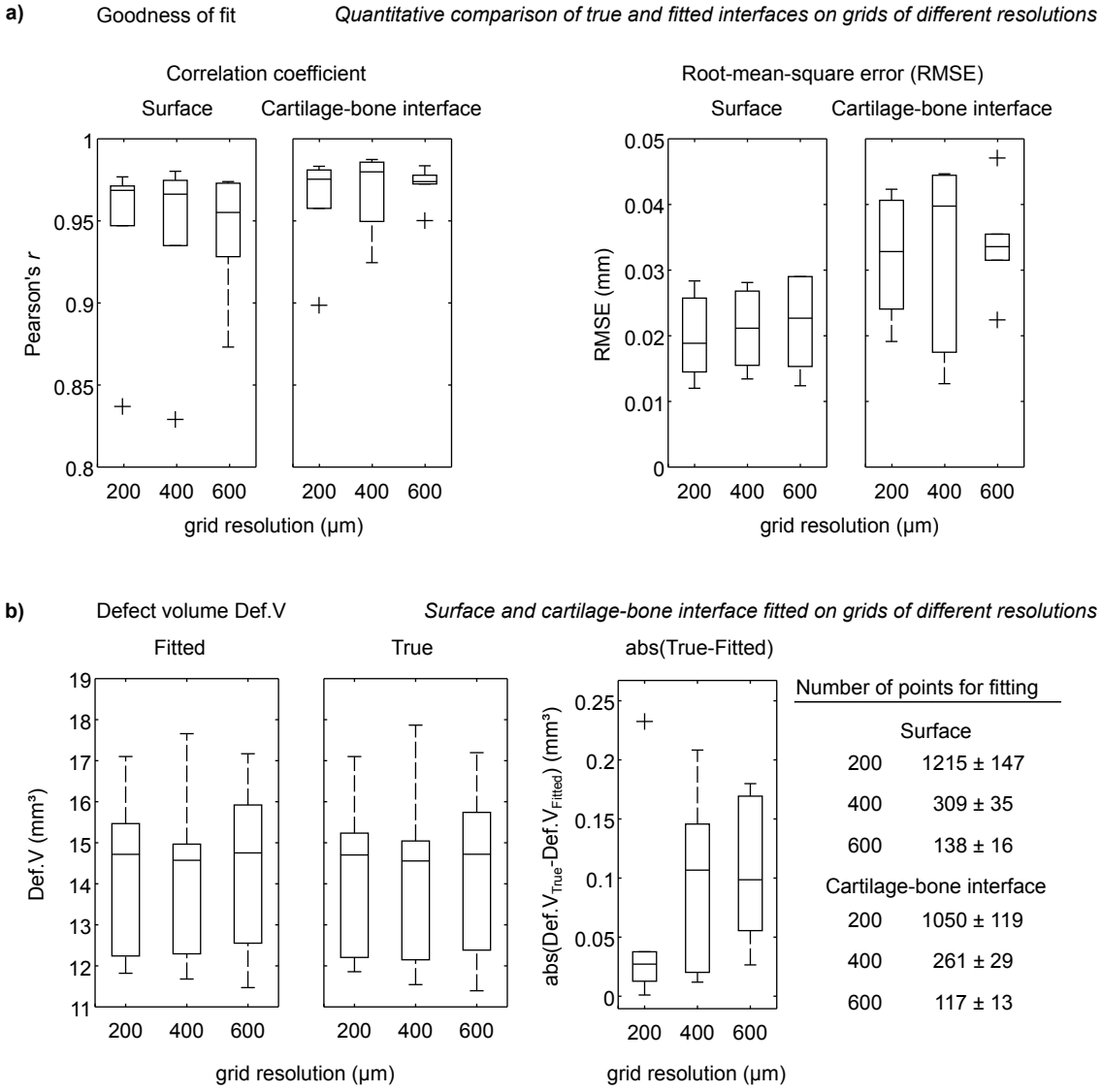

Figure 4.7 – Quantitative comparison of the fitted interfaces with the true interfaces. a) Goodness of fit expressed as Pearson's r and root-mean-square error (RMSE) for different grid resolutions. b) Estimated defect volume Def.V for fitted and true interfaces for different grid resolutions and absolute value of the differences between the Def.V from true and fitted interfaces. The table sums up the number of markers available for interface fitting each grid resolution. Please note, the values for the defect thickness Def.Th behave very similarly to Def.V and are therefore not shown.

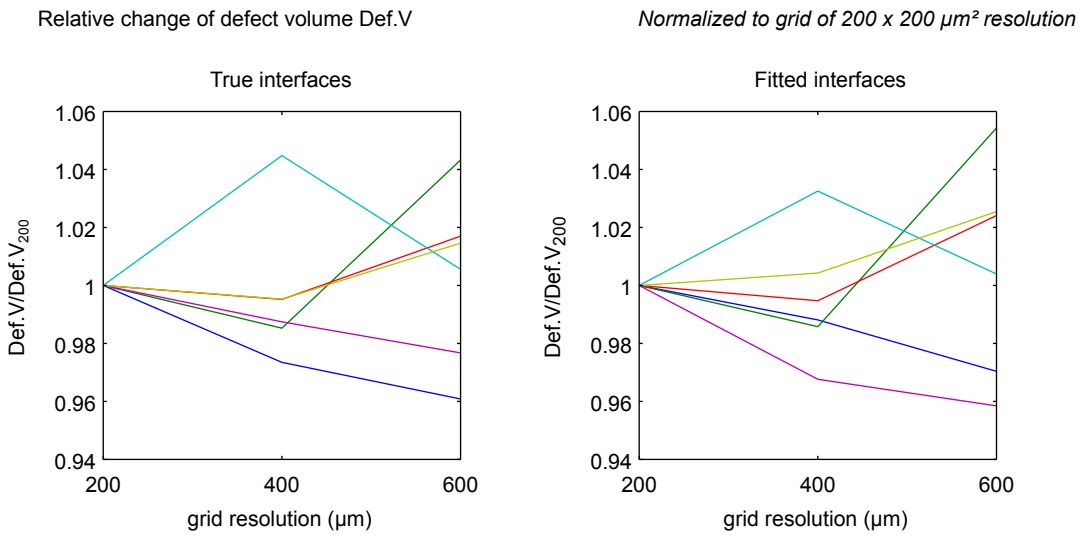

Figure 4.8 – The relative change of the defect volume Def.V estimated from the true and fitted interfaces normalized to the finest grid of 200 μm. Please note, the values for the defect thickness Def.Th behave very similarly to Def.V and are therefore not shown.

defect area is below the initial cartilage-bone interface. Also an indicator for damage and bone removal during the surgery. It should be considered that this shift is additionally enhanced by a smaller speed of sound in PBS than in cartilage. However, the visualization of the ultrasound cross-section is based on the assumption of one constant speed of sound. For the calculation of the thickness and volumetric parameters different tissue-specific sound velocities are used and therefore the obtained parameters are not affected. As a demonstration, the corrected height of the subchondral bone layer in the defect area was manually calculated for this sample and is marked by a dotted line. This sample shows also what happens in empty defect when lateral mechanical support is lacking. As seen in the histology slides and in the ultrasound image, the hyaline cartilage surrounding the defect is bent into the defect region. In the calculation of the UBM parameters, such tissue will then be attributed to defect filling tissue.
In Figure 4.9e the sample with the best outcome of the present study is shown. Both histology and ultrasound images show a defect filled up to the level of surrounding tissue. However, a large amount of defect filling (DefFill.V) is contributed by bone overgrowth (BV+). The derived ultrasound parameters are:

- DefFill.V: 99.7 %
- RepT.V: 75.4 %
- BV+: 24.3 %

Table 4.1 – Descriptive statistics of estimated thickness and volumetric parameters derived from UBM for all samples.

value		unit	mean		std
Thickness Def.Th	minimum	(mm)	0.67	±	0.25
	mean	(mm)	1.01	±	0.25
	maximum	(mm)	1.36	±	0.22
Def.Th difference (left-right)	mean	(mm)	0.07	±	0.26
	absolute value	(mm)	0.20	±	0.17
Volumetric parameters	Def.V	(mm^3)	32.85	±	7.20
	DefFill.V	(%)	71.92	±	16.58
	RepT.V	(%)	62.92	±	12.46
	BV+	(%)	9.00	±	7.83
	BV-	(mm^3)	5.22	±	6.02

The related scores of the conventional classification systems are the following:

- Outerbridge: 1
- ICRS-CRA *degree of defect repair*: 4
- ICRS-CRA *sum*: 11 (max. 12)
- O'Driscoll *thickness*: 0
- O'Driscoll *sum*: 20 (max. 24)
- ICRS-I informative sum: 18 (max. 18)
- ICRS-II *mean*: 83 (max. 100)
- ICRS-II *overall assessment*: 60 (max. 100)

In the following Figures 4.10-4.11 the corresponding values of the examples shown in Figure 4.9 a, b, c, d, and e are marked by Greek letters $\alpha, \beta, \gamma, \delta, \epsilon$.

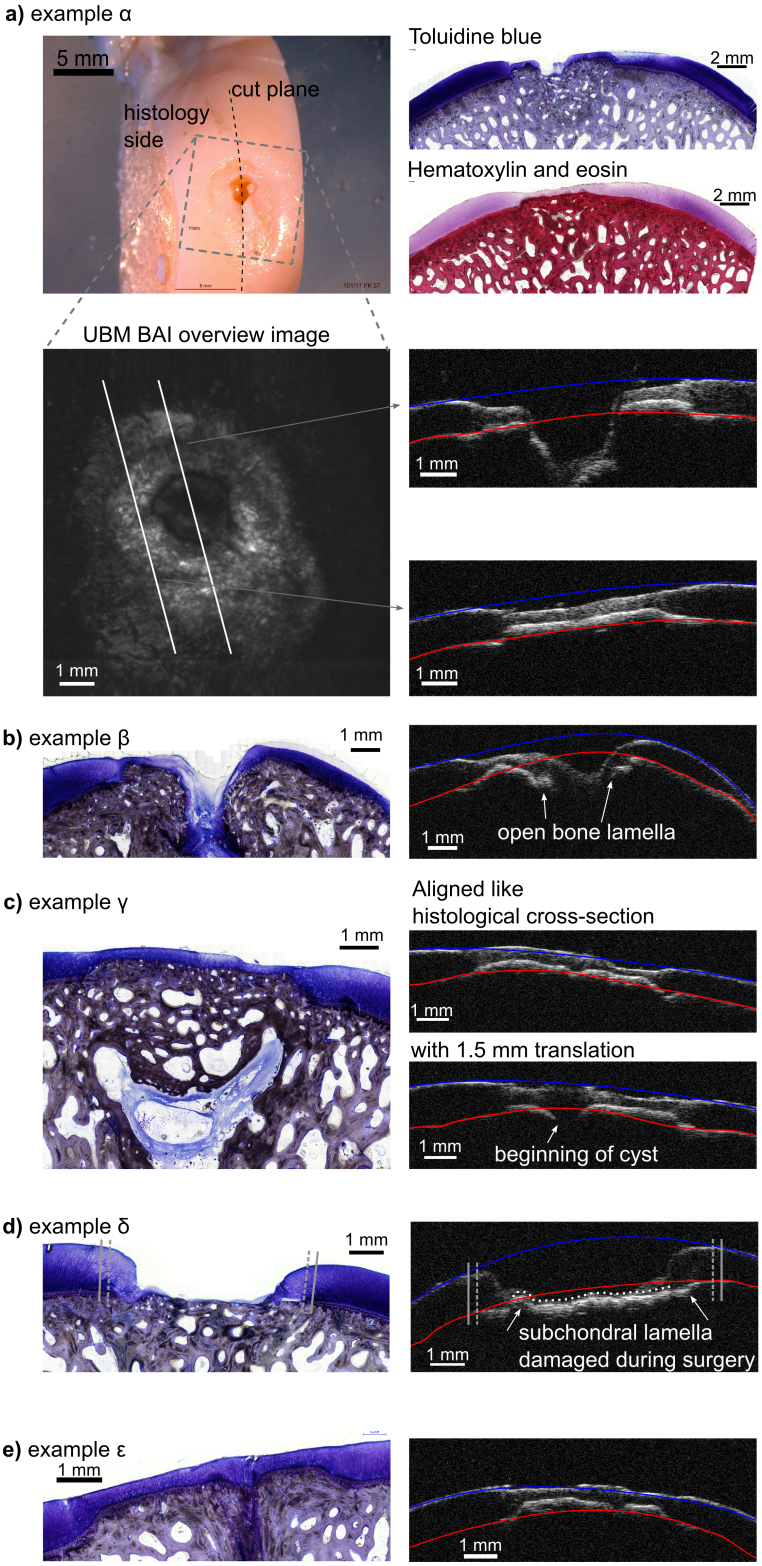

Figure 4.9 – Comparison of histological and ultrasound cross-sectional images. a) Macroscopic view on sample after cutting centrally through the defect region. The left part was used for histology, but both slides do not include the central cyst. Ultrasound cross-sectional images are just 1.5 mm apart. b) Sample with deep cyst where the deeper cyst structures cannot be visualized by ultrasound. The open bone lamella indicates deep cyst. c) Huge cyst covered by subchondral lamella is not visible in ultrasound; the breach can only be seen in the appropriate slide. d) Sample of exposed bone and superficial damage of subchondral lamella. The dashed and solid vertical lines indicate the 7-mm diameter defect boundary and the additional 0.25-mm fringe, respectively. e) Based on the derived scores, this was the best outcome of the present study. However, the sample still contains a large amount of bone overgrowth and a cyst.

Table 4.2 – Cross tabulation of macroscopic, MR and histopathological scores and UBM parameters for defect filling DefFill.V and repair tissue RepT.V. Spearmans ρ values are provided in **bold**, p values in normal font.

score	n	*ICRS-CRA*	*Mod. 2D MOCART*	*O'Driscoll*	*ICRS-I*	*ICRS-II*	*ICRS-II overall assessment*	*UBM DefFill.V*	*UBM RepT.V*
Outerbridge	58	**-0.679** <0.001	**-0.738** <0.001	**-0.715** <0.001	**-0.725** <0.001	**-0.723** <0.001	**-0.718** <0.001	**-0.633** <0.001	**-0.386** 0.003
ICRS-CRA *cumulative score*	58		**0.475** 0.014	**0.549** <0.001	**0.534** <0.001	**0.691** <0.001	**0.636** <0.001	**0.582** <0.001	**0.361** 0.005
Mod. 2D MOCART *cumulative score*	26			**0.731** <0.001	**0.816** <0.001	**0.603** <0.001	**0.644** <0.001	**0.720** <0.001	**0.560** 0.003
O'Driscoll *cumulative score*	58				**0.912** <0.001	**0.824** <0.001	**0.847** <0.001	**0.548** <0.001	**0.315** 0.016
ICRS-I *cumulative score*	58					**0.844** <0.001	**0.836** <0.001	**0.595** <0.001	**0.406** 0.002
ICRS-II *cumulative score*	58						**0.940** <0.001	**0.715** <0.001	**0.486** <0.001
ICRS-II *overall assessment*	58							**0.647** <0.001	**0.373** 0.004
UBM DefFill.V	58								**0.846** <0.001

4.3.3 Statistical analysis

The descriptive statistics for cartilage thickness, thickness differences between left and right knees, and the volumetric parameters are listed in Table 4.1. The scores O'Driscoll, ICRS-I, and ICRS-II were judged by two rates whose intra-rater correlation was $r \geq 0.93$ ($p < 0.0001$) and intraclass correlation was ICC ≥ 0.95. The correlation between the cumulative scores of the established classification systems and the UBM parameters is summarized in a cross tabulation (Table 4.2).
The results of the different repair approaches are covered by a confidential agreement. Thus, no results comparing different approaches are shown here. The relation between the defect filling DefFill.V of UBM to the macroscopically derived scores in shown in Figure 4.10a,c,e. According to the Outerbridge scale, no samples were graded as *normal* and only one sample with the second best grade as *softening and swelling* (Figure 4.10a). In the ICRS-CRA classifications system, the samples are

distributed over the entire range in the item *Degree of defect repair* as well as in the cumulative score (Figure 4.10c,e). The samples that were assigned to ICRA-CRA item *Degree of defect repair* grade 4 (*in level with surround cartilage*) showed significant higher defect filling DefFill.V in the UBM data (4.10c). A significant increase of DefFill.V with the cumulative ICRS-CRA score was found (4.10e). The comparison of UBM volumetric parameters to the results from MRI-based grading according to the modified 2D MOCART is shown in Figure 4.10b,d,f. One item of MOCART is assessing the *degree of defect repair*, thus direct comparison to DefFill.V appears appropriate. Significant differences for DefFill.V were found between samples of grade 5 to 10 and 5 to 20 (Figure 4.10b). According to MOCART only one sample had exposed bone. However, the exposed bone of sample δ (Figure 4.11d) was not detected in MRI. In contrast, 9 samples were assessed as completely filled (20 points). The MOCART item *Subchondral bone* can either be *intact* or *not intact – edema, granulation tissue, cysts, sclerosis* and thus was tested for differences in bone overgrowth BV+ or bone loss BV-. However, no significant differences were found. Figure 4.10d shows the raw data of BV- grouped according to the MOCART item *Subchondral bone*. The five samples with the highest BV- values were grouped as *not intact*. However, the *not intact* group includes several samples with low BV-values. The cumulative MOCART score was found to correlate significantly with UBM DefFill.V (Figure 4.10f). The comparison of the histology derived scores to UBM volumetric parameters is shown in Figure 4.11. The O'Driscoll item *thickness* and the cumulative score are compared to DefFill.V in Figures 4.11a and b, respectively. For all samples the O'Driscoll item *thickness* did not exceed scores higher than 1 ("50-100 % of normal adjacent cartilage"). Two-thirds of the samples were seen to have a filling below 50 %, also sample ϵ as the best outcome of this study. The defect filling was found to correlated positively with the sum of all O'Driscoll items (Figure 4.11b). The ICRS-I classification system has no item that appeared to be similar to the volumetric parameters of UBM. However, the cumulative ICRS-I showed a significant correlation to the defect filling DefFill.V (Figure 4.11c). For ICRS-II item *Subchondral bone abnormalities/marrow fibrosis* a significant negative correlation to the volume of bone loss BV- was noted (Figure 4.11d). The clustering of the scores given for this item around 50 is somewhat conspicuous. The item *overall assessment* and the mean of ICRS-II both showed significant positive correlation to the defect filling DefFill.V (Figure 4.11e-f). Briefly summarized, the defect filling derived from 3D ultrasound data correlates significantly to all classification systems used in this study. As seen in Table 4.2 also the volume of the repair tissue RepT.V shows these correlations, though with a reduced correlation coefficient.

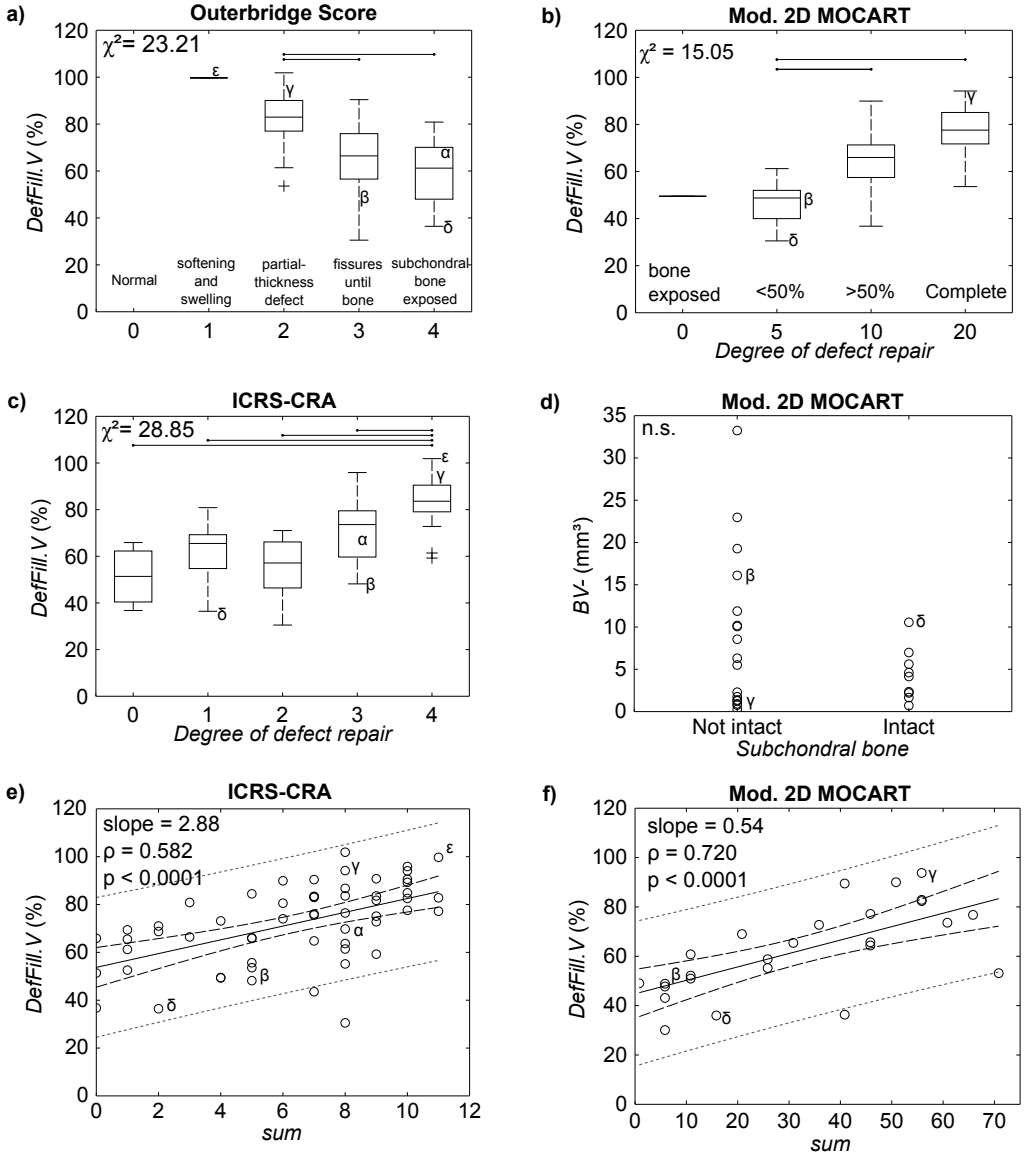

Figure 4.10 – Correlations of macroscopic scores and MOCART items to the defect filling DefFill.V and bone loss BV-. Boxplots of DefFill.V grouped according to a) the Outerbridge Score, b) MOCART item "Degree of repair tissue", and c) the ICRS-CRA item "Degree of defect repair". d) The volume of bone loss BV- grouped as "Not intact" and "Intact" according to the MOCART item "Subchondral bone". e) Linear correlation between DefFill.V and the cumulative score of ICRS-CRA. f) Linear correlation between DefFill.V and the cumulative score of modified 2D MOCART.

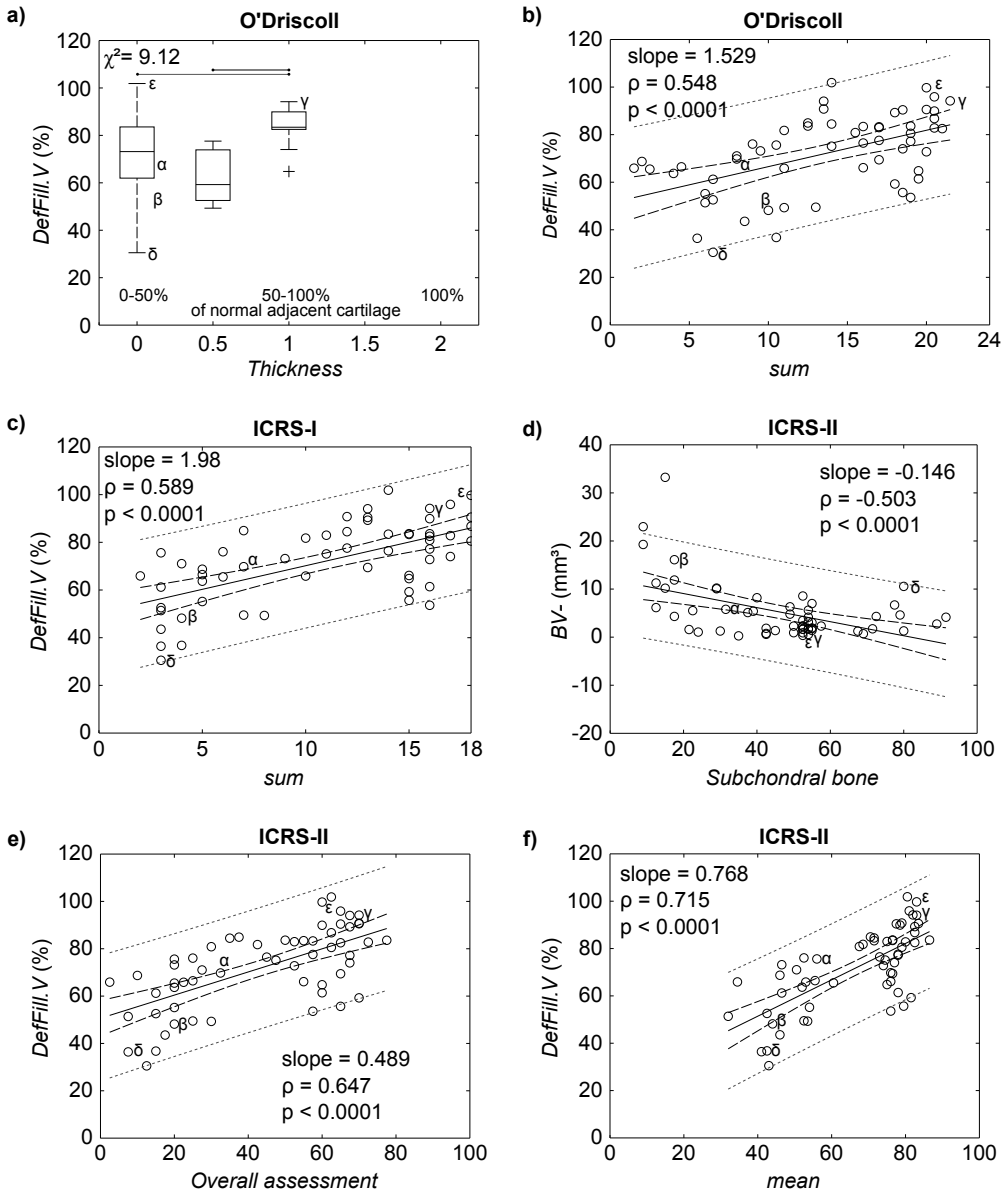

Figure 4.11 – Correlations of histopathological classification systems and defect filling DefFill.V or bone loss BV-. a) Boxplot of DefFill.V grouped according to the O'Driscoll item "Thickness". (b-c) Linear correlation between DefFill.V and the cumulative scores of b) O'Driscoll and c) ICRS-I. (d) Negative linear correlation between the BV- and the ICRS-II item "subchondral bone". e-f) Linear correlation between DefFill.V and e) the ICRS-II item "overall assessment" and f) the mean of all items of ICRS-II.

4.4 Discussion

This study focused on the demonstration of UBM for volumetric characterization of cartilage repair outcomes as an objective method. The methods used for data processing still required some user input, that could potentially have added a subjective factor. Manual input was required to define the center of the defect area and for correction of surface and bone markers that were occasionally defined incorrectly by the algorithm. The surface detection was usually very exact. The largest amount of incorrect definitions occurred at the cartilage-bone interface. Thus manual corrections were required, mostly at regions of irregular ossification, at cyst structures and at peripheral regions of low signal intensity caused by large inclination. Nevertheless, we consider the volumetric quantification of cartilage repair tissue based on UBM data as an objective method. Potential errors are mostly systematic errors as discussed in the following.

One source of systematic error is the lack of knowledge about the exact speed of sound in the cartilage repair tissue determining the spatial position along the z-axis. The speed of sound of the coupling medium is well known, thus the spatial position of the surface is very reliable. However, below the surface, the speed of sound is less well defined and will be different depending on the quality of the repair tissue, but within this study, a constant speed of sound was assumed. Thus, the z-position of the cartilage-bone interface is affected by this error in the speed of sound. Furthermore, the same error applies for the volumetric parameters. As already shown, at constant anatomical sites of joints the cartilage speed of sound values are quite invariable, e.g. 2 % variation for the medial femoral condyle and trochlea, 4 % variation at the patella (Töyräs et al., 2003). The speed of sound for cartilage repair tissue has not previously been documented. Derived from the reduced stiffness of repair tissue it can be assumed that speed of sound is lower than in hyaline cartilage (Gelse et al., 2010). Töyräs et al. reported a minimum speed of sound for degenerated cartilage of 1560 m/s (Töyräs et al., 2003). In relation to the constant 1660 m/s used in this study, a maximum error of 7 % in speed of sound is expected. The usage of a constant speed of sound results in a systematic error that is equally distributed over all samples and presumably does not affect the correlations with the established classification systems.

The second source of systematic error could be flattening of the healthy cartilage tissue located around the defect. After the defect was created, the load distribution of the condylar surfaces was altered. Especially the cartilage directly surrounding the defect was exposed to increased stress. Since lateral support was missing, the tissue bent into the defect region resulting in a flattening of cartilage thickness. This effect is clearly visible in the histology (Figure 4.9d). Unknown is the lateral extension of the thickness reduction. Flattening in the region defined in this study as *healthy area* and thus used for the estimation of the initial surface would cause a reduction in estimated cartilage thickness and defect volume. To reduce any potential influence

of flattened tissue, the measurements should include sufficient data from healthy cartilage with distance to the defect. The dimensions of the 0.25 mm fringe used in the data processing of this study are shown in Figure 4.9d. There the size of the fringe is sufficient to avoid to have bent tissue in the *healthy area*. Macroscopically, the lateral extension of tissue flattening can be assessed by the naked eye based on a circular light reflection of the moist cartilage surface around the defect (Jackson et al., 2001). The field of view of the UBM used in this study is presumably too small to visualize a laterally extended image of the surrounding cartilage. Histological images of low magnification could provide good overview images to allow more detailed investigation of cartilage flattening.

The experiments for verification of the interface fitting showed that also a low amount of points available for fitting can reliable estimate to the true surface and true cartilage-bone interface. The estimated defect thickness and defect volume are independent of the grid resolution. The number of points for estimating the original interfaces of the cartilage defects (Surface: 372; Cartilage-bone interface: 254) was comparable to the grid resolution of 400 $\times$ 400 μm^2 in the verification experiments (Surface: 309; Cartilage-bone interface: 261). The root-mean-square error for the cartilage-bone interface was higher than for the surface. Probably caused by slightly irregularities in the cartilage-bone interface. The marginal increase of the differences between defect volume estimated from true and fitted interfaces is presumably mainly determined by the reduced grid resolution (Figure 4.7b). As shown in Figure 4.8, the reduction of the grid resolution by a factor of 2 leads to deviations of $\pm$3 % and $\pm$4 % for reduction by a factor of 3. These verification experiments were performed on cartilage of human femur condyles that have a lower curvature than sheep condyles. In this respect the comparability is critical. The verification experiments showed that the models used to estimate the true interfaces are reliable. However, they should also be tested on more curved cartilage layers.

Within this study, a wide range of cartilage repair outcomes were observed: from severe cases of deep cysts and exposed subchondral bone to good outcomes with defects filled to the level of surrounding healthy cartilage. The cartilage thickness was found to show high variations between all different samples, but also between the left and right knees of the individual sheep (Table 4.1. The cartilage thickness was estimated at the site of the defect, which was not always necessarily set at the same anatomical site. Thus the variations can be caused by natural variations and from the selection of the spot where the defect was set. The findings of 0.20 mm intra-sheep variation and 0.25 mm inter-sheep variation with an average thickness of 1.01 mm support the use of the bilateral model (Hurtig et al., 2011). The variation between left and right knee are almost the same as between two animals. Thus, from the point of view of the defect depth, the left and right knee can be treated as independent from each other. The drawback of the high cartilage thick-

ness variation is a reduced comparability of the defects. When creating the defect, the cartilage thickness is unknown and the biopsy punch is adjusted to remove a predefined thickness (e.g. 1 mm). Depending on the real cartilage thickness at the site of punching, the resulting defects could be grade 2, 3A, 3B, 3C, 4A or 4B on the ICRS scale. Most crucial are the possible damage of the calcified layer and subchondral bone. Damage of subchondral bone and the resulting bleeding into the defect region drastically changes the repair potential and the outcome compared to a defect with intact subchondral bone. The comparability of these defects is doubtful with respect to the intention to test for superiority of a repair approach. Thus, it is highly recommended to measure cartilage thickness (e.g., with ultrasound) before creating the defect and using a tool that allows for adjustment of the exact depth of the defect. This would improve the comparability of future pre-clinical studies.

In some samples of the present study, the subchondral bone was also damaged (Figure 4.9d). With a view on the current study, this led to larger variations in the repair outcomes and was therefore beneficial. In other words, high variations in the initial effects led to a broader range of grades in the established classification systems. The correlation between the six classification systems was found to be good or excellent. Despite that ICRS-I and -II were developed for histology slides prepared from 2-mm biopsies, they showed excellent correlations to the O'Driscoll score that was developed for whole joint samples from animal studies.
For single items of the established classification systems, direct comparison to UBM parameters was reasonable, e.g. *Degree of defect repair* of ICRS-CRA to the UBM defect filling DefFill.V.
In macroscopic scoring, the grade of defect filling is assessed by Outerbridge and the ICRS-CRA item *Degree of defect repair*. In contrast to the other classification systems used in this study, in the Outerbridge score, the lowest values equal the best outcome. Thus, the correlation to DefFill.V is negative. Except for one sample (example ϵ), all samples of this study were scored with Outerbridge grade 2-4 (partial thickness defect – exposed bone). The limitation in macroscopic evaluation is that only superficial structures are accessible. All features below the surface are hidden. So the structure of the subchondral bone and potential bone overgrowth is invisible, and the estimation of the relative defect thickness is problematic. As long as the subchondral bone is covered by tissue, the total thickness of the cartilage layer cannot be seen. Thus, grading if the defect reaches to 25 %, 50 % or 75 % of the depth (ICRS-CRA *Degree of defect repair*) becomes very imprecise and rater-dependent as the true thickness can only be estimated. With this in mind, it is not surprising that no significant differences were found for DefFill.V between ICRA-CRA *Degree of defect repair* scores 0-3, and only for score 4 (*In level with surrounding cartilage*) the defect filling was significantly higher. Another problem with categorical grading is the definition of the category. This can lead to an overestimation of an individual feature that eventually becomes *the* classifying feature of the entire sample. For ex-

ample, in the Outerbridge scale, a sample gets the worst grade when bone is exposed. This happened in the example α where the central cyst was recognized as exposed subchondral bone. However, this sample appears completely different in histology and shows 60 % defect filling in UBM. Nevertheless, according to Outerbridge, this outcome is as bad as a total empty defect (example δ).
The item *Degree of defect repair* of the modified 2D MOCART appears to be positively biased, since 9 of 26 samples (35 %) were classified as having a complete filling. In the UBM data, these samples showed defect filling between 50 % and 95 %. The definition of the categories *filling above 50 %* and *complete* filling is very rough. Quite likely in such categories is observer bias that comes with information bias when considering the relatively low resolution of the MR images used in this study (voxel: 0.3 mm; slice: 3 mm) and the average cartilage thickness of 1 mm. The resolution appears too small to assess the structures of the cartilage repair sites within this study. It should be considered that human cartilage and the knee joint itself is around 3 times larger than in sheep. Thus more details could be visualized with the same resolution. However, at this point, it is not possible to extrapolate the correlations between modified 2D MOCART and volumetric UBM parameters to an application in human cartilage defects. For this study, an MR system that provides more resolutions would have been better to allow for justified comparison to UBM. As already been shown, an experimental high-field MR scanner with 9.4 T (isotropic voxel size: 120 μm) allows for reliable evaluation of explanted cartilage repair outcomes in sheep (Goebel et al., 2014).
The O'Driscoll item *thickness* is the only item of the histopathological scores that address the thickness of the repair tissue. Important to consider, this item focuses not on the filling of the defect, but only at the thickness of the cartilaginous tissue layer - bone overgrowth is not considered. This explains why one of the best (example ϵ) and one of the worst (example δ) outcomes were both scored with the lowest value. In O'Driscoll item *thickness* no sample from the current study was scored with 100 % cartilage thickness. Furthermore, two-thirds of all samples were graded as having repair tissue thickness below 50 %. In contrast, for these samples, the UBM data revealed defect filling between 30 % and 100 % and a median of 73 %.
The classification systems ICRS-I and -II are both designed for the histopathological assessment of biopsy samples. These biopsies are 2 mm in diameter and do not necessarily include subchondral bone. Thus, neither classification systems address the thickness of defect filling. For the majority of the items from ICRS-I and -II a causal relation to the volumetric UBM parameter was not given and thus no statistical tests were conducted with them. ICRS-II item *Subchondral bone* was uniquely found to show a negative correlation with the bone loss BV-.
Some might argue about the usage of ICRS-I and -II for the grading of histology slides showing a cross-section of the entire cartilage repair site including adjacent hyaline cartilage. From the definition of both classification systems, the features of all items can be accessed in these histology slides. However, the more comprehensive

overview of the repair site may influence the rater. In contrast to 2 mm biopsies, the histology slides used here exhibit more variable structures and different qualities of repair tissue within one repair outcome. This may cause uncertainties for the rater and may add observer bias. However, in the present study, very good intra-rater and intraclass correlations were found and the correlation to the O'Driscoll score was excellent. Thus, for the aim of this study, the usage of ICRS-I and -II appears to be justified. Caution is required when comparing the scores of ICRS-I and -II with other studies that used biopsy samples.

The structures visible in a histological slide strongly depend on the location the sample was cut. However, an individual cross-section is often used as representative for the entire sample. As seen in this study, the three-dimensional morphology of cartilage repair tissue is very variable. Thus the scoring of only two slides is prone to over- or underestimation of certain features. Example α was an extreme case for this (Figure 4.9a). As shown, the deep cyst in the center of the defect was completely missing in one of the histology slides. Now considering a 2-mm diameter biopsy is used to investigate the success of a cartilage repair technique. According to the German Cartilage Registry (Niemeyer et al., 2015) the average cartilage defect size in humans is 3.68 ± 0.23 cm^2. For this area, a 2 mm biopsy would investigate less than 1 % of the total area. When considering the large variations of repair tissue found in some of the samples of the present study, the usage of biopsies in humans as follow-up appears to have very little diagnostic value.
The 3D UBM data, in contrast, can acquire the entire defect area and all structures contribute equally to the results. Additionally, the UBM acquisition is non-destructive, less time consuming and therefore potentially feasible for repeated scans, allowing for monitoring of cartilage repair. The proposed parameter DefFill.V quantifies the relative filling of the former defect. Based on the good correlation with established classification systems, this parameter appears to be very suitable as an overall parameter for the quality of the repair outcome. Interestingly, DefFill.V also showed a very good correlation to the histology based ICRS-II item *overall assessment*. This item is defined by the general impression of the rater about the repair outcome quality. The UBM data enabled us to distinguish between the defect filling tissue in bone overgrowth BV+ and soft repair tissue RepT.V. The correlations for RepT.V were similar to the defect filling DefFill.V, but always with lower correlation coefficient. For the repair outcomes of the present study, we found an average defect filling DefFill.V of 72 % containing 63 % soft repair tissue (RepT.V) and 9 % bone overgrowth (BV+). However, the ratio of RepT.V to BV+ will differ between the samples, but the amount of bone overgrowth is not assessed by the established classification systems. This may explain the smaller correlation coefficients for RepT.V. This is demonstrated in the example ϵ: In macroscopic and histopathological grading this sample was scored with highest grades (e.g. mean ICRS-II: 83). However, the ICRS-II *overall assessment* was only scored with 60 of 100 points. Probably the

rater considered the substantial amount of bone overgrowth in his judgment more than possible by the definitions of the single items of the classification systems. Bone overgrowth leads to changed biomechanics also of the opposing articulating surface of the joint and to a reduced cartilage repair tissue thickness. The importance of the subchondral bone plate in cartilage repair has already been demonstrated and bone overgrowth is known to increase the risk for the repair tissue for "damage from shear forces" (Gomoll et al., 2010).

Based on the finding of this study, we conclude that the UBM parameter DefFill.V is a robust parameter with the potential to quantify the quality of cartilage repair tissue. The good correlation to the ICRS-II item *overall assessment* supports this because Bonasia et al. awards this item as the most reliable of ten major histopathological classification systems (Bonasia et al., 2014). Additionally, Blackman et al. revealed in a comprehensive meta-analysis that the MOCART item *Degree of defect repair* results in the best correlations to clinical outcomes measures (Blackman et al., 2013). Also Marlovits et al. (Marlovits et al., 2006) found best correlations for MOCART item *Degree of defect repair* to patient-reported outcomes two years after autologous chondrocyte transplantation. So the best correlations to patient-based outcomes were obtained from parameters that judge the defect filling. For completeness, some studies found no correlation between this MOCART item and patient-reported outcomes (Ebert et al., 2014).
Future experiments should aim for arthroscopic or transcutaneous application of the UBM methods described in this work. It has already been demonstrated that arthroscopic ultrasound imaging of the knee joint is feasible (Kaleva et al., 2011; Liukkonen et al., 2014). Quantitative cartilage characterization based on transcutaneous ultrasound is only reported by a few publications. However, only some regions of interest, e.g. the femoral condyles and trochlea, are accessible with clinical ultrasound imaging systems transcutaneously (Möller et al., 2008). At least for those sites, transcutaneous ultrasound would be highly beneficial and patient friendly.
The translation of the UBM method and its data processing steps to application in the human knee will face some problems. First, the size of focal cartilage defects in human is approximately ten times larger than the defects of the present study. Thus, the scanner needs to be scaled to allow acquisition of a larger area. Modern commercially available high-frequency ultrasound array scanners should be suitable for this. Second, fully automated data processing is preferred to avoid any operator bias. This will require a standardized procedure for ultrasound imaging of articular cartilage. Third, the mathematical model to estimate the initial cartilage surface and cartilage-bone interface need to be adapted to larger defects and different anatomical sites. Fourth, a technical solution is required to allow reliable 3D imaging of cartilage in vivo, either transcutaneously or arthroscopically. Such imaging methods would presumably work with a reduced ultrasound frequency compared to this study, which would, in turn, reduce the resolution. Nevertheless, based on

the larger structures and thicker cartilage in humans, the accuracy would be similar to the UBM parameter obtained from sheep samples of the present study.

This study showed how 3D data from UBM scans of cartilage repair tissue can be used for volumetric quantification. Of the derived parameters the defect filling DefFill.V was the most important since it showed good to excellent significant correlations to established classification systems that were based on macroscopic evaluation, MR imaging, or histopathological evaluation. As shown, the defect filling tissue can further be differentiated into soft repair tissue and mineralized tissue from bone overgrowth. Furthermore, a further characterization of the repair tissue (fibrotic or hyaline-like) could be possible based on ultrasound backscatter analysis (Gelse et al., 2010). A translation of these methods to a transcutaneous application or arthroscopic application could add substantial support to individual repair follow-up and cartilage repair research activities.

5 Study III - Ultrasound palpation

The findings of this part of the thesis are partially published in the journal Biomechanics and Modeling in Mechanobiology under the title: "Ultrasound palpation for fast in-situ quantification of articular cartilage stiffness, thickness and relaxation capacity" (Schöne et al., 2017).

5.1 Introduction

In this chapter, a new method of ultrasound palpation (USP) will be described. This method enables biomechanical testing of cartilage within seconds, performed with a hand-held, pen-style probe. This method describes the estimation of applied stress and strain during manually performed palpation purely on basis of ultrasound pulse-echo time-of-flight evaluation. Further, it will be shown how repeated USP measurements can be used to quantify the cartilage relaxation behavior. This study aimed to understand the principles of this method, to validate a functional prototype and to investigate its sensitivity to degenerative changes of articular cartilage.

5.2 Materials and methods

5.2.1 USP hardware and software

Hardware components

Measurements with USP require ultrasound emission and detection in pulse-echo mode. In the present work, the ultrasound pulses were excited and digitized with 100 MS/s by an all-in-one hardware box (GS200, GAMPT mbH, Merseburg, Germany) that was connected to a personal computer. Custom software (MATLAB 2011b, The Mathworks Inc., Natick, MA, USA) was developed to control the data acquisition, measurements of the times of flight, plotting, and for the evaluation of the stress-strain curves in real time.

USP probe and tip

The novelty of the USP method is the design of the ultrasound probe. Our collaboration partner GAMPT developed a custom pen-style ultrasound probe with a

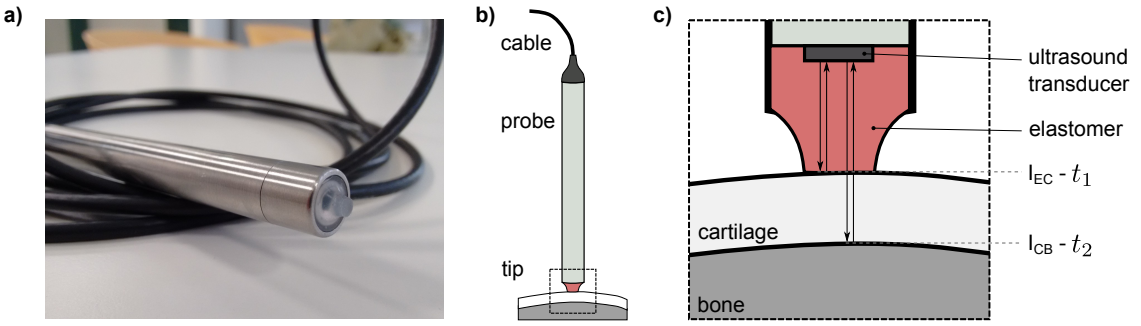

Figure 5.1 – a) Photography of the USP probe. b) Schematic drawing of the USP probe in contact with a cartilage layer. c) Schematic cross-section through the USP tip with illustration of the ultrasonic paths. The elastomer-cartilage and cartilage-bone interfaces are denoted with I_{EC} and I_{CB}, respectively. Both interfaces cause a pulse echo at the time of flight t_1 and t_2, respectively.

center frequency of 10 MHz and 3-mm diameter piezoceramic element (Fig. 5.1 a). The crucial component is an elastomer tip covering the ultrasound transducer (Fig. 5.1 b). The ultrasound transducer emits short ultrasound pulses that propagate through the elastomer and further through a sample when the elastomer and the sample are acoustically coupled. At each interface, a portion of the emitted sound wave is reflected back to the transducer. The length of the propagation path and the speed of sound of the traversed materials defines the time of flight until the pulse echo is received. Therefore, when measuring articular cartilage, the detected signal contains pulse echoes of the reflection at the elastomer-cartilage interface I_{EC} at t_1 and of the reflection at the cartilage-bone interface I_{CB} at t_2.
In this respect, the requirements for the elastomer's acoustic properties become clear. First, the acoustic impedance of the elastomer must be different to cartilage in order to obtain the reflection at the elastomer-cartilage interface I_{EC}. Second, the acoustic attenuation of elastomers is rather high and causes significant signal losses along the propagation through the elastomer. Therefore, the elastomer of low acoustic attenuation is required.
The shape of the elastomer tip needs to be defined considering the sound field defined by the ultrasound transducer. Most important are the sound field diameter and the near-field properties defined by transducer diameter, frequency, and SOS in the elastomer.

Estimation of applied force

By pressing the USP probe against the cartilage layer, the applied force acts equally on both the cartilage and the elastomer. This compresses the cartilage layer and the elastomer, resulting in a reduction of the sound paths and therefore in a reduction of times of the flight t_1 and t_2. When the relation between t_1 and the applied force

F is known from the previous calibration, the force applied during palpation of the cartilage layer can be derived based on a t_1-measurement

$$F = f_{\text{cal}}^{F}(t_1), \tag{5.1}$$

where $f_{\text{cal}}^{F}(t_1)$ is the force calibration function.
Similar to the sound path reduction under mechanical load, the contact area of the USP tip to the sample can increase based on the incompressibility of elastomers ($\nu \approx 0.5$). This relation can be calibrated ahead of time and allows the estimation of the contact area A based on t_1

$$A = f_{\text{cal}}^{A}(t_1). \tag{5.2}$$

Taken together, the applied stress can be obtained by t_1 measurement and previously obtained calibrations curves for force and contact area.

$$\begin{aligned} \sigma &= \frac{F}{A} \\ &= \frac{f_{\text{cal}}^{F}(t_1)}{f_{\text{cal}}^{A}(t_1)} \end{aligned} \tag{5.3}$$

For the current study the area change during compression was neglected, since preliminary experiments showed that this is a factor which is shows no reproducible behavior between experiment and calibration setup. Instead, a constant contact force was assumed, defined by the diameter of the unloaded elastomer tip.

Estimation of applied strain

The strain was estimated as shown before (sec. 2.4.4) with the assumption that speed of sound remains constant during compression. The initial time of flight through the sample $\Delta t_0 = t_{2,0} - t_{1,0}$ was estimated at the beginning of the USP measurement. During the palpation, the current strain was calculated based on the current time of flight difference $\Delta t = t_2 - t_1$ and eq. 2.36.

Time-of-flight estimation by phase-root seeking

Essential for the precision of the ultrasound palpation is the precise estimation of the TOF of both pulse echoes. To allow for real-time evaluation, this method should also be fast. It was found, that Phase-root-seeking (PRS) is the most suitable method for the data evaluation of USP. The PRS algorithm was developed for elastography imaging and provides the temporal delay between two slightly shifted signals (Pesavento et al., 1999). It is assumed a signal acquired under compression is a

compressed and time-shifted version of the signal before compression:

$$x_2(t) = x_1(a \cdot t + t_0). \tag{5.4}$$

Within a small temporal region, the compression can be neglected and the signal is only time-shifted by τ, leading to the more simple equation:

$$x_2(t) = x_1(t - \tau). \tag{5.5}$$

The cross-correlation between the two signals x_1 and x_2 is defined as

$$(x_1 \star x_2)(\tau) \overset{\text{def}}{=} \int_{-\infty}^{\infty} x_1^*(t)\ x_2(t+\tau)\, dt, \tag{5.6}$$

where $x_1^*(t)$ is the complex conjugate of $x_1(t)$. At $-\tau$, the cross-correlation function has its maximum amplitude. But in the calculation of PRS is based on the phase $\varphi(t)$ of the cross-correlation function of the corresponding analytic signals $x_{1+}(t)$ and $x_{2+}(t)$

$$\varphi(t) = \arg\left((x_{1+} \star x_{2+})(t)\right). \tag{5.7}$$

Defining for the term of *phase-root-seeking* is the fact that the phase is zero at $-\tau$

$$\varphi(-\tau) = 0 \tag{5.8}$$

and this root needs to be found in order to know the delay τ. In the vicinity of that root, the phase $\varphi(t)$ is nearly linear and its slope is defined by the signals centroid frequency $\omega_0 = \frac{f_0}{2\pi}$. To find the root a Newton iteration can be used:

$$t_{n+1} = t_n - \frac{\varphi(t_n)}{\dot{\varphi}(t_n)}. \tag{5.9}$$

This is simplified with the assumption $\dot{\varphi}(t_n) = \omega_0$

$$\begin{aligned} t_{n+1} &\approx t_n - \frac{\varphi(t_n)}{\omega_0} \\ &\approx t_n - \frac{\arg\left((x_{1+} \star x_{2+})(t_n)\right)}{\omega_0}. \end{aligned} \tag{5.10}$$

With each iteration step, this method approaches the true value of τ. The number of performed iterations is a question of computation power, time, and required accuracy.

Evaluation of stress-strain curve

The USP system is aiming for a real-time tracking of t_1 and t_2 to obtain stress and strain. This allows visualization of the stress-strain curve while compression. The slope of this curve correlates to the stiffness of the cartilage layer. However, Hayes et al. (Hayes et al., 1972) showed that for indentation experiments the obtained stiffness is also affected by sample thickness h, indenter radius a and indentation depth ω. They provided a correction algorithm that remains the gold standard.
Hayed correction was performed as described in section 2.4.5. However, in equation 2.42 Young's modulus E is obtained from the static values of applied force and resulting displacement. This is problematic for the dynamic and fast character of an USP measurement, where the slope of the entire stress-strain curve $\frac{\mathrm{d}\sigma}{\mathrm{d}\epsilon}$ should be evaluated and corrected. Therefore, in the present work, an adjusted form of the Hayes correction is used:

$$E = \frac{(1-\nu^2)a\pi}{2\kappa h} \cdot \frac{\mathrm{d}\sigma}{\mathrm{d}\epsilon}. \tag{5.11}$$

Values for the correction factor κ have been estimated based on FEM simulations for a wide range of $\frac{a}{h}$ ratios and for different Poisson's values. These values were used as reference in this thesis (Zhang et al., 1997).

5.2.2 Mechanical and acoustical properties of different elastomers

The elastomer tip is the most important component of USP and needs to be selected with respect to the material being tested. The most important parameters: elastomer stiffness, acoustic impedance, and attenuation. It was estimated that the stiffness of the elastomer should be similar to the test material. The acoustic impedance should differ as much as possible to increase the reflection coefficient R (2.3.1, Eq. 2.11). Finally, the attenuation of the sound wave should be as low as possible. The acoustic parameters need to be optimized to improve the signal-to-noise ratio and the stiffness defines the measurement range.
For measurements on articular cartilage a maximum stiffness of 20 MPa was targeted (Saarakkala et al., 2004a). The stiffness of elastomers is usually measured as hardness based on the Shore grade (durometer). The relation of stiffness and shore grade has been modeled and experimentally proven by Kunz and Studer (Kunz and Studer, 2006). Based on their work, the target hardness of Shore-A grade between 80 and 90 was defined. For comparison, this is harder than car tires and approximately the hardness of inline skate wheels. Based on the limited availability of medical grade elastomers with this high hardness any test materials that could be obtained were tested for their acoustic properties. In total, 17 different materials have been tested for speed of sound and attenuation. The test materials were available in layers of 2-4 mm thickness. The exact thickness was measured with a digital

caliper. Pulse echoes were acquired with a 10-MHz contact transducer (KBA120) at the GS200 and evaluated subsequently. The time of flight through the test material was determined and with the thickness, the speed of sound was calculated. The density values were obtained from the manufacturer data sheet. Finally, the attenuation was quantified by

$$\alpha = \frac{1}{2d} \frac{V_{peak}}{V_{ref}}, \tag{5.12}$$

where V_{peak} is the maximum voltage of the envelope curve of the pulse echo, V_{ref} a reference voltage (2 V), and d the material thickness. This experiment gives just a rough estimate of the attenuation, but it is enough to support the choice for the right material for USP.

5.2.3 Calibration

The actuator of the material testing machine (ElectroForce TestBench, BOSE) was not able to mount the USP probe. Therefore, the USP probe was mounted upside down at the material testing machine. Between the USP probe and the actuator, the load cell and a 6-mm diameter steel target were mounted (Fig. 5.2 a). A drop of water between the USP tip and the steel target ensured acoustic coupling. The actuator was used to move the steel target to reach a deformation of the USP elastomer tip by 0.5 mm. During deformation, force F, displacement z and the pulse echoes were recorded continuously. Since the material testing machine and USP data acquisition systems recorded their data independently from each other, the data required synchronization afterward. To support this, short displacement peaks were driven before and after the loading-unloading phase to create reference points in the data (Fig. 5.2 b). The TOF through the USP elastomer t_1 was calculated by the PRS method as described before. The calibration function $f_{\text{cal}}(t_1)$ was obtained by fitting the applied force $F$and t_1 in the loading phase to a polynomial of 4^{th} (Fig. 5.2 c). This calibration experiment was repeated for the displacement rates of 0.05, 0.10, 0.20, 0.30, 0.50, and 1.00 mm/s to investigate for potential strain-rate effects.

5.2.4 Reference phantoms

To verify the USP measurements reference samples were created from polyurethane (PU). A PU molding kit (Ebalta GM 956/GM 356-1) allowed for definition of the final stiffness of the cured material by using different mixture ratios of three components. Table 5.1 gives an overview of the mixtures as provided by the manufacturer and as used in the present study. The three components were first carefully mixed and then the resin was given into aluminum molds. They provided flat cylindrical shapes with a diameter of 4 cm and different heights between 2 and 4 mm. The molds were completely filled with resin and then closed with a PMMA plate, fixed to prevent slip and then placed in a pressure pot. The pressure pot was adjusted

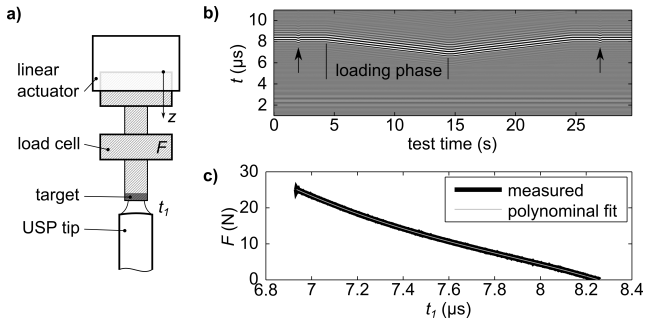

Figure 5.2 – a) Schematic setup of the USP probe during calibration. The shaded components were moved, while the white parts were fixed in place. b) 2D representation of the recorded RF signals for the acquired test time. The arrows point at the reference points for later synchronization. Only the loading phase was used to create the calibration curve. c) The relation between F and t_1 and the parameterized calibration curve $f_{\mathrm{cal}}(t_1)$ as a polynomial of the 4^{th} order.

to a pressure of 2 bar and immersed in a water bath of 70°C. The PU samples were removed from the molds after a curing time of at least 4 hours. Finally, each sample thickness was measured with a micrometer caliper.

Table 5.1 – Table of Ebalta GM 956 polyurethane mixtures to adjust the stiffness of the cured material. Components A, B and B-1 are denoted as *GM 956 Komp. A*, *GM 956 Komp. B*, and *GM 956-1 Komp. B* by the manufacturer, respectively. First, B and B-1 components were mixed, then mixed with the A component.

	guideline [parts]			**measured [g]**		
Shore A	**A**	**B**	**B-1**	**A**	**B**	**B-1**
30	100	195	-	20.405	39.814	-
50	100	125	30	19.650	23.915	5.715
60	100	100	40	18.365	18.174	7.320
70	100	50	60	24.962	12.555	14.954
80	100	-	80	15.345	-	12.793

5.2.5 Cartilage samples

The cartilage samples originated from a total of 9 fresh porcine patellae, that were obtained from a local butcher's shop. After being removed from the joint, the patellae were stored at -22°C. Care was taken that the patellae kept their naturally moist surface covered by synovial fluid between removal from the joint and freezing. Before measurements, the frozen patella was immersed in PBS at room temperature

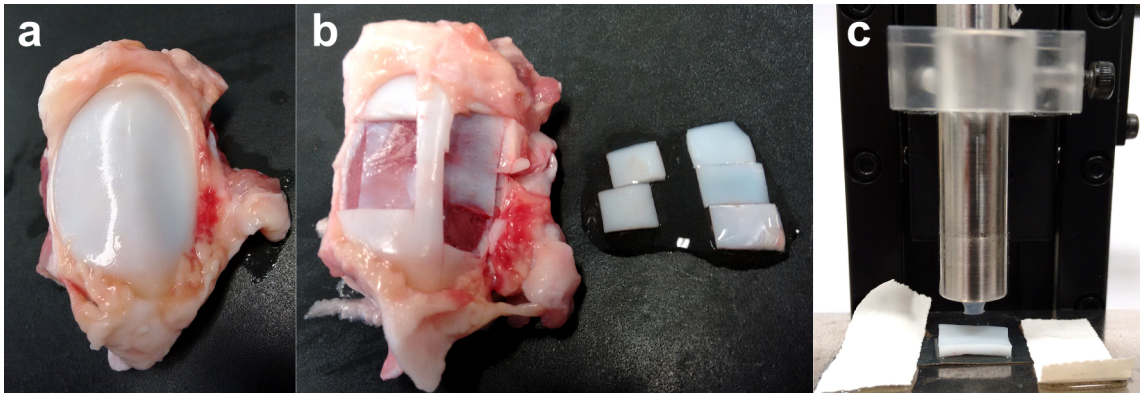

Figure 5.3 – a) Intact cartilage surface of porcine patella used for in-situ measurements. b) Full-thickness cartilage samples removed from the patella used for ex-situ measurements. c) Ex-situ USP measurement on a full-thickness cartilage sample in the mounted setup.

to allow thawing. USP measurements at the cartilage layer of the patella without further preparation were denoted as in-situ measurement within this study (Fig. 5.3 a). In contrast, ex-situ measurements were conducted on full-thickness cartilage samples that were cut with a scalpel from the bone. From each patella, two or three ex-situ samples were prepared from the medial or the lateral facet (Fig. 5.3 b). First, full-thickness cuts were made to define the sample size, then the cartilage sample was detached from the subchondral bone by slicing along the cartilage-bone interface.
Some of the ex-situ cartilage samples were enzymatically degenerated by a trypsin/EDTA solution (0.25% / 0.02 % (w/v) in PBS w/o Ca^{2+} and w/o Mg^{2+}, Biochrom GmbH, Germany) solution. The samples were entirely immersed in that solution and placed into an incubator set to a temperature of 37°C. Trypsin is a common protein in the digestive system. In articular cartilage research, it is often used to simulate cartilage degeneration because it is known to digest the proteoglycans and also has a minor effect on the collagen network (Saarakkala et al., 2004b).

5.2.6 Repeated ultrasound palpations

As stated before, loading and unloading of articular cartilage causes interstitial water movements and relaxation processes (2.4.2). Therefore, repeated USP measurements at one spot are always affected by the palpation performed right before as long the relaxation process is not entirely finished. To investigate the sensitivity of USP to these effects we performed 3 to 5 USP measurements of each sample at the same spot and took a closer look at the initial time of flight through the cartilage layer Δt^0 and the derived stiffness E. First, these values were normalized to the corresponding value of the first palpation and fitted to a linear model. With the

assumption of constant speed of sound, the changes in time of flight correlate to the changes of thickness (Eq. 2.34). The relative change of thickness RCT for subsequent palpations k was obtained by linear regression based on the model:

$$\frac{\Delta t_{0,k}}{\Delta t_{0,1}} = RCT \cdot k + const., \tag{5.13}$$

and accordingly, for the model of the relative change of stiffness (RCS) as

$$\frac{E_k}{E_1} = RCS \cdot k + const. \tag{5.14}$$

Based on this model, the parameters RCT and RCS describe the relative change in cartilage thickness and stiffness with each palpation. This only applies under the assumption that the delay between two palpations at the same spot is so short that there is no time for complete relaxation. In general, the USP measurements need to be done with comparable performance. This was evaluated by recording the average time between subsequent palpations ΔT, the applied preload F_0, maximum strain ϵ_{max} and strain rate $\dot{\epsilon}$.

5.2.7 Indentation

Reference stiffness values were obtained by indentation experiments performed on a high-precision material testing machine (ElectroForce TestBench, BOSE, Framingham, MA, USA). The setup comprised a load cell (BOSE ElectroForce, WMC-50-543, maximum load 225 N), a linear actuator and the indenter arranged in-line. A flat-ended circular steel indenter of 3 mm and 1.5 mm diameter for the reference phantoms and cartilage samples were used, respectively. During testing the sample was supported by a flat metal plate. The distance between this plate and the indenter tip z_{ref} was measured before. First, the indenter was moved towards the sample surface. The position when the indenter first came in contact with the sample was denoted as position z_0 and noticed by a little peak in the load cell data. Based on the difference between z_0 and z_{ref} the sample thickness h was defined. Optimal contact was ensured by applying 5 % pre-strain. Then, a one-step displacement-controlled indentation of 5 % strain with 2.5 $\%/s$ strain-rate was performed. The indenter position was held for a dwell time of 2 s and then returned to the starting position. The force and displacement data were recorded with a sampling rate of 20 s^{-1} and saved for subsequent evaluation.
The data evaluation focused on the loading phase of the stress-strain curve. First, using linear regression in the strain range of 0-5 % the uncorrected stiffness was estimated. In a second step, correction according to Hayes (Eq. 5.11) was applied to obtain the final stiffness. For the correction, a Poisson's ratio of $\nu = 0.5$ was assumed and the values for κ have been obtained from interpolation of the values

provided by Zhang et al. 1997.

5.2.8 Overview of the experiments

Reference phantoms

The reference values of the phantom stiffness were obtained by indentation, as described in section 5.2.7. For USP measurements, the phantoms were placed on a rigid metal plate and a drop of water ensured ultrasonic coupling. The USP measurements were performed in two setups: one hand-held setup and one setup with the USP probe mounted on a manual driven linear translation stage. Each sample was measured 12 times for each setup. Since the USP software provided real-time data of preload and applied strain, the measurements conditions could be performed under comparable conditions for each sample. The recorded data were later used to quantify the comparability.
In a second run, intra-operator and inter-operator reliability were investigated by hand-held USP measurements performed on eight reference phantoms by five different users. I was one of these users and the others were colleagues that were inexperienced with USP measurements and received instructions directly before their measurements. They conducted some trial measurements until they felt confident. Each user tested the same reference phantoms in 10 sequential iterations.

Native, trypsinized and PBS immersed cartilage

A total of 27 native full-thickness ex-situ cartilage samples have been prepared from 7 porcine patellae. Each sample was first measured by indentation and then probed by 3-5 repeated USP measurements in the mounted setup. These samples were then measured again with both methods after being immersed in trypsin (n=5) or in PBS (n=5) at 37°C (Fig. 5.4 a). The measurements were repeated at 1, 2, and 3 hours of immersion.
The USP measurements were done in the mounted setup (Fig. 5.3 c). The cartilage sample was placed on a rigid metal plate below the USP probe and moistened with PBS. A thin layer of fine abrasive paper (FEPA grit 800) was glued to the metal plate to prevent lateral slippage of the cartilage sample. The USP probe was then moved to the sample. By checking the pulse echoes and the preload displayed by the USP software, proper contact was confirmed between USP probe and cartilage sample.

In-situ and ex-situ cartilage

This experiment was conducted to reveal differences between mechanical testing done on the intact cartilage layer that is connected to the bone and testing done on cartilage samples that are removed from the bone. First, seven sites of two porcine

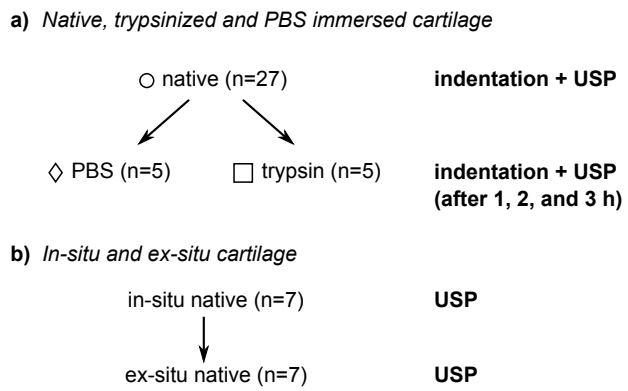

Figure 5.4 – Illustration of cartilage experiment workflow. a) Measurements to compare indentation and USP experiments for native and trypsinized ex-situ cartilage. b) Comparison of USP measurements with site-matched in-situ and ex-situ cartilage samples.

patellae were measured by in-situ hand-held USP (Fig. 5.3 a). The measurement sites were documented with the help of photography and sketches. Then, these measurement sites were prepared to achieve site-matched ex-situ cartilage samples (Fig. 5.3 b), to measure them again with USP (Fig. 5.4 b). Each USP measurement was repeated five times. Between in-situ and ex-situ measurements a time of 20-30 minutes was required, mainly for preparation of the sample. The samples were always kept in PBS to prevent dehydration effects.

Speed of sound under mechanical load

For these experiments, the USP transducer (prototype II) without the elastomer was mounted upside down at the BOSE material testing machine. The set-up is shown in Fig. 5.5 a) and b). The material testing machine was equipped with a linear actuator, a load cell (max. 225 N, ID 519713, Honeywell Model 31 Mid BN), and a flat-ended cylindrical indenter in series. The indenter was first moved until contacting the ultrasound transducer to obtain a reference point z_{ref} in displacement. A sample was put between the ultrasound transducer and the indenter. Its thickness was calculated from the difference of the z-position at first contact and z_{ref}. Since the BOSE system and the USP system are recording data independent from each other and with different samples rates, synchronization of the data was done in post-processing. Before and after the actual compression of the sample, a short -1-% strain was applied. In post-processing, both peaks were detected at z and TOF and matched. The displacement z and force F data from the BOSE system were interpolated to reach the same sampling frequency like the USP system (around 140 RF/s). A series of measurements were performed only with PBS between ultrasound transducer and indenter to tune the system and the evaluation algorithm. Subsequently, polyurethane samples of Shore A grade 30 and 60 as well as two cartilage

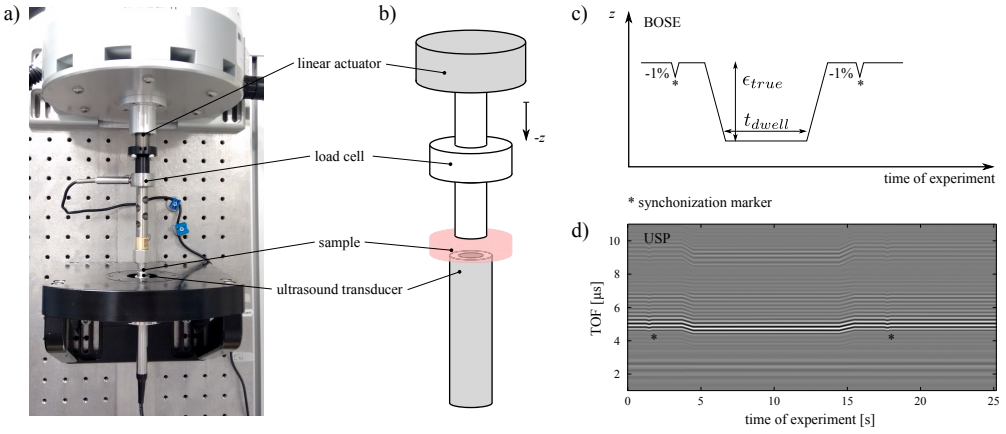

Figure 5.5 – a) Photography of the setup. b) Schematic drawing of the setup. c) Schematic displacement controlled by the BOSE material testing machine. d) M-mode visualization of the recorded pulse echoes with the USP.

samples were measured. The cartilage samples were obtained from porcine patellae, removed from the subchondral bone and cut in 10-mm diameter discs. The first cartilage sample was measured with different strain rates from 0.1 %/s to 10 %/s with a constant strain of 5 %. The second cartilage sample was measured with a strain rate of 2 %/s and different strains between 2.5 % to 15 %. Then this sample was stored for 4 hours in trypsin at 38°C. Subsequently, the measurements were repeated.
From the recorded pulse echoes the TOF was calculated by the phase-root seeking (PRS) method (see 5.2.1). Only for the first pulse echo of each experiment, the group delay method was used. From the measurements with PBS, the speed of sound was estimated by linear regression of $2z(t)/TOF(t)$. Based on the known distance between the ultrasound transducer and indenter $z - z_{ref}$ the TOF required for this path was calculated. The measured TOF is higher due to the unknown delay between triggering the digitization and pulse excitation and the actual sound exit from the transducer's surface. The delay was calculated by the difference between the measured TOF and the calculated TOF and then corrected in all subsequent measurements.

5.2.9 Statistics

Agreement between stiffness values from indentation and USP was quantified by linear regression analysis and Pearson's correlation coefficient. Significant differences in individual parameters between samples groups and users were evaluated based on a Kruskal-Wallis test with a significance level of $\alpha = 0.05$. This non-parametric test was selected because the data were mostly non-normally distributed. The two-way

random intra-class correlation (ICC) factor was calculated from the single measurements of each operator to quantify his individual *intra-operator* reliability. In contrast, the *inter-operator* reliability was calculated from the average stiffness for each sample and operator by the two-way random ICC. The statistical calculations were done with the Statistics Toolbox provided in MATLAB 2011b. ICC calculation was based on a function provided by Salarian (2017). The influence of preload and strain rate on the estimated stiffness values of USP measurements were evaluated by multivariate stepwise linear regression.

5.3 Results

5.3.1 Mechanical and acoustical properties of different elastomers

The characteristic parameters for elastomer hardness, mass density, and acoustical parameters are listed in Table 5.2 for 17 different materials. Most materials had a mass density around 1 g/cm^3 (median: 1.04 g/cm^3). The measured speed of sound varied more in the range of 1000 to 1800 m/s. The acoustic impedances ranged from 1.20 to 2.08 MRayl. Large differences were found for the attenuation. The acoustic parameters of the Pebax materials have been reported previously and are in good agreement with the values obtained in this study (Guess and Campbell, 1995).
Additionally, Figure 5.6 shows the spectral intensity of the pulse echoes through the different elastomers. The spectra are corrected to the individual sample thickness and normalized to the maximum intensity of Pebax 2533 which showed the lowest attenuation. The graph nicely demonstrates that the attenuation dominates at the high-frequency components. Compared to the analysis of the peak voltage, the overall spectral intensity of NuSil MED4980 appears superior to the other materials. This silicone showed a generally high intensity and the lowest losses in the higher frequencies.

5.3.2 Calibration

The calibration experiments with different deformation velocities showed that the displacement rate had no influence in the investigated range. The polynomial that represents the force calibration function was fitted to the loading curve that was driven by 0.5 mm/s. At a deformation of 0.5 mm deformation the maximum force of 25 N (stress: 3.5 N/mm^2) was recorded (Fig. 5.2 c). The entire loading and unloading cycle showed a clear hysteresis, but the initial length of the silicone tip was restored within less than a second.

Table 5.2 – Hardness, mass density and acoustical properties of different elastomer materials. [1] Values were obtained from the manufacturers' data sheet.

elastomer name	hardness[1] Shore A	SOS (m/s)	ρ[1] (g/cm^3)	Z (MRayl)	α (dB/cm)
Ebalta PU Shore A 30	30	1457.2	1.04	1.52	-12.72
Ebalta PU Shore A 50	50	1549.1	1.04	1.61	-28.81
Ebalta PU Shore A 60	60	1451.7	1.04	1.51	-22.05
Ebalta PU Shore A 70	70	1465.2	1.04	1.52	-26.67
Ebalta PU Shore A 80	80	1489.6	1.04	1.55	-32.64
NuSil MED4980 (1)	80	1029.4	1.17	1.20	-18.47
NuSil MED4980 (2)	80	1037.7	1.17	1.21	-18.93
Pebax 2533 SA 01	77	1565.3	1.00	1.57	-7.52
Pebax 3533 SA 01	82	1587.7	1.00	1.59	-11.37
Pebax 4033 SA 01	90	1677.2	1.00	1.68	-18.72
Pebax 4533 SA 01	92	1705.7	1.01	1.72	-20.16
Silpuran 6610 80	80	1008.4	1.26	1.27	-36.18
Silpuran 8020 70 (1)	70	1035.9	1.18	1.22	-19.31
Silpuran 8020 70 (2)	70	1020.2	1.18	1.20	-25.21
Tecoflex EG 93A	87	1813.1	1.08	1.96	-32.22
TT-1085A	85	1669.1	1.12	1.87	-32.31
TT-1095A	94	1808.0	1.15	2.08	-33.20
TT soft AR-62A	62	1627.1	0.99	1.61	-30.35
Versalloy XL9220 90	90	1674.3	0.94	1.57	-40.11

5.3.3 USP accuracy, reliability, and repeatability

Mounted vs. hand-held USP

Table 5.3 gives an overview of the stiffness results obtained from indentation and mounted and hand-held USP measurements. For five of the nine samples mounted and hand-held USP measurements showed significantly different stiffness. However, neither mounter nor hand-held USP showed higher or lower values in general. The average relative difference between mounted and hand-held derived USP measurement was $4.03 \pm 3.00\,\%$ and not significant. Very good agreement between hand-held and mounted USP stiffness estimation was confirmed by linear regression analysis, with a slope of 1.027 ± 0.026, $r = 0.9996$). The used preload and strain rate showed no significant difference and therefore can be considered as consistent for both mounted and hand-held setups.

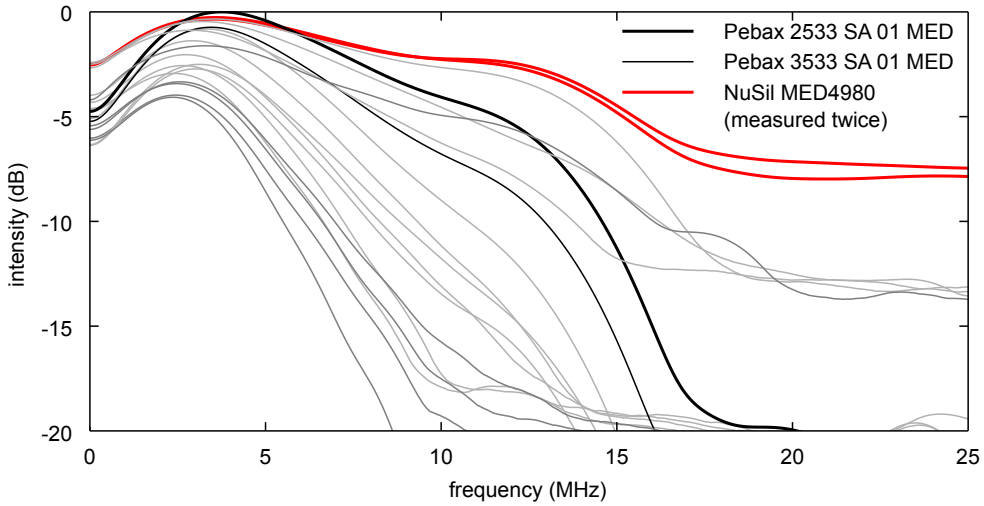

Figure 5.6 – Spectral intensity of the different elastomers corrected by the thickness of the individual samples. The spectra are normalized to the maximum intensity found for Pebax 2533 SA 01 MED. The selected material NuSil MED4980 was measured twice to confirm the low attenuation.

Accuracy and precision

The precision was quantified by the average coefficients of variation (CV) and was 0.8 % for indentation, 2.8 % for mounted and 4.0 % for hand-held USP measurements. The 2.1 mm sample of Shore A 30 showed a noticeably high value of 11.8 % for the hand-held USP measurements. A closer look at the individual data revealed a pronounced preconditioning effect for this sample, resulting in an increase of the derived stiffness value with each palpation. When excluding the first two palpations, CV was reduced to 2.9 % and therefore within the range of the other samples.
To visualize the accuracy, all mounted and hand-held USP measurements from each reference phantom were averaged and plotted against the average stiffness obtained from indentation (Fig. 5.7 a). Linear regression analysis from these data revealed very good agreement of USP with indentation ($r = 0.99$). The linear slope was 0.95 ± 0.15 and the offset was -0.53 $\pm$ 1.44 MPa.
The Bland-Altmann plot (Fig. 5.7 b) confirmed the agreement between USP and indentation. On average, the USP measurements underestimated the stiffness with -0.92 MPa compared to indentation. Furthermore, this visualization demonstrated that there is no stiffness dependency.

Table 5.3 – Results of indentation, mounted USP, and hand-held USP measurements on reference phantoms of different stiffness (Shore A) and thickness (d). The coefficient of variation (CV) is defined as the ratio of standard deviation (std) to the mean derived from n repeated measurements. The asterisk (*) indicates significant differences between mounted USP and hand-held USP with $p < 0.05$.

sample		**indentation**			**mounted USP**			**hand-held USP**			
			E (MPa)			E (MPa)			E (MPa)		
Shore A	d (mm)	n	mean ± std	CV	n	mean ± std	CV	n	mean ± std	CV	
30	2.1	5	0.61 ± 0.01	1.1 %	12	0.62 ± 0.03	4.5 %	12	0.66 ± 0.08	11.8 %	*
30	4.0	5	0.66 ± 0.00	0.6 %	12	0.50 ± 0.01	1.8 %	12	0.47 ± 0.01	1.3 %	*
50	4.1	5	4.69 ± 0.09	2.0 %	12	4.72 ± 0.07	1.5 %	12	4.79 ± 0.06	1.3 %	*
60	2.3	5	4.92 ± 0.02	0.4 %	12	3.71 ± 0.14	3.8 %	12	3.52 ± 0.12	3.3 %	*
60	3.1	10	4.49 ± 0.06	1.3 %	12	3.64 ± 0.06	1.5 %	12	3.69 ± 0.04	1.0 %	
70	2.1	5	9.97 ± 0.04	0.4 %	12	7.81 ± 0.22	2.8 %	12	7.73 ± 0.22	2.8 %	
70	3.1	5	10.07 ± 0.03	0.3 %	12	7.56 ± 0.10	1.4 %	12	7.61 ± 0.32	4.2 %	
80	2.0	5	16.20 ± 0.18	1.1 %	12	16.44 ± 0.24	1.4 %	12	17.11 ± 1.05	6.2 %	*
80	4.0	5	18.59 ± 0.06	0.3 %	12	16.82 ± 1.02	6.1 %	12	16.97 ± 0.64	3.8 %	

Table 5.4 – Results of USP experiments on a reference phantom (Shore A 60, d = 3.1 mm) of one experienced (ID 1) and four inexperienced (ID 2 - ID 5) users. The coefficient of variation (CV) is defined as the ratio of standard deviation (std) to the mean derived from n repeated measurements.

		E (MPa)		strain rate $\dot{\epsilon}$ (%/s)	
ID	n	mean ± std	CV	mean ± std	CV
1	10	3.65 ± 0.24	3.5 %	1.60 ± 0.24	15.1 %
2	10	3.81 ± 0.17	4.4 %	1.34 ± 0.17	12.9 %
3	10	3.75 ± 0.28	6.2 %	1.26 ± 0.28	22.2 %
4	10	3.85 ± 0.40	5.7 %	1.67 ± 0.40	24.2 %
5	10	3.56 ± 0.39	5.5 %	1.57 ± 0.39	24.6 %

Reliability

Table 5.4 summarises the experiments for the inter-operator reliability of one of the samples. Overall operators, the average CV of the measured stiffness was 5.1 %. The CV of the applied strain rates was approximately 4 times higher with 19.8 %. The inter-operator ICC values were in the range of 0.872 to 0.989 (mean 0.930) and inter-operator ICC was 0.996. Preload and strain rate were found to have no significant influence on the estimated stiffness.

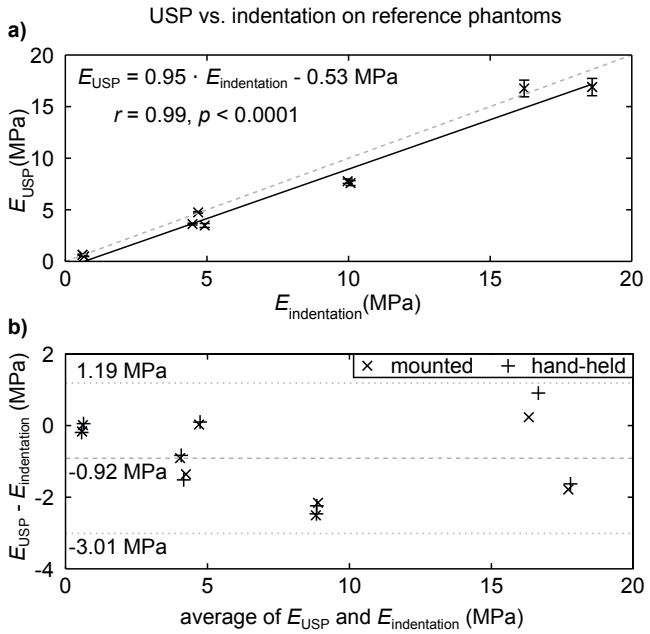

Figure 5.7 – a) Correlation between USP stiffness and indentation stiffness for the reference phantoms. Mounted and hand-held USP measurements are averaged for each sample. The positions and lengths of error bars represent the means and standard deviations of the repeated USP measurement on each sample, respectively. The dashed line represents the identity line. b) The Bland-Altman plot shows the comparison between USP and indentation measurements. Here, the results from mounted and hand-help USP measurements are plotted separately. The horizontal lines indicate the limits of agreement (mean ± the 1.96-fold standard deviation).

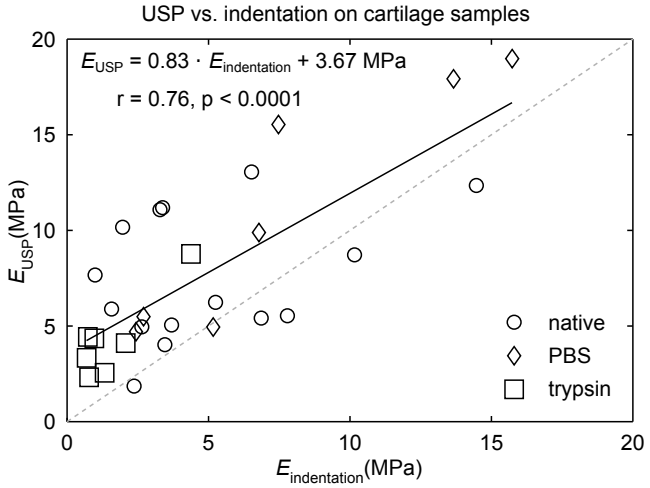

Figure 5.8 – Correlation between USP stiffness E_1 and indentation stiffness for the ex-situ cartilage samples measured in a native state and after trypsin treatment or after PBS immersion. The dashed line represents the identity line.

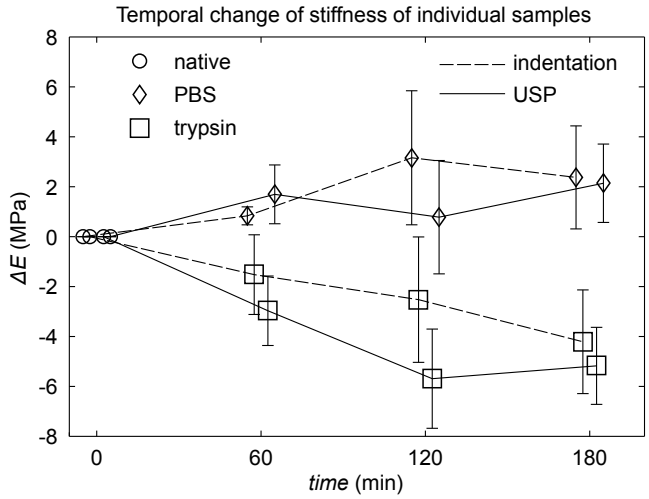

Figure 5.9 – Temporal stiffness changes measured by USP and indentation for PBS immersed and trypsinized full-thickness cartilage samples. The changes in stiffness of the first palpation to the native state $\Delta E = E_1 - E_{1,time=0}$ are plotted.

5.3.4 USP on cartilage samples

The correlation of the derived stiffness values obtained by USP and indentation is shown in Fig. 5.8 for native, trypsinized, and PBS immersed cartilage samples. The applied linear model indicates an overestimation of the USP measurements when considering the indentation values as reference. The slope of the fitted linear model was (0.83 ± 0.28) and the offset (3.67 ± 1.78) MPa.
In Fig. 5.9 the temporal change in stiffness induced by trypsinization or PBS immersion is plotted. As measured by both methods, the stiffness of the PBS immersed cartilage increased slightly. In contrast, the stiffness of the trypsinized cartilage decreased, as expected. The stiffness changes were not significantly different in both methods. The stiffness changes between PBS-immersed samples and trypsinized samples were found to be significant at 180 minutes for indentation and at 60 and 180 minutes for USP.
On cartilage, repeated USP measurements at one spot affect the measured stiffness and apparent thickness of the sample as shown for representative native and trypsin-degenerated samples in Fig. 5.10. In Fig. 5.10a) the stress-strain curves of 5 subsequent USP measurements are plotted. The corresponding normalized stiffness E_k/E_1 and normalized initial time of flight $\Delta t_{0,k}/\Delta t_{0,1}$ are shown in Fig. 5.10b). It is clearly visible that the slopes of E_k/E_1 and $\Delta t_{0,k}/\Delta t_{0,1}$ differ strongly between the native and the trypsinized sample. To quantify this slope, the parameters *relative change of thickness* (RCT) and *relative change of stiffness* (RCS) have been introduced. They describe the relative change of thickness and stiffness with each palpation, respectively.
Table 5.5 provides descriptive statistics of these parameters and other parameters

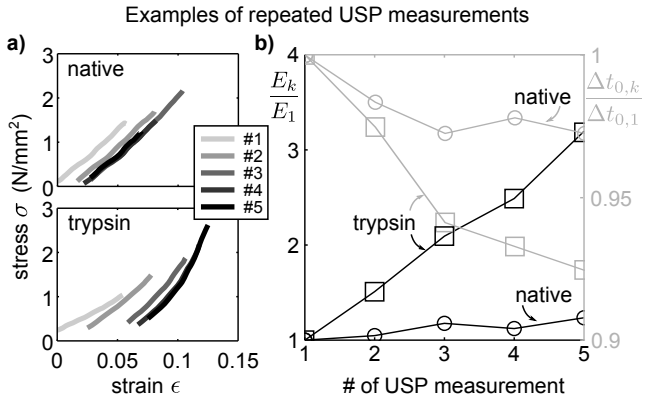

Figure 5.10 – a) Representative stress-strain curves for 5 subsequent USP measurements on native and trypsin treated ex-situ samples. b) Corresponding plot of the changes of stiffness and initial time of flight through the cartilage layer of the repeated USP measurements. The data were normalized to values obtained from the first palpation. With each palpation, the derived stiffness E increases and the initial time of flight Δt_0 decreases. Both effects were much stronger for the trypsin treated sample.

quantifying the measurement conditions. These data were collected from repeated USP measurements on the 27 native samples and for 11 repeated USP measurements on 5 ex-situ cartilage samples after they have been immersed in trypsin for different durations. The trypsinized cartilage showed significant lower stiffness values at the first USP measurement E_1, but an increased thickness reduction RCT and clearly larger stiffness increase RCS with repeated palpations. That indicates that the trypsinized cartilage samples are still in a compression state when starting the next palpation experiment. In contrast, native cartilage samples showed only a little stiffness increase RCS and nearly no thickness change RCT. The measurement conditions expressed as the time between repeated USP measurements ΔT, preload F_0, and maximum strain ϵ_{max} showed no significant differences between measurement on native and trypsinized cartilage (Table 5.5). Therefore, the influence of the measurement conditions on the results can be excluded.
The same parameters were acquired for the USP measurement on in-situ and ex-situ cartilage samples and are summarized in Tab. 5.6. Interestingly, the stiffness E_1 when derived in-situ was significantly larger than when derived ex-situ. The parameter RCS was, on average, negative for the in-situ experiments and significantly lower compared to the ex-situ measurements. The in-situ measurement were performed with lower strain rate $\dot{\epsilon}$ ($p < 0.05$) and larger time between subsequent palpations ΔT ($p < 0.05$) than the ex-situ experiments. The comparability of these experiments will be discussed later.

Table 5.5 – Parameters derived from USP measurements on native (n=27) and trypsinized (n=11) cartilage samples shown as median ± interquartile range. (* $p < 0.05$).

parameter	unit	native	trypsinized	
		measurement conditions		
ΔT	s	8.00 ± 1.17	6.25 ± 3.36	
F_0	N	1.90 ± 2.07	1.20 ± 1.55	
ϵ_{max}	%	4.96 ± 1.41	4.59 ± 1.64	
$\dot{\epsilon}$	%/s	2.22 ± 0.69	2.48 ± 1.10	
		results		
E_1	MPa	8.76 ± 5.64	4.14 ± 2.03	*
RCT	$\%/k$	-1.54 ± 1.80	-3.99 ± 2.28	*
RCS	$\%/k$	13.3 ± 19.2	50.4 ± 28.8	*

Table 5.6 – Parameters derived from USP measurements on in-situ (n=7) and ex-situ (n=7) cartilage samples shown as median ± interquartile range. (* $p < 0.05$)

parameter	unit	in-situ	ex-situ	
		measurement conditions		
ΔT	s	8.33 ± 2.25	6.25 ± 0.38	*
F_0	N	2.07 ± 1.21	1.90 ± 0.78	
ϵ_{max}	%	1.96 ± 1.18	5.61 ± 0.97	*
$\dot{\epsilon}$	%/s	0.75 ± 0.47	2.21 ± 0.46	*
		results		
E_1	MPa	12.11 ± 5.46	8.47 ± 5.92	*
RCT	$\%/k$	1.27 ± 1.51	-1.31 ± 1.23	*
RCS	$\%/k$	-8.81 ± 13.65	19.47 ± 28.71	*

5.3.5 Speed of sound under mechanical load

The delay between digitization and sound wave emission was found to be 0.5063 μs. By correcting for that delay, the speed of sound in PBS was found to be constant during these experiments for strain rates of 1, 2, 5 and 10 $\%/s$ (Fig. 5.11 a)). The polyurethane rubbers showed strain-dependent SOS decrease (Fig. 5.11 b-c), independent from the strain rate in the range 1-10 $\%/s$ (Fig. 5.11 d). The effect of SOS decrease was more visible for the stiffer polyurethane rubber. The values of relative SOS decrease with increasing strain are summarized in Table 5.7. The polyurethane rubbers showed no relaxation behavior. As long as the deformation was held, the reduced SOS remained unchanged.

Table 5.7 – Relative speed of sound change with strain of polyurethane rubber of different hardnesses.

elastomer	**strain**			
	2.5 %	5.0 %	10.0 %	15.0 %
PU Shore A 30	-0.25 %	-0.51 %	-1.08 %	-1.73 %
PU Shore A 60	-0.45 %	-0.76 %	-1.47 %	-2.46 %

Cartilage showed SOS decrease with increasing strain but independent from the strain rate (Fig. 5.12 a-b). During dwell time (holding the deformation), relaxation processes in cartilage led to slow SOS recovering (Fig. 5.12 a). The maximum SOS decrease was -1 % and therefore lower than for the PU samples and approximately half of the values reported by Lötjönen et al. measured on bovine cartilage (Lötjönen et al., 2009). After trypsinization, the cartilage sample showed a reduction in SOS decrease under mechanical load by a factor of 2 (Fig. 5.12 c).

5.4 Discussion

This study presents a new and innovative method for biomechanical testing of soft tissue, or more specifically, for testing of articular cartilage. Its big advantage is the possibility to perform in-situ measurements. Measuring the applied force based on ultrasound pulse time of flight through a deformable elastomer represent the key innovation of this method. Therefore, the force measurement is done directly at the site where the force is applied. As an additional advantage, it should be noted that only one data channel (the ultrasound pulse echoes) is required to record stress and strain.

The USP prototype in this study showed good results for the mounted and hand-held application. The stiffness values of reference samples obtained from USP

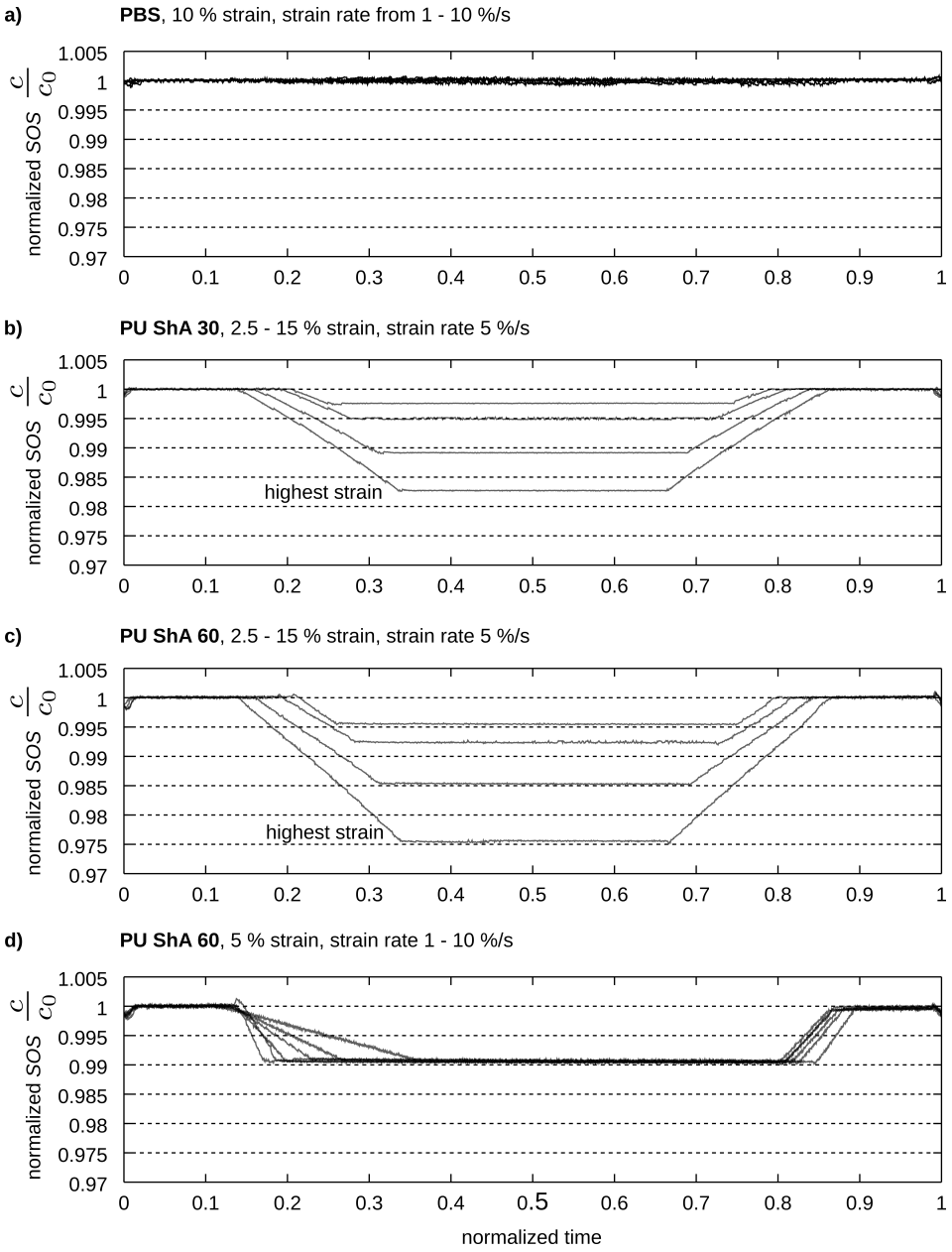

Figure 5.11 – Speed of sound during compression for PBS and polyurethane (PU) samples. a) The speed of sound changes were first recorded for PBS to validate this method. No changes in speed of sound were expected. b) Speed of sound changes during mechanical load of a soft PU sample (ShA 30) for different strains. c) Speed of sound changes for a stiffer PU sample (ShA 60) for different strains and d) for different strain rates.

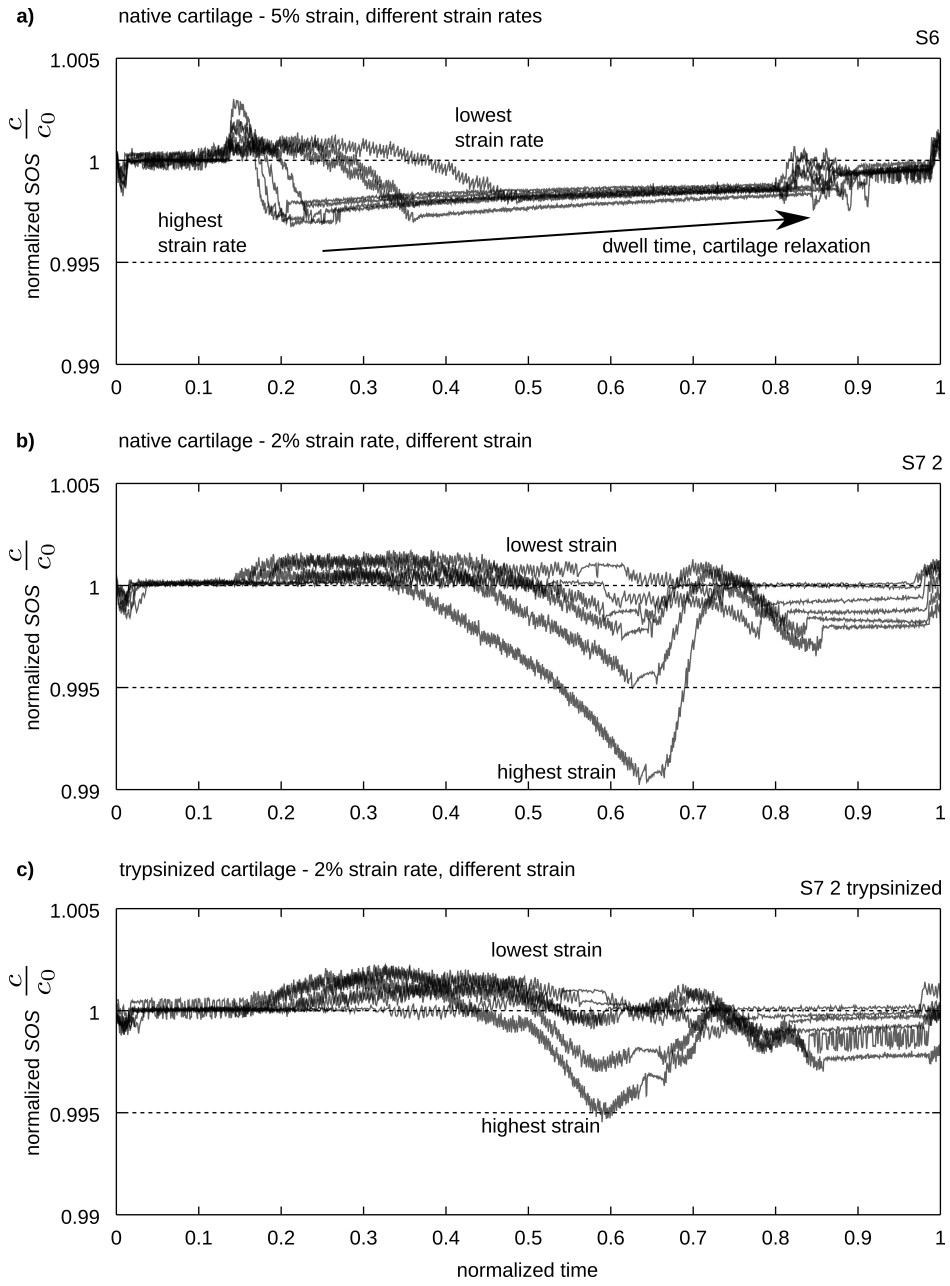

Figure 5.12 – Speed of sound during compression for cartilage samples. a) Speed of sound change of a native cartilage sample for constant strain but different strain rates. After the target strain was reached the deformation was hold (dwell time) and the cartilage relaxed. During this phase the speed of sound increased towards the initial values. The speed of sound changes for different strains but with a constant strain rate are shown in (b) and (c) for a native sample and the same sample after trypsinization, respectively.

measurements showed very good agreement with the values measured with a high-precision material testing system by conventional indentation. Therefore, the usage of the Hayes correction method can be approved for the application to USP measurements. The Hayes correction was introduced for experiments with a rigid indenter and the original work stated that this is a "serious restriction" to fulfill the assumption that all deformations occur in the cartilage layer (Hayes et al., 1972). Currently, the influence of using a deformable indenter material has not been investigated. Further investigations could analyze this by finite element simulations to optimize the Hayes correction specifically for USP.

The hand-held USP measurements by five users showed excellent intra- and inter-operator reliability. Interestingly, the values did not significantly differ between the experienced and the inexperienced users. Therefore it can be concluded that USP measurements are easy to learn and the results are less influenced by user experience. It is known that biomechanical measurements on cartilage depend strongly on measurement conditions, such as preload, strain rate, and maximum strain and load. Future improved versions of the USP system should provide software assistant measurements for better controlling these parameters.
The USP measurements on cartilage showed good correlation with the indentation experiments. However, the differences in the stiffness values were larger than for the reference phantoms. On cartilage, USP overestimates the stiffness when considering the stiffness obtained from indentation as correct values. However, biomechanical testing of articular cartilage is not simple and not standardized. The obtained results depend strongly on several boundary conditions, like pretreatment of the sample, the ionic concentration of the buffer medium (Chahine et al., 2004), testing with compression or indentation (Korhonen et al., 2002), absolute strain and strain rate (Li and Herzog, 2004). Important to note here is the difference in indenter radius (0.75 mm vs. 1.5 mm) and in the indenter material stiffness (steel vs. elastomer) of indentation and USP, respectively. Ideally, the influence of the indenter radius should be removed with the usage of the Hayes correction. The ex-situ USP measurements have been conducted with a strain rate of 1.8 - 2.0 %/s which is close to the strain rate of 2.5 %/s as used in the indentation tests. Regarding the work of Li et al., with a maximum strain of 5 %, these small strain rate differences can be neglected (Li and Herzog, 2004).
Additionally, a geometrical factor that could influence the stiffness results needs to be discussed. The surfaces of the excised cartilage samples are usually not parallel, due to the natural shape of the joint and curling of small detached cartilage samples (Mow and Guo, 2002). Such a slightly bent sample placed on a flat supporting plate does not have uniform contact. Therefore, a fraction of the applied force acts to bend the sample, but not to indent it. Therefore, the measured force is too low. This affects USP and indentation measurements. However, I assume that the effect is more severe for indentation measurements because the applied forces are smaller,

due to the smaller indenter radius. While in indentation the indenter was moved towards the sample until a slight force was measured, in the USP measurements the probe was placed onto the sample until a certain preload was reached. It is possible that the higher preload in USP was sufficient to bend the sample and bring it into proper contact with the supporting plate. Considering these, it seems reasonable that the USP measurement obtained higher stiffness values compared to indentation, especially for the soft cartilage samples.
The USP sensitivity was able to distinguish changes in cartilage stiffness that were caused by enzymatic degeneration of the proteoglycan network. These temporal stiffness changes were in agreement with the changes recorded by conventional indentation. It has been reported that cartilage digestion with trypsin is a process that starts at the surface and progresses with variable pace for different samples (Moody et al., 2006). Thus, the degree of degeneration differs between samples, although they have been immersed in the trypsin solution for the same time. Consequently, the observed stiffness changes vary as well.

As expected, ex-situ cartilage samples revealed a strongly different stiffness compared to site-matched in-situ samples. The cartilage for the in-situ measurements is very close to the normal physiological conditions. In contrast, the ex-situ samples are excised from their regular environment. The stiffness of USP measurements of in-situ samples was on average 43 % higher than those for respective ex-situ samples. Furthermore, the low RCS values for the in-situ measurements indicate that cartilage stiffness is very consistent as long as cartilage is in its natural condition. Furthermore, comparing the RCT values, it seems that in-situ cartilage relaxes faster than ex-situ samples. It is required to note that the in-situ measurements were more challenging to the operator, compared to the measurements of the ex-situ samples. For the in-situ measurement it was more complicated to align the USP probe in order to get a proper ultrasound signal. Furthermore, during the actual palpation it was likely to slip and therefore change the position of the probe. The pulse-echo signal intensity of the cartilage-bone interface is lower than for the cartilage-steel interface as for the ex-situ experiments. Additionally, some signal may be lost by the slightly curved shape of the patellae. All in all, the likelihood of losing the signal during the USP measurement is increased for the in-situ measurement. Because more care is required, the palpation is performed slower, which was noticed by a reduced strain rate and increased time between subsequent USP measurements (Table 5.6). It is known that a lower strain rate for cartilage measurements results in a reduced stiffness estimate (Li and Herzog, 2004). Therefore, I expect the differences between in-situ and ex-situ measured stiffness would even be larger when measuring both with the same strain rate.
The revealed differences further increase the importance of a biomechanical evaluation of cartilage directly at the articulating surface and not detached from the bone. It is obvious when excising cartilage from subchondral bone that the complex inter-

play between the cartilage components and their structure is significantly altered. Nevertheless, biomechanical testing of articular cartilage has mostly been performed on cartilage samples separated from the subchondral bone (Nieminen et al., 2007; Patwari et al., 2007; Föhr et al., 2012; Korhonen et al., 2002, 2003; Julkunen et al., 2008b; Chahine et al., 2004). Removing cartilage from bone is accompanied by another problem: it is nearly impossible to clearly separate cartilage from the bone. This was also a problem during this study as seen in Fig. 5.3b. A small amount of the lowest cartilage material usually remains on the bone site. Thus the radial layer thickness is reduced and thickness ratios of the three structural layers are altered as well as the entire cartilage thickness. Taken together, it was directly confirmed that detaching cartilage from bone changes the biomechanical behavior of cartilage, especially stiffness and relaxation.
Several studies used osteochondral cylinders for biomechanical testing of cartilage (Korhonen et al., 2002; Saarakkala et al., 2003; Abedian et al., 2013). Osteochondral cylinders are samples of bone that have been cut perpendicular to the joint surface including the articular cartilage. Therefore, the integrity of cartilage and subchondral bone is still intact. Therefore, I expect that osteochondral cylinders would show a smaller permeability and higher tensile strength of the collagen network compared to the ex-situ sample of this study. Based on that, I assume osteochondral cylinders would show larger stiffness caused by larger hydrostatic pressure and reduced water mobility, similar to in-situ cartilage. Further studies should investigate the comparability of measurements on osteochondral cylinders and in-situ measurements.

It has been shown that ultrasound is feasible for precise and non-destructive thickness estimation for articular cartilage when anatomical site and grade of degeneration are considered (Töyräs et al., 2003). The works of Nieminen and Lötjönen investigated the behavior of speed of sound (SOS) in articular cartilage under mechanical load (Nieminen et al., 2006, 2007; Lötjönen et al., 2009). They found an SOS decrease that is proportional to strain and that the strain rate has no effect on SOS. They also showed that even a small SOS decrease can cause much larger errors in the estimated strain when assuming SOS as constant. For example, they found a SOS decrease of 2.15 % that resulted in an error of the estimated strain up to −40 % (Lötjönen et al., 2009) (compare theoretical considerations in section 2.4.4). The SOS decrease between different samples of cartilage was very inconsistent, therefore a correction improved the strain estimation only slightly (Lötjönen et al., 2009). They also performed FEM simulations trying to explain the SOS decrease at mechanical load. This model based on changes in the collagen fiber orientation and alterations in the fluid-to-solid ratio, but could predict only half of the SOS decrease found experimentally (Nieminen et al., 2007; Lötjönen et al., 2009). Their experimental data were collected from healthy bovine ex-situ cartilage samples of the patella. It is very likely that SOS decrease is different for different grades of degeneration and between different species and even anatomical sites. Because there are so many unknowns, we decided not to apply SOS corrections to the

measurements of this study. Based on the preliminary tests that are in agreement with the reported SOS decrease, the strain estimate from USP measurements would be underestimated. Finally, the derived stiffness would be overestimated, which was actually found in the current study. The stiffness overestimation appeared more pronounced for the samples with lower stiffness. Based on that, it can be assumed that the SOS decrease is stronger for degenerated cartilage. Alterations in SOS during mechanical load of cartilage could also be a potential cause for the larger stiffness found in in-situ measurements of the present study (Tab. 5.7). Therefore, the SOS would need to decrease more in the in-situ samples than in the ex-situ samples. For follow-up studies, two points would be of interest: i) the origin of SOS decrease of articular cartilage under mechanical load, and ii) the behavior of SOS under mechanical load for different species, anatomical sites, and grades of degeneration. In the explanation of the force estimation (sec. 5.2.1) it was explained, that a constant contact area of the elastomer tip was used. However, in simple preliminary experiments it was observed, that the elastomer tip expands laterally under deformation. As elastomers have high Poisson's ratios (close to 0.5), they can be handled as nearly incompressible. That means that during deformation the volume remains constant. Therefore, the USP elastomer tip expands laterally when compressed in the axial direction. Eventually, the contact area increases as shown in preliminary experiments. However, when considering the increasing contact area, increase deviations in the derived stiffness were observed. It was assumed that the stress distribution is not homogeneous along the contact area. For follow-up experiments, I propose the definition of an effective contact area based on the estimation of the stress distribution in experiments. This would further increase the accuracy of the USP measurements.

The trypsin immersion of articular cartilage is often used to artificially create osteoarthritic cartilage (sec. 2.1.1). However, this is only an experimental model that mainly affects the proteoglycans. Pathologically, osteoarthritic changes also comprise degeneration of the collagen fibers, changes in the amount and morphology of the chondrocytes as well as an increased water content (Turunen et al., 2012). So it is not clear if native OA cartilage would show comparable biomechanical behavior to the trypsinized cartilage. However, to show that USP is capable of detecting stiffness changes caused by degeneration, this simple model of trypsinized cartilage was sufficient. To achieve a more realistic model of OA cartilage, mixtures of different enzymes can be used (Turunen et al., 2012). Two limitations of this study were i) the early removal of the joint capsule and ii) freezing the samples before the experiments. This caused loss of the synovial fluid which may change the ionic environment (third phase). Furthermore, a potentially negative influence of the freeze-thaw cycle on the biomechanical behavior cannot be excluded. It was shown that freezing cartilage once for 7 days has no influence on the biomechanics investigated by indentation and unconfined compression. The effects of long-term freezing or several freeze-thaw cycles are unknown (Changoor et al., 2010; Szarko et al.,

2010). A potential follow-up study should investigate the usage of the USP probe on fresh samples at open joints as in real operation theater settings and quantify the inter-observer agreement. As a first step, this could be done within an animal study. Eventually, USP measurements have to be done on human samples to evaluate the benefit of this investigation. Ideally, samples of different OA grades would be investigated and USP is compared to established classification systems (see study II).

Since the force estimation of the USP method is based on the deformation of the elastomer tip, this component is the most crucial one for the correct functionality of the USP probe. Sadly, the mechanical behavior of elastomers is known to depend on many factors, such as temperature, the maximum strain of previous deformations (Mullins effect, (Mullins, 1969)), and age of the material (Giese, 2014). It is important to recall that the calibrated USP probe is reliable only in a narrow range of internal and external parameters. Along with the mechanical stiffness, the acoustic impedance must also be chosen according to the acoustic properties of the material to test. However, the elastomer tip also brings several benefits. When designing the USP probe in such a way that the elastomer tip can be replaced, it is possible to change and adapt the measurement range easily. Furthermore, by using a new elastomer tip for each operation, constant mechanical conditions and sterility can be ensured.

In the last few decades, different methods have been introduced for in-situ testing of articular cartilage. Two similar approaches performed an indentation with a constant deformation depth predefined by the designs of the devices. The measurement result was the required force to reach the deformation of 300 μm (Lyyra et al., 1995) or a device-specific measure to reach 100 μm deformation (Niederauer et al., 2004). In both methods, it could be shown that their outcomes correlate with cartilage stiffness. Another approach used a water jet to apply deformation which was detected optically (Duda et al., 2004). Other researchers quantified the dynamic biomechanical response of cartilage when excited with a vibrational probe (Uchio et al., 2002; Appleyard et al., 2001). It was shown that these methods allow for reliable estimation of shear modulus and phase lag and that these parameters correlate to the degree of cartilage degeneration.
All mentioned methods share the fact that they do not consider cartilage thickness and that the estimated parameters are not comparable with other methods. The device from Lyyra et al. was later improved by replacing the indentation tip with an ultrasound transducer. This allowed for additional estimation of thickness and ultrasound reflectivity of the surface (as in study I) (Laasanen et al., 2002). I consider this device as most similar to the USP device presented here. However, force estimation and data evaluation were totally different and they did not record the entire stress-strain curve. In contrast to other studies, the stiffness values reported by Laasanen et al. as well as the USP based values of the present study were com-

parable and reproducible with reference material testing machines.
Two studies mentioned the coefficient of variation (CV) of the stiffness values obtained at elastomer phantoms with their probes: (Laasanen et al., 2002) reported a CV of 8.2 % and (Duda et al., 2004) a value of 7.3 %. Based on the CV of 4.0 % found for the USP measurements on the reference phantoms of the present study, it can be concluded that the USP measurements are twice as precise as the other methods.
For completion, two other arthroscopic devices should be mentioned that have been introduced to quantify the cartilage quality but are not based on biomechanical testing. The Arthro-BST from Biomomentum measures the streaming potentials that are induced by ionic flow caused by deformation of cartilage. It has been shown that the streaming potential integral decreases with cartilage degeneration (Abedian et al., 2013; Sim et al., 2014). A different approach was used by arthrospec GmbH: they used near-infrared spectroscopy (NIRS) in an arthroscopic probe and could show that the measurement outcomes are sensitive to cartilage degeneration (Spahn et al., 2007).
Lau et al. developed a hand-held probe for stiffness estimation for scar tissue (Lau et al., 2005). There are some similarities with the present USP device as well as with the device developed by Laasanen et al. (Laasanen et al., 2002). They used ultrasound to measure tissue strain and the applied force was measured with a load cell mounted at the back of the ultrasound transducer. Precise load cells cannot be miniaturized to fit into an arthroscopic probe tip, therefore Laasanen et al. used a strain gauge that measures deformation along the shaft of the arthroscopic probe.
Compared to all other hand-held biomechanical testing systems, the USP device presented here is the only device that allowed for real-time stress and strain measuring. The derived stiffness values are a device-independent measure and therefore comparable to conventional biomechanical tests. Additional advantages of USP are given by the replaceable elastomer tip. By using tips of different stiffness, the measurement range can easily be adjusted, maybe to measure the stiffness of much softer tissues. For clinical application, sterility and consistency are required and can easily be guaranteed with single-use USP tips. The simple fact that the ultrasound pulse echoes are only detected when the USP probe is aligned perpendicular to the cartilage layer allows for simple alignment control during palpation.

The USP method presented here could be adapted to other applications of biomechanical testing or more general mechanical testing. In the research field of tissue engineering, a lot of experiments are done in bioreactors. For example, in the creation of artificial cartilage grafts, several designs of bioreactors use adaptive mechanical stimulation and testing (Schulz and Bader, 2007), (Petersen et al., 2012). A bioreactor must be closed to prevent infection of the tissue engineered constructs. This gets complicated when the construct is excited by a defined mechanical stimulus or if the current scaffold stiffness is measured (Kock et al., 2009). USP measurements could

be performed on entirely sealed bioreactors as long as the sealing is deformable, i.e., made of a soft silicone. The silicone would couple the ultrasound waves into the bioreactor and applied stress and strain could be estimated as described for the USP method. It has already been shown that the speed of sound derived from pulse-echo measurements performed in a bioreactor can be correlated to the stiffness of different gels (Mansour et al., 2014).
Another interesting application for USP would be the quantification of cartilage repair tissue (compare Study II). Since USP is objective and non-destructive it could be used during regular follow-up to monitor the temporal change of the biomechanical competence. Experimental studies or preclinical trials would benefit especially since there is a lack of non-destructive, quantitative biomechanical methods. The current cartilage repair approaches do not result in tissue that equals native hyaline cartilage, instead, the tissue is described as hyaline-like or fibrous (Hunziker et al., 2015). Along with the structural composition, the biomechanical behavior and, as seen in study II, the tissue thickness is very important for the quality of the repair outcome. The eligibility of ultrasound for cartilage thickness estimation has already been shown (Jurvelin et al., 1995). The possibilities of quantification of cartilage repair tissue based on ultrasound data has also been shown (Gelse et al., 2010; Schöne et al., 2016).

As shown, repeated USP measurements at one spot could yield additional parameters that describe the biomechanical competence of articular cartilage. Therefore, the diagnostic value of USP could be increased with repeated measurements. However, further investigation would be required to better understand and interpret the detected changes in stiffness and thickness. Conventional biomechanical testing usually requires strict preconditioning and its large impact on the derived stress-strain curves has already been reported (Cheng et al., 2009). However, no study could provide data about the ideal preconditioning for articular cartilage. The USP experiments of the present study were done without preconditioning. Based on the interesting findings of the relative change of stiffness and thickness (RCS and RCT), preconditioning before USP experiments would probably cover information about the fluid phase and the collagen network integrity. With repeated USP measurements, single short-term biomechanical testing is extended to a time-dependent characterization of the cartilage relaxation behavior. When a palpation is performed while the cartilage sample has not recovered its initial thickness caused by a previous palpation, the derived thickness change is a measure of cartilage's relaxation ability. The parameter introduced in this study was the relative change of thickness (RCT) and is based on 3-5 subsequent palpations. This parameter differed clearly between native and degenerated cartilage samples. Healthy articular cartilage recovers very fast, therefore the RCT values are rather small. For trypsinized cartilage, the water attraction and therefore the restoration of the initial thickness is delayed which explains the increased RCT for trypsinized cartilage. This recovering after defor-

mation is also evaluated visually during arthroscopy by the naked eye.
When the cartilage has not entirely recovered after a first palpation and is measured again in this state, it can be considered pre-compressed. Based on cartilage's non-linear biomechanical behavior this results in an increased stiffness (Li and Herzog, 2004). Miller and Morgan also reported an increased stiffness derived from subsequent compression experiments on ex-situ cartilage discs (Miller and Morgan, 2010). This is in agreement with the results found in the present study quantified as relative change of stiffness RCS.

In conclusion, repeated USP measurements allow more information about the biomechanical behavior of cartilage than a single measurement. Thus, repeated USP measurements could provide additional diagnostic value. Follow-up experiments should evaluate the differences in these parameters for native and spontaneously degenerated articular cartilage.
In a clinical setup, the prototype of a pen-style USP probe presented in this study would allow for measurements on open knee joints only. To perform arthroscopic USP measurements the design needs to be miniaturized. It appears achievable to bring an ultrasound transducer into the tip of an arthroscopic probe, since a similar probe has already been shown by others (Lyyra et al., 1995),(Laasanen et al., 2002). Ideally, the tip would be angled and the elastomer replaceable.

6 Conclusion

The objectives of this thesis were to develop and evaluate new approaches to data evaluation of 3D UBM scans to provide improved possibilities in the quantification of native or repair cartilage tissue and to investigate the feasibility of a novel mechano-acoustic probe for the biomechanical characterization of cartilage. These objectives have been targeted with new ways of data evaluation and innovative experimental methods.

Study I of this thesis investigated the change of UBM surface parameters with respect to the local inclination of the sample. This was achieved by developing a robust method for surface detection based on scans with ultrasound pulse echoes. The established ultrasound surface parameters for surface reflectivity and roughness, IRC and URI, respectively, could then be mapped one-to-one to the local inclination. On idealized phantoms with different components of reflected and scattered signals, it was shown that only the reflected and not the scattered signals show strong inclination dependency. This is in alignment with the theory and was then applied to the evaluation of native, human cartilage samples of different grades of degeneration. Based on the inclination information, the parameterization of the cartilage surface was then restricted to low-inclination regions. Finally, I showed that the derived parameters are able to differentiate between the first grades of degeneration expressed by the histological grading scale according to Mankin and Lippiello (1970). This work was the basis of two other studies that used the information about the local surface inclination (Männicke et al., 2014a) and the derived surface parameters for the classification of articular cartilage (Männicke et al., 2014b). There are two important findings of this study to summarize: first, for reliable calculation of ultrasound surface parameters, the inclination must be controlled. Second, ultrasound-based surface parameters are sensitive to differentiate first grades of cartilage degeneration.

In the second study of this thesis, UBM scans were used to derive volumetric parameters for the quantification of cartilage repair outcomes. The surface detection method established in study I could be applied here, too. But further methods were developed to create a 3D reconstruction of cartilage surface, cartilage-bone interface, and the original defect boundaries for each repair region individually. Since this study was embedded in a large pre-clinical trial, the repair tissue was additionally quantified by established classification systems based on macroscopic evaluation, MR imaging, or histopathological evaluation. The defect filling, derived by UBM,

correlated very well to scores of all the established classification systems. Based on these findings, it can be concluded that the defect filling can be seen as a quality marker for the result of cartilage repair. Further, it was shown that UBM provides information that can not be seen by macroscopic evaluation (bony overgrowth), MRI resolution may not be sufficient for (filling), and histopathological evaluation is insufficient because it only evaluates a small section of the sample.

In study III, USP was introduced that allows for hand-held biomechanical testing of articular cartilage. The novelty of this method is that both the applied stress and strain are derived from the time of flight of ultrasound pulse echoes. This was achieved by the adaption of a method from ultrasound elastography to the RF signals acquired with a custom-made, pen-style USP probe. In the first part of the study, it was demonstrated how mechanical and acoustical parameters have to be chosen to allow for USP measurements on articular cartilage. Effects of friction and contact area increase during calibration were addressed. Finally, a USP prototype was developed, calibrated and verified, by measurements on reference phantoms and comparison to the measurements of conventional indentation experiments. This allowed for the verification of the applied correction function according to Hayes et al. (1972) and the estimation of repeatability and reliability of the USP measurements. Eventually, USP and indentation measurements on articular cartilage samples were conducted and compared. There it was shown that the USP measurements are sensitive to detect stiffness changes caused by enzymatic degeneration. Further, it was demonstrated that cartilage stiffness is higher when acquired at the intact joint surface than on an excised cartilage sample detached from the subchondral bone. Additionally, a way was shown to quantify cartilage relaxation based on repetitive USP measurements. On one hand, biomechanical testing with USP is much faster and simpler than conventional biomechanical testing. One the other hand, it does not achieve the same accuracy. However, in some cases, e.g. in a clinical setting, the advantages of USP, such as hand-held application and in-situ measurements within seconds predominate over higher accuracy.

6.1 Outlook

Study I and II both present novel methods of data evaluation that allow precise and objective characterization of cartilage degeneration grade or cartilage repair outcomes. Potentially, these findings or parts of these methods could be brought to an in-vivo application. There is an urgent demand for novel approachs to quantify cartilage degeneration status (Spahn et al., 2008, 2009) and the outcomes of cartilage repair approaches (Hunziker et al., 2015). The experimental setups used in these studies are not appropriate for intra-operative or even arthroscopic application. However, the arthroscopic acquisition of 2D ultrasound data from knee cartilage has

already been demonstrated (Kaleva et al., 2011; Liukkonen et al., 2014). When improving this method to prove 3D datasets, the estimation of surface parameters IRC and URI can be derived under control of inclination, and cartilage defects could be quantified volumetrically as described within this thesis. For the estimation of the surface parameters, uncovered access to the cartilage surface is inevitable. However, for the volumetric characterization transcutaneous application would also be feasible since only spatial information is required. One company is attempting to use a 2D intra-articular ultrasound in combination with an optical tracking system. This would allow for virtual positioning of the acquired ultrasound cross-sections and also for combining them with a 3D dataset (Cartimage Medical, Grenoble, France). Then the basic principles of surface parameter estimation, inclination determination, and volumetric quantification could be applied as well.
A further interesting approach is the evaluation of ultrasound backscatter. It has already been shown that ultrasound backscatter analysis can classify cartilage degeneration (Männicke et al., 2014b) and that cartilage repair tissue can be distinguished between fibrotic and hyaline-like (Gelse et al., 2010). It would be interesting to combine the approach of volumetric characterization and backscatter analysis to provide a qualitative description of the defect filling, i.e., provide the relative amount of fibrotic and hyaline-like repair tissue.

In the last part of this thesis, USP was introduced and verified as a novel method for biomechanical testing of articular cartilage. In comparison to conventional biomechanical testing, USP measurements can be conducted by hand, without samples preparation and within some seconds. Therefore, USP has a high potential to be applied intra-operatively. However, this first requires the development of a certified medical product. Potential improvements could be achieved by further investigations into the stress-strain distribution of the elastomer-cartilage interface and additionally considering an increase of contact area during palpation. Additional information about the cartilage sample could be achieved by using the elastomer-cartilage pulse echo for quantitative analysis of the reflectivity as shown in study I. Such a combination of a biomechanical tester with evaluation of the ultrasound pulse echoes has already been demonstrated (Laasanen et al., 2002). A more detailed investigation and understanding of the speed of sound changes in articular cartilage under mechanical load would be very interesting for the scientific community but would also improve the accuracy of USP.
The shared ultimate goal of the methods described in this thesis is arthroscopic application. This would allow for improved diagnostics and therefore support any treatment decision. Furthermore, individual follow-up measurements would allow for better monitoring of repair approaches and yield a suitable tool that supports research activities done on cartilage regeneration or restoration as requested by Hunziker (2015).

Bibliography

R. Abedian, E. Willbold, C. Becher, and C. Hurschler. In vitro electro-mechanical characterization of human knee articular cartilage of different degeneration levels: A comparison with ICRS and Mankin scores. *Journal of Biomechanics*, 46(7): 1328–1334, Apr. 2013.

A. M. Abraham, I. Goff, M. S. Pearce, R. M. Francis, and F. Birrell. Reliability and validity of ultrasound imaging of features of knee osteoarthritis in the community. *BMC Musculoskeletal Disorders*, 12:70, Apr. 2011.

R. S. Adler, D. K. Dedrick, T. J. Laing, E. H. Chiang, C. R. Meyer, P. H. Bland, and J. M. Rubin. Quantitative assessment of cartilage surface roughness in osteoarthritis using high frequency ultrasound. *Ultrasound in Medicine & Biology*, 18(1):51–58, 1992.

R. Altman, E. Asch, D. Bloch, G. Bole, D. Borenstein, K. Brandt, W. Christy, T. D. Cooke, R. Greenwald, M. Hochberg, D. Howell, D. Kaplan, W. Koopman, S. Longley, H. Mankin, D. J. McShane, T. Medsger, R. Meenan, W. Mikkelsen, R. Moskowitz, W. A. M. Jr, B. Rothschild, M. Segal, L. Sokoloff, and F. Wolfe. Development of criteria for the classification and reporting of osteoarthritis: Classification of osteoarthritis of the knee. *Arthritis & Rheumatism*, 29(8):1039–1049, Jan. 1986.

R. C. Appleyard, M. V. Swain, S. Khanna, and G. A. C. Murrell. The accuracy and reliability of a novel handheld dynamic indentation probe for analysing articular cartilage. *Physics in Medicine and Biology*, 46(2):541, Feb. 2001.

AQUA. Arthroskopie am Kniegelenk. Stellungnahmen der zur Stellungnahme berechtigten Organisationen nach §137a Abs. 3 SGB V, Dec. 2011.

Ärzteblatt. Infektionsrisiko bei Gelenkersatz auch nach Jahren vorhanden, July 2019. URL https://www.aerzteblatt.de/nachrichten/104605/Infektionsrisiko-bei-Gelenkersatz-auch-nach-Jahren-vorhanden.

K. A. Athanasiou, G. G. Niederauer, and R. C. Schenck. Biomechanical topography of human ankle cartilage. *Annals of Biomedical Engineering*, 23(5):697–704, Sept. 1995.

A. Benninghoff. *Form und Bau der Gelenkknorpel in ihren Beziehungen zur Funktion: Zweiter Teil: Der Aufbau des Gelenkknorpels in seinen Beziehungen zur Funktion*, volume 2. Zeitschrift für Zellforschung und Mikroskopische Anatomie, 1925.

J. C. Bernhard and G. Vunjak-Novakovic. Should we use cells, biomaterials, or tissue engineering for cartilage regeneration? *Stem Cell Research & Therapy*, 7, Apr. 2016.

A. J. Blackman, M. V. Smith, D. C. Flanigan, M. J. Matava, R. W. Wright, and R. H. Brophy. Correlation Between Magnetic Resonance Imaging and Clinical Outcomes After Cartilage Repair Surgery in the Knee A Systematic Review and Meta-analysis. *The American Journal of Sports Medicine*, 41(6):1426–1434, June 2013.

D. E. Bonasia, A. Marmotti, A. D. F. Massa, A. Ferro, D. Blonna, F. Castoldi, and R. Rossi. Intra- and inter-observer reliability of ten major histological scoring systems used for the evaluation of in vivo cartilage repair. *Knee Surgery, Sports Traumatology, Arthroscopy*, pages 1–10, Apr. 2014.

A. Briggs. *Acoustic microscopy*. Oxford University Press, Oxford, New York, 1992. ISBN 978-0-19-851377-3.

R. Brignardello-Petersen, G. H. Guyatt, R. Buchbinder, R. W. Poolman, S. Schandelmaier, Y. Chang, B. Sadeghirad, N. Evaniew, and P. O. Vandvik. Knee arthroscopy versus conservative management in patients with degenerative knee disease: a systematic review. *BMJ Open*, 7(5):e016114, May 2017.

F. Bronner and M. C. Farach-Carson, editors. *Bone and osteoarthritis*. Number v. 4 in Topics in bone biology. Springer, London, 2007. ISBN 978-1-84628-513-4.

M. D. Buschmann and D. B. F. Saris. Introduction to the International Cartilage Repair Society Recommendation Papers. *Cartilage*, 2(2):99–99, Apr. 2011.

N. P. Camacho, P. West, P. A. Torzilli, and R. Mendelsohn. FTIR microscopic imaging of collagen and proteoglycan in bovine cartilage. *Biopolymers*, 62(1):1–8, Nov. 2000.

M. L. Cameron, K. K. Briggs, and J. R. Steadman. Reproducibility and Reliability of the Outerbridge Classification for Grading Chondral Lesions of the Knee Arthroscopically. *The American Journal of Sports Medicine*, 31(1):83–86, Jan. 2003.

R. K. Chaganti and N. E. Lane. Risk factors for incident osteoarthritis of the hip and knee. *Current Reviews in Musculoskeletal Medicine*, 4(3):99–104, Aug. 2011.

N. Chahine, C. Wang, C. Hung, and G. Ateshian. Anisotropic strain-dependent material properties of bovine articular cartilage in the transitional range from tension to compression. *Journal Of Biomechanics*, 37(8):1251–1261, 2004.

A. Changoor, L. Fereydoonzad, A. Yaroshinsky, and M. D. Buschmann. Effects of Refrigeration and Freezing on the Electromechanical and Biomechanical Properties of Articular Cartilage. *Journal of Biomechanical Engineering*, 132(6):064502–064502, Apr. 2010.

S. Cheng, E. C. Clarke, and L. E. Bilston. The effects of preconditioning strain on measured tissue properties. *Journal of Biomechanics*, 42(9):1360–1362, June 2009.

E. H. Chiang, R. S. Adler, C. R. Meyer, J. M. Rubin, D. K. Dedrick, and T. J. Laing. Quantitative assessment of surface roughness using backscattered ultrasound: The effects of finite surface curvature. *Ultrasound in Medicine & Biology*, 20(2):123–135, 1994.

E. Chérin, A. Säied, P. Laugier, P. Netter, and G. Berger. Evaluation of Acoustical Parameter Sensitivity to Age-Related and Osteoarthritic Changes in Articular Cartilage Using 50-MHz Ultrasound. *Ultrasound in Medicine & Biology*, 24(3): 341–354, Mar. 1998.

W. S. Cleveland. Robust Locally Weighted Regression and Smoothing Scatterplots. *Journal of the American Statistical Association*, 74(368):829–836, Dec. 1979.

B. T. Cox, J. G. Laufer, P. C. Beard, and S. R. Arridge. Quantitative spectroscopic photoacoustic imaging: a review. *Journal of Biomedical Optics*, 17(6):061202, June 2012.

J. L. Davis. *Mathematics of Wave Propagation*. Princeton University Press, May 2000. ISBN 978-0-691-02643-5.

I. A. Dekkers, R. Roos, and A. J. v. d. Molen. Gadolinium retention after administration of contrast agents based on linear chelators and the recommendations of the European Medicines Agency. *European Radiology*, 28(4):1579–1584, Apr. 2018.

M. Delgado-Rodríguez and J. Llorca. Bias. *Journal of Epidemiology and Community Health*, 58(8):635–641, Jan. 2004.

W. Demtröder. *Mechanik und Wärme*. Number 1 in Experimentalphysik. Springer, Berlin, 3., neu bearb. und aktualisierte aufl., korrigierter nachdr. edition, 2004. ISBN 978-3-540-43559-4.

G. N. Duda, R. U. Kleemann, U. Bluecher, and A. Weiler. A New Device to Detect Early Cartilage Degeneration. *The American Journal of Sports Medicine*, 32(3): 693–698, Jan. 2004.

J. R. Ebert, A. Smith, M. Fallon, D. J. Wood, and T. R. Ackland. Correlation Between Clinical and Radiological Outcomes After Matrix-Induced Autologous Chondrocyte Implantation in the Femoral Condyles. *The American Journal of Sports Medicine*, 42(8):1857–1864, Aug. 2014.

Eurpoean Medicines Agency. Reflection paper on in-vitro cultured chondrocyte containing products for cartilage repair of the knee, 2010. URL http://www.ema.europa.eu/docs/en_GB/document_library/Scientific_guideline/2010/05/WC500090887.pdf.

P. Föhr, V. Hautmann, P. Prodinger, F. Pohlig, C. Kaddick, and R. Burgkart. Hochdynamisches Prüfsystem zur biomechanischen Charakterisierung von Knorpel und seinen Regeneraten. *Der Orthopäde*, 41(10):820–826, Oct. 2012.

Food and Drug Administration. Cellular & Gene Therapy Guidances - Draft Guidance for Industry: Preparation of IDEs and INDs for Products Intended to Repair or Replace Knee Cartilage, 2009. URL http://www.fda.gov/BiologicsBloodVaccines/GuidanceComplianceRegulatoryInformation/Guidances/CellularandGeneTherapy/ucm072952.htm.

R. Fujioka, T. Aoyama, and T. Takakuwa. The layered structure of the articular surface. *Osteoarthritis and Cartilage*, 21(8):1092–1098, Aug. 2013.

K. Gelse, A. Olk, S. Eichhorn, B. Swoboda, M. Schoene, and K. Raum. Quantitative ultrasound biomicroscopy for the analysis of healthy and repair cartilage tissue. *European Cells & Materials*, 19:58–71, 2010.

J. M. Gere and B. J. Goodno. *Mechanics of Materials*. Cengage Learning, Jan. 2012. ISBN 978-1-111-57773-5.

U. Giese. Aging Behavior of Elastomers. In S. Kobayashi and K. Müllen, editors, *Encyclopedia of Polymeric Nanomaterials*, pages 1–7. Springer Berlin Heidelberg, Berlin, Heidelberg, 2014. ISBN 978-3-642-36199-9.

S. Glyn-Jones, A. J. R. Palmer, R. Agricola, A. J. Price, T. L. Vincent, H. Weinans, and A. J. Carr. Osteoarthritis. *The Lancet*, 386(9991):376–387, July 2015.

L. Goebel, D. Zurakowski, A. Müller, D. Pape, M. Cucchiarini, and H. Madry. 2d and 3d MOCART scoring systems assessed by 9.4 t high-field MRI correlate with elementary and complex histological scoring systems in a translational model of osteochondral repair. *Osteoarthritis and Cartilage*, 22(10):1386–1395, Oct. 2014.

A. H. Gomoll, H. Madry, G. Knutsen, N. v. Dijk, R. Seil, M. Brittberg, and E. Kon. The subchondral bone in articular cartilage repair: current problems in the surgical management. *Knee Surgery, Sports Traumatology, Arthroscopy*, 18(4):434–447, Apr. 2010.

A. Guermazi, H. Alizai, M. D. Crema, S. Trattnig, R. R. Regatte, and F. W. Roemer. Compositional MRI techniques for evaluation of cartilage degeneration in osteoarthritis. *Osteoarthritis and Cartilage*, 23(10):1639–1653, Oct. 2015.

J. F. Guess and J. S. Campbell. Acoustic properties of some biocompatible polymers at body temperature. *Ultrasound in Medicine & Biology*, 21(2):273–277, 1995.

M. I. Haller and B. T. Khuri-Yakub. A surface micromachined electrostatic ultrasonic air transducer. *IEEE Transactions on Ultrasonics, Ferroelectrics, and Frequency Control*, 43(1):1–6, Jan. 1996.

C. W. Han, C. R. Chu, N. Adachi, A. Usas, F. H. Fu, J. Huard, and Y. Pan. Analysis of rabbit articular cartilage repair after chondrocyte implantation using optical coherence tomography. *Osteoarthritis and Cartilage*, 11(2):111–121, Feb. 2003.

J. Hassenpflug, editor. *Handbuch Sportorthopädie, -traumatologie*. Number 157 in Beiträge zur Lehre und Forschung im Sport. Hofmann, Schorndorf, 2007. ISBN 978-3-7780-4570-1.

W. Hayes, L. Keer, G. Herrmann, and L. Mockros. A mathematical analysis for indentation tests of articular cartilage. *Journal of Biomechanics*, 5(5):541–551, Sept. 1972.

P. Hepp, G. Osterhoff, M. Niederhagen, B. Marquass, T. Aigner, A. Bader, C. Josten, and R. Schulz. Perilesional changes of focal osteochondral defects in an ovine model and their relevance to human osteochondral injuries. *J Bone Joint Surg Br*, 91-B(8):1110–1119, Aug. 2009.

C. D. Hoemann, C.-H. Lafantaisie-Favreau, V. Lascau-Coman, G. Chen, and J. Guzmán-Morales. The cartilage-bone interface. *The Journal of Knee Surgery*, 25(2):85–97, May 2012.

S. M. Hosseini, M. B. Veldink, K. Ito, and C. C. v. Donkelaar. Is collagen fiber damage the cause of early softening in articular cartilage? *Osteoarthritis and Cartilage*, 21(1):136–143, Jan. 2013.

Y.-P. Huang, S. Saarakkala, J. Toyras, L.-K. Wang, J. S. Jurvelin, and Y.-P. Zheng. Effects of optical beam angle on quantitative optical coherence tomography (OCT) in normal and surface degenerated bovine articular cartilage. *Physics in Medicine and Biology*, 56(2):491–509, Jan. 2011.

E. B. Hunziker. Articular cartilage repair: basic science and clinical progress. A review of the current status and prospects. *Osteoarthritis and Cartilage*, 10(6): 432–463, June 2002.

E. B. Hunziker, K. Lippuner, M. J. B. Keel, and N. Shintani. An educational review of cartilage repair: precepts & practice – myths & misconceptions – progress & prospects. *Osteoarthritis and Cartilage*, 23(3):334–350, Mar. 2015.

M. B. Hurtig, M. D. Buschmann, L. A. Fortier, C. D. Hoemann, E. B. Hunziker, J. S. Jurvelin, P. Mainil-Varlet, C. W. McIlwraith, R. L. Sah, and R. A. Whiteside. Preclinical Studies for Cartilage Repair: Recommendations from the International Cartilage Repair Society. *Cartilage*, 2(2):137–152, Apr. 2011.

M. F. Insana and T. J. Hall. Parametric ultrasound imaging from backscatter coefficient measurements: Image formation and interpretation. *Ultrasonic Imaging*, 12(4):245–267, Oct. 1990.

M. F. Insana, R. F. Wagner, D. G. Brown, and T. J. Hall. Describing small-scale structure in random media using pulse-echo ultrasound. *The Journal of the Acoustical Society of America*, 87(1):179–192, 1990.

J. J. Irrgang, A. F. Anderson, A. L. Boland, C. D. Harner, M. Kurosaka, P. Neyret, J. C. Richmond, and K. D. Shelborne. Development and Validation of the International Knee Documentation Committee Subjective Knee Form. *The American Journal of Sports Medicine*, 29(5):600–613, Jan. 2001.

D. W. Jackson, P. A. Lalor, H. M. Aberman, and T. M. Simon. Spontaneous Repair of Full-Thickness Defects of Articular Cartilage in a Goat Model A Preliminary Study. *The Journal of Bone & Joint Surgery*, 83(1):53–53, Jan. 2001.

J. A. Jensen. A model for the propagation and scattering of ultrasound in tissue. *The Journal of the Acoustical Society of America*, 89(1):182–190, Jan. 1991.

P. Julkunen, R. K. Korhonen, W. Herzog, and J. S. Jurvelin. Uncertainties in indentation testing of articular cartilage: A fibril-reinforced poroviscoelastic study. *Medical Engineering & Physics*, 30(4):506–515, May 2008a.

P. Julkunen, W. Wilson, J. S. Jurvelin, J. Rieppo, C.-J. Qu, M. J. Lammi, and R. K. Korhonen. Stress–relaxation of human patellar articular cartilage in unconfined compression: Prediction of mechanical response by tissue composition and structure. *Journal of Biomechanics*, 41(9):1978–1986, 2008b.

J. S. Jurvelin, T. Räsänen, P. Kolmonens, and T. Lyyra. Comparison of optical, needle probe and ultrasonic techniques for the measurement of articular cartilage thickness. *Journal of Biomechanics*, 28(2):231–235, Feb. 1995.

E. Kaleva, S. Saarakkala, J. Jurvelin, T. Virén, and J. Töyräs. Effects of Ultrasound Beam Angle and Surface Roughness on the Quantitative Ultrasound Parameters of Articular Cartilage. *Ultrasound in Medicine & Biology*, 35(8):1344–1351, Aug. 2009a.

E. Kaleva, J. Toyras, J. Jurvelin, T. Viren, and S. Saarakkala. Effects of ultrasound frequency, temporal sampling frequency, and spatial sampling step on the quantitative ultrasound parameters of articular cartilage. *IEEE Transactions on Ultrasonics, Ferroelectrics and Frequency Control*, 56(7):1383 –1393, July 2009b.

E. Kaleva, T. Virén, S. Saarakkala, J. Sahlman, J. Sirola, J. Puhakka, T. Paatela, H. Kröger, I. Kiviranta, J. S. Jurvelin, and J. Töyräs. Arthroscopic Ultrasound Assessment of Articular Cartilage in the Human Knee Joint. *Cartilage*, 2(3):246 –253, July 2011.

H. I. Keen and P. G. Conaghan. Ultrasonography in Osteoarthritis. *Radiologic Clinics of North America*, 47(4):581–594, July 2009.

H. K. W. Kim, P. S. Babyn, K. A. Harasiewicz, H. K. Gahunia, K. P. H. Pritzker, and F. S. Foster. Imaging of immature articular cartilage using ultrasound backscatter microscopy at 50 MHz. *Journal of Orthopaedic Research*, 13(6):963–970, 1995.

S. Kim, J. Bosque, J. P. Meehan, A. Jamali, and R. Marder. Increase in Outpatient Knee Arthroscopy in the United States: A Comparison of National Surveys of Ambulatory Surgery, 1996 and 2006. *The Journal of Bone & Joint Surgery*, 93 (11):994–1000, June 2011.

R. Kleemann, D. Krocker, A. Cedraro, J. Tuischer, and G. Duda. Altered cartilage mechanics and histology in knee osteoarthritis: relation to clinical assessment (ICRS Grade). *Osteoarthritis and Cartilage*, 13(11):958–963, Nov. 2005.

L. M. Kock, R. M. Schulz, C. C. van Donkelaar, C. B. Thümmler, A. Bader, and K. Ito. RGD-dependent integrins are mechanotransducers in dynamically compressed tissue-engineered cartilage constructs. *Journal of Biomechanics*, 42(13): 2177–2182, Sept. 2009.

J. L. Koh, K. Wirsing, E. Lautenschlager, and L.-Q. Zhang. The Effect of Graft Height Mismatch on Contact Pressure Following Osteochondral Grafting A Biomechanical Study. *The American Journal of Sports Medicine*, 32(2):317–320, Jan. 2004.

R. K. Korhonen, M. S. Laasanen, J. Töyräs, J. Rieppo, J. Hirvonen, H. J. Helminen, and J. S. Jurvelin. Comparison of the equilibrium response of articular cartilage in unconfined compression, confined compression and indentation. *Journal of Biomechanics*, 35(7):903–909, July 2002.

R. K. Korhonen, M. S. Laasanen, J. Töyräs, R. Lappalainen, H. J. Helminen, and J. S. Jurvelin. Fibril reinforced poroelastic model predicts specifically mechanical behavior of normal, proteoglycan depleted and collagen degraded articular cartilage. *Journal of Biomechanics*, 36(9):1373–1379, Sept. 2003.

H. Krieger and W. Petzold. *Strahlenphysik, Dosimetrie und Strahlenschutz. 1: Grundlagen: mit 81 Tabellen und 40 Beispielen*. Teubner, Stuttgart, 4., völlig neubearb. u. erw. aufl edition, 1998. ISBN 978-3-519-33052-3.

J. Kunz and M. Studer. Druck-Elastizitätsmodul über Shore-A-Härte ermitteln. *Kunststoffe*, 96(6):92–94, 2006.

I. Kutzner, B. Heinlein, F. Graichen, A. Bender, A. Rohlmann, A. Halder, A. Beier, and G. Bergmann. Loading of the knee joint during activities of daily living measured in vivo in five subjects. *Journal of Biomechanics*, 43(11):2164–2173, Aug. 2010.

M. Laasanen, J. Töyräs, R. Korhonen, J. Rieppo, S. Saarakkala, M. Nieminen, J. Hirvonen, and J. Jurvelin. Biomechanical properties of knee articular cartilage. *Biorheology*, 40(1):133–140, Jan. 2003.

M. S. Laasanen, J. T$ouml$yr$auml$s, J. Hirvonen, S. Saarakkala, R. K. Korhonen, M. T. Nieminen, I. Kiviranta, and J. S. Jurvelin. Novel mechano-acoustic technique and instrument for diagnosis of cartilage degeneration. *Physiological Measurement*, 23:491–503, Aug. 2002.

M. S. Laasanen, S. Saarakkala, J. Töyräs, J. Rieppo, and J. S. Jurvelin. Site-specific ultrasound reflection properties and superficial collagen content of bovine knee articular cartilage. *Physics in Medicine and Biology*, 50:3221–3233, July 2005.

M. S. Laasanen, J. Töyräs, A. Vasara, S. Saarakkala, M. M. Hyttinen, I. Kiviranta, and J. S. Jurvelin. Quantitative ultrasound imaging of spontaneous repair of porcine cartilage. *Osteoarthritis and Cartilage*, 14(3):258–263, Mar. 2006.

I. Ladabaum, X. Jin, H. T. Soh, A. Atalar, and B. t. Khuri-Yakub. Surface micromachined capacitive ultrasonic transducers. *IEEE Transactions on Ultrasonics, Ferroelectrics, and Frequency Control*, 45(3):678–690, May 1998.

S. Lakshmanan, T. Koch, S. Brand, N. Männicke, M. Wicke, D. Mörlein, and K. Raum. Prediction of the intramuscular fat content in loin muscle of pig carcasses by quantitative time-resolved ultrasound. *Meat Science*, 90(1):216–225, Jan. 2012.

L. D. Latt, R. R. Glisson, H. E. Montijo, F. G. Usuelli, and M. E. Easley. Effect of Graft Height Mismatch on Contact Pressures With Osteochondral Grafting of the Talus. *The American Journal of Sports Medicine*, 39(12):2662–2669, Dec. 2011.

J. C. Lau, C. W. Li-Tsang, and Y. Zheng. Application of tissue ultrasound palpation system (TUPS) in objective scar evaluation. *Burns*, 31(4):445–452, June 2005.

S. Leicht and K. Raum. Acoustic impedance changes in cartilage and subchondral bone due to primary arthrosis. *Ultrasonics*, 48(6–7):613–620, Nov. 2008.

L. P. Li and W. Herzog. Strain-rate dependence of cartilage stiffness in unconfined compression: the role of fibril reinforcement versus tissue volume change in fluid pressurization. *Journal of Biomechanics*, 37(3):375–382, Mar. 2004.

S. Linn, B. Murtaugh, and E. Casey. Role of Sex Hormones in the Development of Osteoarthritis. *PM&R*, 4(5):S169–S173, May 2012.

J. Liukkonen, P. Lehenkari, J. Hirvasniemi, A. Joukainen, T. Virén, S. Saarakkala, M. T. Nieminen, J. S. Jurvelin, and J. Töyräs. Ultrasound Arthroscopy of Human Knee Cartilage and Subchondral Bone in Vivo. *Ultrasound in Medicine & Biology*, 40(9):2039–2047, Sept. 2014.

F. L. Lizzi, M. Greenebaum, E. J. Feleppa, M. Elbaum, and D. J. Coleman. Theoretical framework for spectrum analysis in ultrasonic tissue characterization. *The Journal of the Acoustical Society of America*, 73(4):1366–1373, Apr. 1983.

F. L. Lizzi, E. J. Feleppa, S. Kaisar Alam, and C. X. Deng. Ultrasonic spectrum analysis for tissue evaluation. *Pattern Recognition Letters*, 24(4–5):637–658, Feb. 2003.

O. Lopez, K. K. Amrami, A. Manduca, and R. L. Ehman. Characterization of the dynamic shear properties of hyaline cartilage using high-frequency dynamic MR elastography. *Magnetic Resonance in Medicine*, 59(2):356–364, Feb. 2008.

P. Lötjönen, P. Julkunen, J. Töyräs, M. J. Lammi, J. S. Jurvelin, and H. J. Nieminen. Strain-Dependent Modulation of Ultrasound Speed in Articular Cartilage Under Dynamic Compression. *Ultrasound in Medicine & Biology*, 35(7):1177–1184, July 2009.

X. L. Lu and V. C. Mow. Biomechanics of articular cartilage and determination of material properties. *Medicine and Science in Sports and Exercise*, 40(2):193–199, Feb. 2008.

X. L. Lu, L. Q. Wan, X. Edward Guo, and V. C. Mow. A linearized formulation of triphasic mixture theory for articular cartilage, and its application to indentation analysis. *Journal of Biomechanics*, 43(4):673–679, Mar. 2010.

T. Lyyra, J. Jurvelin, P. Pitkänen, U. Väätäinen, and I. Kiviranta. Indentation instrument for the measurement of cartilage stiffness under arthroscopic control. *Medical Engineering & Physics*, 17(5):395–399, July 1995.

J. Mamou, A. Coron, M. L. Oelze, E. S. Beecroft, M. Hata, P. Lee, J. Machi, E. Yanagihara, P. Laugier, and E. J. Feleppa. Three-dimensional High-frequency Backscatter and Envelope Quantification of Cancerous Human Lymph Nodes. *Ultrasound in medicine & biology*, 37(3):345–357, Mar. 2011.

H. J. Mankin and L. Lippiello. Biochemical and Metabolic Abnormalities in Articular Cartilage from Osteo-Arthritic Human Hips. *The Journal of Bone and Joint Surgery (American)*, 52(3):424–434, Apr. 1970.

N. Männicke. High-frequency ultrasound backscatter analysis of hyaline cartilage. *Dissertation, FU Berlin*, 2018.

N. Männicke, M. Schöne, M. Gottwald, F. Göbel, M. L. Oelze, and K. Raum. 3-D High-Frequency Ultrasound Backscatter Analysis of Human Articular Cartilage. *Ultrasound in Medicine & Biology*, 40(1):244–257, Jan. 2014a.

N. Männicke, M. Schöne, M. Oelze, and K. Raum. Articular cartilage degeneration classification by means of high-frequency ultrasound. *Osteoarthritis and Cartilage*, 22(10):1577–1582, Oct. 2014b.

N. Männicke, M. Schöne, J. Liukkonen, D. Fachet, S. Inkinen, M. K. Malo, M. L. Oelze, J. Töyräs, J. S. Jurvelin, and K. Raum. Species-Independent Modeling of High-Frequency Ultrasound Backscatter in Hyaline Cartilage. *Ultrasound in Medicine & Biology*, 42(6):1375–1384, June 2016.

J. M. Mansour, D.-W. M. Gu, C.-Y. Chung, J. Heebner, J. Althans, S. Abdalian, M. D. Schluchter, Y. Liu, and J. F. Welter. Towards the Feasibility of Using Ultrasound to Determine Mechanical Properties of Tissues in a Bioreactor. *Annals of Biomedical Engineering*, 42(10):2190–2202, Aug. 2014.

H. Maradit Kremers, D. R. Larson, C. S. Crowson, W. K. Kremers, R. E. Washington, C. A. Steiner, W. A. Jiranek, and D. J. Berry. Prevalence of Total Hip and Knee Replacement in the United States. *The Journal of Bone and Joint Surgery. American volume*, 97(17):1386–1397, Sept. 2015.

S. Marlovits, G. Striessnig, C. T. Resinger, S. M. Aldrian, V. Vecsei, H. Imhof, and S. Trattnig. Definition of pertinent parameters for the evaluation of articular cartilage repair tissue with high-resolution magnetic resonance imaging. *European Journal of Radiology*, 52(3):310–319, Dec. 2004.

S. Marlovits, P. Singer, P. Zeller, I. Mandl, J. Haller, and S. Trattnig. Magnetic resonance observation of cartilage repair tissue (MOCART) for the evaluation of autologous chondrocyte transplantation: Determination of interobserver variability and correlation to clinical outcome after 2 years. *European Journal of Radiology*, 57(1):16–23, Jan. 2006.

B. Marquass, R. Schulz, P. Hepp, M. Zscharnack, T. Aigner, S. Schmidt, F. Stein, R. Richter, G. Osterhoff, G. Aust, C. Josten, and A. Bader. Matrix-Associated Implantation of Predifferentiated Mesenchymal Stem Cells Versus Articular Chondrocytes In Vivo Results of Cartilage Repair After 1 Year. *The American Journal of Sports Medicine*, 39(7):1401–1412, July 2011.

O. E. Mattiat. *Ultrasonic Transducer Materials*. Springer Science & Business Media, Mar. 2013. ISBN 978-1-4757-0468-6.

G. J. Miller and E. F. Morgan. Use of microindentation to characterize the mechanical properties of articular cartilage: comparison of biphasic material properties across length scales. *Osteoarthritis and Cartilage*, 18(8):1051–1057, Aug. 2010.

I. Möller, D. Bong, E. Naredo, E. Filippucci, I. Carrasco, C. Moragues, and A. Iagnocco. Ultrasound in the study and monitoring of osteoarthritis. *Osteoarthritis and Cartilage*, 16, Supplement 3:S4–S7, Oct. 2008.

H. R. Moody, C. P. Brown, J. C. Bowden, R. W. Crawford, D. L. S. McElwain, and A. O. Oloyede. In vitro degradation of articular cartilage: does trypsin treatment produce consistent results? *Journal of Anatomy*, 209(2):259–267, Aug. 2006.

J. B. Moseley, K. O'Malley, N. J. Petersen, T. J. Menke, B. A. Brody, D. H. Kuykendall, J. C. Hollingsworth, C. M. Ashton, and N. P. Wray. A Controlled Trial of Arthroscopic Surgery for Osteoarthritis of the Knee. *New England Journal of Medicine*, 347(2):81–88, July 2002.

V. Mow, M. Gibbs, W. Lai, W. Zhu, and K. Athanasiou. Biphasic indentation of articular cartilage—II. A numerical algorithm and an experimental study. *Journal of Biomechanics*, 22(8-9):853–861, 1989.

V. C. Mow and a. X. E. Guo. Mechano-Electrochemical Properties Of Articular Cartilage: Their Inhomogeneities and Anisotropies. *Annual Review of Biomedical Engineering*, 4(1):175–209, 2002.

V. C. Mow, M. H. Holmes, and W. Michael Lai. Fluid transport and mechanical properties of articular cartilage: A review. *Journal of Biomechanics*, 17(5):377–394, 1984.

L. Mullins. Softening of Rubber by Deformation. *Rubber Chemistry and Technology*, 42(1):339–362, Mar. 1969.

S. Nebelung, N. Brill, U. Marx, V. Quack, M. Tingart, Schmitt Robert, Rath Björn, and Jahr Holger. Three-dimensional imaging and analysis of human cartilage degeneration using Optical Coherence Tomography. *Journal of Orthopaedic Research*, 33(5):651–659, Jan. 2015.

C. P. Neu. Functional imaging in OA: role of imaging in the evaluation of tissue biomechanics. *Osteoarthritis and Cartilage*, 22(10):1349–1359, Oct. 2014.

G. G. Niederauer, G. M. Niederauer, L. C. Cullen, K. A. Athanasiou, J. B. Thomas, and M. Q. Niederauer. Correlation of Cartilage Stiffness to Thickness and Level of Degeneration Using a Handheld Indentation Probe. *Annals of Biomedical Engineering*, 32(3):352–359, 2004.

P. Niemeyer, K. Schweigler, B. Grotejohann, J. Maurer, P. Angele, M. Aurich, C. Becher, J. Fay, R. Feil, S. Fickert, J. Fritz, A. Hoburg, P. Kreuz, T. Kolombe, J. Laskowski, J. Lützner, S. Marlovits, P. E. Müller, T. Niethammer, M. Pietschmann, K. Ruhnau, G. Spahn, T. Tischer, W. Zinser, and D. Albrecht. [The German Cartilage Registry (KnorpelRegister DGOU) for Evaluation of Surgical Treatment for Cartilage Defects: Experience after Six Months Including First Demographic Data]. *Zeitschrift Für Orthopädie Und Unfallchirurgie*, 153 (1):67–74, Feb. 2015.

H. J. Nieminen, J. Töyräs, J. Rieppo, M. T. Nieminen, J. Hirvonen, R. Korhonen, and J. S. Jurvelin. Real-time ultrasound analysis of articular cartilage degradation in vitro. *Ultrasound in Medicine & Biology*, 28(4):519–525, Apr. 2002.

H. J. Nieminen, J. Töyräs, M. S. Laasanen, and J. S. Jurvelin. Acoustic properties of articular cartilage under mechanical stress. *Biorheology*, 43(3-4):523–535, 2006.

H. J. Nieminen, P. Julkunen, J. Töyräs, and J. S. Jurvelin. Ultrasound Speed in Articular Cartilage Under Mechanical Compression. *Ultrasound in Medicine & Biology*, 33(11):1755–1766, Nov. 2007.

H. J. Nieminen, Y. Zheng, S. Saarakkala, Q. Wang, J. Toyras, Y. Huang, and J. Jurvelin. Quantitative assessment of articular cartilage using high-frequency ultrasound: research findings and diagnostic prospects. *Critical Reviews in Biomedical Engineering*, 37(6):461–494, 2009.

S. W. O'Driscoll, F. W. Keeley, and R. B. Salter. Durability of regenerated articular cartilage produced by free autogenous periosteal grafts in major full-thickness defects in joint surfaces under the influence of continuous passive motion. A follow-up report at one year. *The Journal of Bone & Joint Surgery*, 70(4):595–606, Apr. 1988.

B. P. O'Hara, J. P. Urban, and A. Maroudas. Influence of cyclic loading on the nutrition of articular cartilage. *Annals of the Rheumatic Diseases*, 49(7):536–539, July 1990.

J. Ophir, I. Céspedes, H. Ponnekanti, Y. Yazdi, and X. Li. Elastography: A quantitative method for imaging the elasticity of biological tissues. *Ultrasonic Imaging*, 13(2):111–134, Apr. 1991.

R. E. Outerbridge. The Etiology of Chondromalacia Patellae. *Journal of Bone & Joint Surgery, British Volume*, 43-B(4):752–757, Jan. 1961.

A. M. Parfitt, M. K. Drezner, F. H. Glorieux, J. A. Kanis, H. Malluche, P. J. Meunier, S. M. Ott, and R. R. Recker. Bone histomorphometry: Standardization of nomenclature, symbols, and units: Report of the asbmr histomorphometry nomenclature committee. *Journal of Bone and Mineral Research*, 2(6):595–610, Dec. 1987.

S. Patil and S. R. Tapasvi. Osteochondral autografts. *Current Reviews in Musculoskeletal Medicine*, 8(4):423–428, Sept. 2015.

P. Patwari, D. M. Cheng, A. A. Cole, K. E. Kuettner, and A. J. Grodzinsky. Analysis of the Relationship between Peak Stress and Proteoglycan Loss following Injurious Compression of Human Post-mortem Knee and Ankle Cartilage. *Biomechanics and Modeling in Mechanobiology*, 6(1-2):83–89, Jan. 2007.

B. Pellaumail, A. Watrin, D. Loeuille, P. Netter, G. Berger, P. Laugier, and A. Saïd. Effect of articular cartilage proteoglycan depletion on high frequency ultrasound backscatter. *Osteoarthritis and Cartilage*, 10(7):535–541, July 2002.

A. Pesavento, C. Perrey, M. Krueger, and H. Ermert. A time-efficient and accurate strain estimation concept for ultrasonic elastography using iterative phase zero estimation. *IEEE Transactions on Ultrasonics, Ferroelectrics, and Frequency Control*, 46(5):1057–1067, Sept. 1999.

A. Petersen, P. Joly, C. Bergmann, G. Korus, and G. N. Duda. The Impact of Substrate Stiffness and Mechanical Loading on Fibroblast-Induced Scaffold Remodeling. *Tissue Engineering Part A*, 18(17-18):1804–1817, Sept. 2012.

J. Podlipská, A. Guermazi, P. Lehenkari, J. Niinimäki, F. W. Roemer, J. P. Arokoski, P. Kaukinen, E. Liukkonen, E. Lammentausta, M. T. Nieminen, O. Tervonen, J. M. Koski, and S. Saarakkala. Comparison of Diagnostic Performance of Semi-Quantitative Knee Ultrasound and Knee Radiography with MRI: Oulu Knee Osteoarthritis Study. *Scientific Reports*, 6:22365, Mar. 2016.

P. H. Puhakka, N. C. R. t. Moller, P. Tanska, S. Saarakkala, V. Tiitu, R. K. Korhonen, H. Brommer, T. Virén, J. S. Jurvelin, and J. Töyräs. Optical coherence tomography enables accurate measurement of equine cartilage thickness for determination of speed of sound. *Acta Orthopaedica*, 0(0):1–7, May 2016.

K. Raum and W. O'Brien. Pulse-echo field distribution measurement technique for high-frequency ultrasound sources. *IEEE Transactions On Ultrasonics Ferroelectrics And Frequency Control*, 44(4):810–815, July 1997.

K. Raum, A. Ozguler, S. Morris, and W. O'Brien. Channel defect detection in food packages using integrated backscatter ultrasound imaging. *IEEE Transactions on Ultrasonics, Ferroelectrics, and Frequency Control*, 45(1):30–40, Jan. 1998.

K. Raum, R. O. Cleveland, F. Peyrin, and P. Laugier. Derivation of elastic stiffness from site-matched mineral density and acoustic impedance maps. *Physics in Medicine & Biology*, 51(3):747, 2006.

K. Raum, M. Schöne, and P. Varga. Ultrasonic palpator, measurement system and kit comprising the same, method for determining a property of an object, method for operating and method for calibrating a palpator, 2013.

J.-Y. Rho. An ultrasonic method for measuring the elastic properties of human tibial cortical and cancellous bone. *Ultrasonics*, 34(8):777–783, Dec. 1996.

B. F. Riecke, R. Christensen, S. Torp-Pedersen, M. Boesen, H. Gudbergsen, and H. Bliddal. An ultrasound score for knee osteoarthritis: a cross-sectional validation study. *Osteoarthritis and Cartilage*, 22(10):1675–1691, Oct. 2014.

L. Rieppo, J. Rieppo, J. S. Jurvelin, and S. Saarakkala. Fourier Transform Infrared Spectroscopic Imaging and Multivariate Regression for Prediction of Proteoglycan Content of Articular Cartilage. *PLoS ONE*, 7(2):e32344, Feb. 2012.

D. Rohrbach, S. I. Inkinen, J. Zatloukalová, A. Kadow-Romacker, A. Joukainen, M. K. Malo, J. Mamou, J. Töyräs, and K. Raum. Regular chondrocyte spacing is a potential cause for coherent ultrasound backscatter in human articular cartilage. *The Journal of the Acoustical Society of America*, 141(5):3105, May 2017.

E. M. Roos, H. P. Roos, L. S. Lohmander, C. Ekdahl, and B. D. Beynnon. Knee Injury and Osteoarthritis Outcome Score (KOOS)–development of a self-administered outcome measure. *The Journal of orthopaedic and sports physical therapy*, 28(2):88–96, Aug. 1998.

M. Rutgers, M. van Pelt, W. Dhert, L. Creemers, and D. Saris. Evaluation of histological scoring systems for tissue-engineered, repaired and osteoarthritic cartilage. *Osteoarthritis and Cartilage*, 18(1):12–23, Jan. 2010.

S. Saarakkala, M. S. Laasanen, J. S. Jurvelin, K. Törrönen, M. J. Lammi, R. Lappalainen, and J. Töyräs. Ultrasound indentation of normal and spontaneously degenerated bovine articular cartilage. *Osteoarthritis and Cartilage*, 11(9):697–705, Sept. 2003.

S. Saarakkala, R. K. Korhonen, M. S. Laasanen, J. Töyräs, J. Rieppo, and J. S. Jurvelin. Mechano-acoustic determination of Young's modulus of articular cartilage. *Biorheology*, 41(3-4):167–179, 2004a.

S. Saarakkala, J. Töyräs, J. Hirvonen, M. S. Laasanen, R. Lappalainen, and J. S. Jurvelin. Ultrasonic quantitation of superficial degradation of articular cartilage. *Ultrasound in Medicine & Biology*, 30(6):783–792, June 2004b.

S. Saarakkala, M. S. Laasanen, J. S. Jurvelin, and J. Töyräs. Quantitative ultrasound imaging detects degenerative changes in articular cartilage surface and subchondral bone. *Physics in Medicine and Biology*, 51:5333–5346, Oct. 2006.

S. Saarakkala, P. Waris, V. Waris, I. Tarkiainen, E. Karvanen, J. Aarnio, and J. M. Koski. Diagnostic performance of knee ultrasonography for detecting degenerative changes of articular cartilage. *Osteoarthritis and Cartilage*, 20(5):376–381, May 2012.

A. Salarian. Intraclass Correlation Coefficient (ICC) - File Exchange - MATLAB Central, 2017. URL http://ch.mathworks.com/matlabcentral/fileexchange/22099-intraclass-correlation-coefficient--icc-.

M. J. Salzler, A. Lin, C. D. Miller, S. Herold, J. J. Irrgang, and C. D. Harner. Complications After Arthroscopic Knee Surgery. *The American Journal of Sports Medicine*, 42(2):292–296, Feb. 2014.

M. Schöne, N. Männicke, M. Gottwald, F. Göbel, and K. Raum. 3-D High-Frequency Ultrasound Improves the Estimation of Surface Properties in Degenerated Cartilage. *Ultrasound in Medicine & Biology*, 39(5):834–844, May 2013.

M. Schöne, N. Männicke, J. S. Somerson, B. Marquaß, R. Henkelmann, T. Aigner, K. Raum, and R. M. Schulz. 3d ultrasound biomicroscopy for assessment of cartilage repair tissue: volumetric characterisation and correlation to established classification systems. *European Cells & Materials*, 31:119–135, 2016.

M. Schöne, R. M. Schulz, H. Tzschätzsch, P. Varga, and K. Raum. Ultrasound palpation for fast in-situ quantification of articular cartilage stiffness, thickness and relaxation capacity. *Biomechanics and Modeling in Mechanobiology*, pages 1–15, Feb. 2017.

R. M. Schulz and A. Bader. Cartilage tissue engineering and bioreactor systems for the cultivation and stimulation of chondrocytes. *European Biophysics Journal*, 36 (4-5):539–568, Feb. 2007.

M. D. Shoulders and R. T. Raines. COLLAGEN STRUCTURE AND STABILITY. *Annual review of biochemistry*, 78:929–958, 2009.

P. J. Shull. *Nondestructive Evaluation: Theory, Techniques, and Applications*. CRC Press, July 2016. ISBN 978-0-203-91106-8.

F. H. Silver and G. Bradica. Mechanobiology of cartilage: how do internal and external stresses affect mechanochemical transduction and elastic energy storage? *Biomechanics and Modeling in Mechanobiology*, 1(3):219–238, Dec. 2002.

S. Sim, A. Chevrier, M. Garon, E. Quenneville, A. Yaroshinsky, C. D. Hoemann, and M. D. Buschmann. Non-destructive electromechanical assessment (Arthro-BST) of human articular cartilage correlates with histological scores and biomechanical properties. *Osteoarthritis and Cartilage*, 22(11):1926–1935, Nov. 2014.

J. G. Skedros, R. D. Bloebaum, M. W. Mason, and D. M. Bramble. Analysis of a tension/compression skeletal system: Possible strain-specific differences in the hierarchical organization of bone. *The Anatomical Record*, 239(4):396–404, Aug. 1994.

M. D. Smith. The Normal Synovium. *The Open Rheumatology Journal*, 5:100–106, Dec. 2011.

G. Spahn, H. Plettenberg, E. Kahl, H. M. Klinger, T. Mückley, and G. O. Hofmann. Near-infrared (NIR) spectroscopy. A new method for arthroscopic evaluation of low grade degenerated cartilage lesions. Results of a pilot study. *BMC Musculoskeletal Disorders*, 8(1):47, May 2007.

G. Spahn, H. Plettenberg, H. Nagel, E. Kahl, H. M. Klinger, T. Mückley, M. Günther, G. O. Hofmann, and J. A. Mollenhauer. Evaluation of cartilage defects with near-infrared spectroscopy (NIR): An ex vivo study. *Medical Engineering & Physics*, 30(3):285–292, Apr. 2008.

G. Spahn, H. M. Klinger, and G. O. Hofmann. How valid is the arthroscopic diagnosis of cartilage lesions? Results of an opinion survey among highly experienced arthroscopic surgeons. *Archives of Orthopaedic and Trauma Surgery*, 129(8):1117–1121, Aug. 2009.

G. Spahn, H. M. Klinger, M. Baums, M. Hoffmann, H. Plettenberg, A. Kroker, and G. O. Hofmann. Near-Infrared Spectroscopy for Arthroscopic Evaluation of Cartilage Lesions Results of a Blinded, Prospective, Interobserver Study. *The American Journal of Sports Medicine*, 38(12):2516–2521, Dec. 2010.

G. Spahn, H. M. Klinger, M. Baums, U. Pinkepank, and G. O. Hofmann. Reliability in arthroscopic grading of cartilage lesions: results of a prospective blinded study for evaluation of inter-observer reliability. *Archives of Orthopaedic and Trauma Surgery*, 131(3):377–381, Mar. 2011.

G. Spahn, G. Felmet, and G. O. Hofmann. Traumatic and degenerative cartilage lesions: arthroscopic differentiation using near-infrared spectroscopy (NIRS). *Archives of Orthopaedic and Trauma Surgery*, 133(7):997–1002, July 2013.

T. D. Spector and A. J. MacGregor. Risk factors for osteoarthritis: genetics1. *Osteoarthritis and Cartilage*, 12:39–44, Jan. 2004.

J. Staubesand, E.-G. Afting, A. Benninghoff, K. Fleischhauer, and K. Goerttler, editors. *Cytologie, Histologie, allgemeine Anatomie und Anatomie des Bewegungsapparates*. Number begr. von Alfred Benninghoff. Fortgef. von Kurt Goerttler ... Hrsg. u. neubearb. von Kurt Fleischhauer ... ; Bd. 1 in Makroskopische und mikroskopische Anatomie des Menschen. Urban & Schwarzenberg, München, 14., völlig neubearb. aufl edition, 1985. ISBN 978-3-541-00244-3.

M. Szarko, K. Muldrew, and J. E. Bertram. Freeze-thaw treatment effects on the dynamic mechanical properties of articular cartilage. *BMC Musculoskeletal Disorders*, 11:231, 2010.

H. M. D. Tkaczuk. Human Cartilage Stiffness: In Vivo Studies. *Clinical Orthopaedics & Related Research*, 206:301–312, May 1986.

J. Töyräs, M. S. Laasanen, S. Saarakkala, M. J. Lammi, J. Rieppo, J. Kurkijärvi, R. Lappalainen, and J. S. Jurvelin. Speed of sound in normal and degenerated bovine articular cartilage. *Ultrasound in Medicine & Biology*, 29(3):447–454, Mar. 2003.

A. S. Tunis, G. J. Czarnota, A. Giles, M. D. Sherar, J. W. Hunt, and M. C. Kolios. Monitoring structural changes in cells with high-frequency ultrasound signal statistics. *Ultrasound in Medicine & Biology*, 31(8):1041–1049, Aug. 2005.

S. M. Turunen, M. J. Lammi, S. Saarakkala, S.-K. Han, W. Herzog, P. Tanska, and R. K. Korhonen. The effect of collagen degradation on chondrocyte volume and morphology in bovine articular cartilage following a hypotonic challenge. *Biomechanics and Modeling in Mechanobiology*, 12(3):417–429, June 2012.

H. Tzschätzsch, T. Elgeti, K. Rettig, C. Kargel, R. Klaua, M. Schultz, J. Braun, and I. Sack. In Vivo Time Harmonic Elastography of the Human Heart. *Ultrasound in Medicine & Biology*, 38(2):214–222, Feb. 2012.

H. Tzschätzsch, S. Ipek-Ugay, M. Nguyen Trong, J. Guo, J. Eggers, E. Gentz, T. Fischer, M. Schultz, J. Braun, and I. Sack. Multifrequency Time-Harmonic Elastography for the Measurement of Liver Viscoelasticity in Large Tissue Windows. *Ultrasound in Medicine & Biology*, 41(3):724–733, Mar. 2015.

Y. Uchio, M. Ochi, N. Adachi, K. Kawasaki, and J. Iwasa. Arthroscopic assessment of human cartilage stiffness of the femoral condyles and the patella with a new tactile sensor. *Medical Engineering & Physics*, 24(6):431–435, July 2002.

J. A. van der Sluijs, R. G. T. Geesink, A. J. van der Linden, S. K. Bulstra, R. Kuyer, and J. Drukker. The reliability of the mankin score for osteoarthritis. *Journal of Orthopaedic Research*, 10(1):58–61, Jan. 1992.

F. Vanhoenacker, N. D. Vos, and P. V. Dyck. Common Mistakes and Pitfalls in Magnetic Resonance Imaging of the Knee. *Journal of the Belgian Society of Radiology*, 100(1):99, Nov. 2016.

T. Viren, S. Saarakkala, V. Tiitu, J. Puhakka, I. Kiviranta, J. S. Jurvelin, and J. Toyras. Ultrasound evaluation of mechanical injury of bovine knee articular cartilage under arthroscopic control. *IEEE Transactions on Ultrasonics, Ferroelectrics, and Frequency Control*, 58(1):148–155, Jan. 2011.

T. Virén, S. Saarakkala, J. S. Jurvelin, H. J. Pulkkinen, V. Tiitu, P. Valonen, I. Kiviranta, M. J. Lammi, and J. Töyräs. Quantitative Evaluation of Spontaneously and Surgically Repaired Rabbit Articular Cartilage Using Intra-Articular Ultrasound Method in situ. *Ultrasound in Medicine & Biology*, 36(5):833–839, May 2010.

T. Virén, Y. P. Huang, S. Saarakkala, H. Pulkkinen, V. Tiitu, A. Linjama, I. Kiviranta, M. J. Lammi, A. Brünott, H. Brommer, R. V. Weeren, P. A. J. Brama, Y. P. Zheng, J. S. Jurvelin, and J. Töyräs. Comparison of ultrasound and optical coherence tomography techniques for evaluation of integrity of spontaneously repaired horse cartilage. *Journal of Medical Engineering & Technology*, 36(3): 185–192, Apr. 2012.

T. Vos, A. D. Flaxman, M. Naghavi, R. Lozano, C. Michaud, M. Ezzati, K. Shibuya, J. A. Salomon, S. Abdalla, V. Aboyans, J. Abraham, I. Ackerman, R. Aggarwal, S. Y. Ahn, M. K. Ali, M. A. AlMazroa, M. Alvarado, H. R. Anderson, L. M. Anderson, K. G. Andrews, C. Atkinson, L. M. Baddour, A. N. Bahalim, S. Barker-Collo, L. H. Barrero, D. H. Bartels, M.-G. Basáñez, A. Baxter, M. L. Bell, E. J. Benjamin, D. Bennett, E. Bernabé, K. Bhalla, B. Bhandari, B. Bikbov, A. B. Abdulhak, G. Birbeck, J. A. Black, H. Blencowe, J. D. Blore, F. Blyth, I. Bolliger, A. Bonaventure, S. Boufous, R. Bourne, M. Boussinesq, T. Braithwaite, C. Brayne, L. Bridgett, S. Brooker, P. Brooks, T. S. Brugha, C. Bryan-Hancock, C. Bucello, R. Buchbinder, G. Buckle, C. M. Budke, M. Burch, P. Burney, R. Burstein, B. Calabria, B. Campbell, C. E. Canter, H. Carabin, J. Carapetis, L. Carmona, C. Cella, F. Charlson, H. Chen, A. T.-A. Cheng, D. Chou, S. S. Chugh, L. E. Coffeng, S. D. Colan, S. Colquhoun, K. E. Colson, J. Condon, M. D. Connor, L. T. Cooper, M. Corriere, M. Cortinovis, K. C. de Vaccaro, W. Couser, B. C. Cowie, M. H. Criqui, M. Cross, K. C. Dabhadkar, M. Dahiya, N. Dahodwala, J. Damsere-Derry, G. Danaei, A. Davis, D. De Leo, L. Degenhardt, R. Dellavalle, A. Delossantos, J. Denenberg, S. Derrett, D. C. Des Jarlais, S. D. Dharmaratne, M. Dherani, C. Diaz-Torne, H. Dolk, E. R. Dorsey, T. Driscoll,

H. Duber, B. Ebel, K. Edmond, A. Elbaz, S. E. Ali, H. Erskine, P. J. Erwin, P. Espindola, S. E. Ewoigbokhan, F. Farzadfar, V. Feigin, D. T. Felson, A. Ferrari, C. P. Ferri, E. M. Fèvre, M. M. Finucane, S. Flaxman, L. Flood, K. Foreman, M. H. Forouzanfar, F. G. R. Fowkes, R. Franklin, M. Fransen, M. K. Freeman, B. J. Gabbe, S. E. Gabriel, E. Gakidou, H. A. Ganatra, B. Garcia, F. Gaspari, R. F. Gillum, G. Gmel, R. Gosselin, R. Grainger, J. Groeger, F. Guillemin, D. Gunnell, R. Gupta, J. Haagsma, H. Hagan, Y. A. Halasa, W. Hall, D. Haring, J. M. Haro, J. E. Harrison, R. Havmoeller, R. J. Hay, H. Higashi, C. Hill, B. Hoen, H. Hoffman, P. J. Hotez, D. Hoy, J. J. Huang, S. E. Ibeanusi, K. H. Jacobsen, S. L. James, D. Jarvis, R. Jasrasaria, S. Jayaraman, N. Johns, J. B. Jonas, G. Karthikeyan, N. Kassebaum, N. Kawakami, A. Keren, J.-P. Khoo, C. H. King, L. M. Knowlton, O. Kobusingye, A. Koranteng, R. Krishnamurthi, R. Lalloo, L. L. Laslett, T. Lathlean, J. L. Leasher, Y. Y. Lee, J. Leigh, S. S. Lim, E. Limb, J. K. Lin, M. Lipnick, S. E. Lipshultz, W. Liu, M. Loane, S. L. Ohno, R. Lyons, J. Ma, J. Mabweijano, M. F. MacIntyre, R. Malekzadeh, L. Mallinger, S. Manivannan, W. Marcenes, L. March, D. J. Margolis, G. B. Marks, R. Marks, A. Matsumori, R. Matzopoulos, B. M. Mayosi, J. H. McAnulty, M. M. McDermott, N. McGill, J. McGrath, M. E. Medina-Mora, M. Meltzer, Z. A. Memish, G. A. Mensah, T. R. Merriman, A.-C. Meyer, V. Miglioli, M. Miller, T. R. Miller, P. B. Mitchell, A. O. Mocumbi, T. E. Moffitt, A. A. Mokdad, L. Monasta, M. Montico, M. Moradi-Lakeh, A. Moran, L. Morawska, R. Mori, M. E. Murdoch, M. K. Mwaniki, K. Naidoo, M. N. Nair, L. Naldi, K. V. Narayan, P. K. Nelson, R. G. Nelson, M. C. Nevitt, C. R. Newton, S. Nolte, P. Norman, R. Norman, M. O'Donnell, S. O'Hanlon, C. Olives, S. B. Omer, K. Ortblad, R. Osborne, D. Ozgediz, A. Page, B. Pahari, J. D. Pandian, A. P. Rivero, S. B. Patten, N. Pearce, R. P. Padilla, F. Perez-Ruiz, N. Perico, K. Pesudovs, D. Phillips, M. R. Phillips, K. Pierce, S. Pion, G. V. Polanczyk, S. Polinder, C. A. Pope III, S. Popova, E. Porrini, F. Pourmalek, M. Prince, R. L. Pullan, K. D. Ramaiah, D. Ranganathan, H. Razavi, M. Regan, J. T. Rehm, D. B. Rein, G. Remuzzi, K. Richardson, F. P. Rivara, T. Roberts, C. Robinson, F. R. De Leòn, L. Ronfani, R. Room, L. C. Rosenfeld, L. Rushton, R. L. Sacco, S. Saha, U. Sampson, L. Sanchez-Riera, E. Sanman, D. C. Schwebel, J. G. Scott, M. Segui-Gomez, S. Shahraz, D. S. Shepard, H. Shin, R. Shivakoti, D. Silberberg, D. Singh, G. M. Singh, J. A. Singh, J. Singleton, D. A. Sleet, K. Sliwa, E. Smith, J. L. Smith, N. J. Stapelberg, A. Steer, T. Steiner, W. A. Stolk, L. J. Stovner, C. Sudfeld, S. Syed, G. Tamburlini, M. Tavakkoli, H. R. Taylor, J. A. Taylor, W. J. Taylor, B. Thomas, W. M. Thomson, G. D. Thurston, I. M. Tleyjeh, M. Tonelli, J. A. Towbin, T. Truelsen, M. K. Tsilimbaris, C. Ubeda, E. A. Undurraga, M. J. van der Werf, J. van Os, M. S. Vavilala, N. Venketasubramanian, M. Wang, W. Wang, K. Watt, D. J. Weatherall, M. A. Weinstock, R. Weintraub, M. G. Weisskopf, M. M. Weissman, R. A. White, H. Whiteford, S. T. Wiersma, J. D. Wilkinson, H. C. Williams, S. R. Williams, E. Witt, F. Wolfe, A. D. Woolf, S. Wulf, P.-H. Yeh, A. K. Zaidi, Z.-J. Zheng, D. Zonies, A. D. Lopez, and C. J.

Murray. Years lived with disability (YLDs) for 1160 sequelae of 289 diseases and injuries 1990–2010: a systematic analysis for the Global Burden of Disease Study 2010. *The Lancet*, 380(9859):2163–2196, Dec. 2012.

I. J. Wallace, S. Worthington, D. T. Felson, R. D. Jurmain, K. T. Wren, H. Maijanen, R. J. Woods, and D. E. Lieberman. Knee osteoarthritis has doubled in prevalence since the mid-20th century. *Proceedings of the National Academy of Sciences of the United States of America*, 114(35):9332–9336, Aug. 2017.

C.-T. Wang, J. Lin, C.-J. Chang, Y.-T. Lin, and S.-M. Hou. Therapeutic Effects of Hyaluronic Acid on Osteoarthritis of the Knee. *J Bone Joint Surg Am*, 86(3): 538–545, Mar. 2004.

S.-Z. Wang, Y.-P. Huang, S. Saarakkala, and Y.-P. Zheng. Quantitative Assessment of Articular Cartilage with Morphologic, Acoustic and Mechanical Properties Obtained Using High-Frequency Ultrasound. *Ultrasound in Medicine & Biology*, 36 (3):512–527, Mar. 2010.

P. N. T. Wells. Absorption and dispersion of ultrasound in biological tissue. *Ultrasound in Medicine & Biology*, 1(4):369–376, Mar. 1975.

E. Willbold and F. Witte. Histology and research at the hard tissue–implant interface using Technovit 9100 New embedding technique. *Acta Biomaterialia*, 6(11): 4447–4455, Nov. 2010.

B. Willie, T. Pap, C. Perka, C. Schmidt, F. Eckstein, A. Arampatzis, H.-C. Hege, H. Madry, A. Vortkamp, and G. Duda. OVERLOAD – Rolle der Gelenküberlastung in der primären Arthrose: Die Krankheitsprogression verstehen und vermeiden. *Zeitschrift für Rheumatologie*, 74(7):618–621, Sept. 2015.

T. S. d. Windt, G. H. Welsch, M. Brittberg, L. Vonk, S. Marlovits, S. Trattnig, D. B. F. Saris, A. J. Blackman, M. V. Smith, D. C. Flanigan, M. J. Matava, R. W. Wright, and R. H. Brophy. Correlation Between Magnetic Resonance Imaging and Clinical Outcomes After Knee Cartilage Repair: Letter to the Editor. *The American Journal of Sports Medicine*, 41(11):NP48–NP50, Nov. 2013a.

T. S. d. Windt, G. H. Welsch, M. Brittberg, L. A. Vonk, S. Marlovits, S. Trattnig, and D. B. F. Saris. Is Magnetic Resonance Imaging Reliable in Predicting Clinical Outcome After Articular Cartilage Repair of the Knee? A Systematic Review and Meta-analysis. *The American Journal of Sports Medicine*, 41(7):1695–1702, July 2013b.

S. Witjes, V. Gouttebarge, P. P. F. M. Kuijer, R. C. I. v. Geenen, R. W. Poolman, and G. M. M. J. Kerkhoffs. Return to Sports and Physical Activity After Total and Unicondylar Knee Arthroplasty: A Systematic Review and Meta-Analysis. *Sports Medicine*, 46(2):269–292, Feb. 2016.

M. Yoshida, Z. Zea-Aragon, K. Ohtsuki, M. Ohnishi, and S. Ohno. Ultrastructural study of upper surface layer in rat mandibular condylar cartilage by quick-freezing method. *Histology and Histopathology*, 19(4):1033–1041, Oct. 2004.

E. Zhang, J. Laufer, and P. Beard. Backward-mode multiwavelength photoacoustic scanner using a planar Fabry-Perot polymer film ultrasound sensor for high-resolution three-dimensional imaging of biological tissues. *Applied Optics*, 47(4): 561–577, Feb. 2008.

M. Zhang, Y. Zheng, and A. F. Mak. Estimating the effective Young's modulus of soft tissues from indentation tests—nonlinear finite element analysis of effects of friction and large deformation. *Medical Engineering & Physics*, 19(6):512–517, Sept. 1997.

M. Zscharnack, P. Hepp, R. Richter, T. Aigner, R. Schulz, J. Somerson, C. Josten, A. Bader, and B. Marquass. Repair of Chronic Osteochondral Defects Using Predifferentiated Mesenchymal Stem Cells in an Ovine Model. *The American Journal of Sports Medicine*, 38(9):1857–1869, Sept. 2010.

Supplementary Information

Table 6.1 – Macroscopic scoring - Outerbridge

Score	Description
0	Normal cartilage
1	Cartilage with softening and swelling
2	A partial-thickness defect with fissures on the surface that do not reach subchondral bone or exceed 1.5 cm in diameter
3	Fissuring to the level of subchondral bone in an area with a diameter more than 1.5 cm
4	Exposed subchondral bone

Table 6.2 – Macroscopic scoring - ICRS-CRA

Item	**Score**	**Description**
Degree of defect repair	4	In level with surrounding cartilage
	3	75 % repair of defect depth
	2	50 % repair of defect depth
	1	25 % repair of defect depth
	0	0 % repair of defect depth
Integration to border zone	4	Complete integration with surrounding cartilage, Demarcating border < 1 mm
	3	75 % of graft integrated, 25 % with notable border > 1 mm width
	1	50 % of graft integrated with surrounding cartilage, 50 % with a notable border > 1 mm
	0	From no contact to 25% of graft integrated with surrounding cartilage
Macrosopic appearance	4	Intact smooth surface
	3	Fibrillated surface
	2	Small, scattered fissures or cracks
	1	Several, small or few but large fissures
	0	Total degeneration of graft area
Maximum cumulative score	12	

Table 6.3 – MOCART scoring

Item	Score	Description
1 - Degree of defect repair	20	Complete (on a level with adjacent cartilage)
	15	Hypertrophy
	10	$> 50\,\%$
	5	$< 50\,\%$
	0	Subchondral bone exposed
2 - Integration to border zone	15	Complete (integration with adjacent cartilage)
	10	Demarcating border visible
	5	Defect visible $< 50\,\%$ of the length of the repair tissue
	0	Defect visible $> 50\,\%$ of the length of the repair tissue
3 - Surface of the repair tissue (Dual T2-FSE or 3D-GE-FS)	10	Intact (lamina splendens intact)
	5	Damaged $< 50\,\%$ of repair tissue depth
	0	Damaged $> 50\,\%$ of repair tissue depth
4 - Structure of the repair tissue	5	Homogenous
	0	Inhomogenous or cleft formation
5 - Signal intensity of the repair tissue	10	Isointense
	5	Moderately hyperintense
	0	Markedly hyperintense
6 - Subchondral lamina	5	Intact
	0	Non-intact
7 - Subchondral bone	10	Intact
	5	Non-intact (edema, granulation tissue, cysts, sclerosis)
Maximum cumulative score	75	

Table 6.4 – Sequences used for MRI imaging

Sequence	FOV [mm]	matrix	slice [mm]	TR [ms]	TE [ms]
T1 TIRM cor	150 x 150	512 x 512	3	4810	43
T1 SE sag	150 x 150	512 x 488	3	502	11
PD+T2 SE sag	180 x 180	448 x 448	3	450	10/70
T2 TRUFI cor 3D	160 x 160	384 x 384	0.4	10	4.85

Table 6.5 – ODriscoll scoring

Item	Score	Description
1 – Cellular morphology	4	Hyaline articular cartilage
	2	Incomplete different mesenchyme
	0	Fibrous tissue or bone
2 – Safranin-O staining of the matrix	3	Normal or nearly normal
	2	Moderate
	1	Slight
	0	None
3 – Surface regularity	3	Smooth and intact
	2	Superficial horizontal lamination
	1	Fissures – 25-100 % of the thickness
	0	Severe disruption, including fibrillation
4 – Structural integrity	2	Normal
	1	Slight disruption, including cysts
	0	Severe disintegration
5 – Thickness	2	100 % of normal adjacent cartilage
	1	50-100 % of normal cartilage
	0	0-50 % of normal cartilage
6 – Bonding to adjacent cartilage	2	Bonded at both ends of graft
	1	Bonded at one end, or partially at both ends
	0	Not bonded
7 – Hypocellularity	3	Normal cellularity
	2	Slight hypocellularity
	1	Moderate hypocellularity
	0	Severe hypocellularity
8 – Chondrocyte clustering	2	No clusters
	1	< 25 % of the cells
	0	25-100 % of the cells
9 – Freedom of degenerative changes in adjacent cartilage	3	Normal cellularity, no clusters, normal staining
	2	Normal cellularity, mild clusters, moderate staining
	1	Mild or moderate hypocellularity, slight staining
	0	Severe hypocellularity, poor or no staining
Maximum cumulative score	24	

Table 6.6 – Histopathological classification systems according to ICRS-I.

Item	**Score**	**Description**
I – Surface	3	smooth/continuous
	0	Discontinuities/irregularities
II – Matrix	3	Hyaline
	2	Mixture: hyaline/fibrocartilage
	1	Fibrocartilage
	0	Fibrous tissue
III – Cell distribution	3	Columnar
	2	Mixed/columnar-clusters
	1	Cluster
	0	Individual cells/disorganized
IV – Cell population	3	Predominantly viable
	1	Partially viable
	0	$< 10\,\%$ viable
V – Subchondral bone	3	Normal
	2	Increased remodeling
	1	Bone necrosis/granulation tissue
	0	Detached/fracture/callus at base
VI – Cartilage mineralization	3	Normal
	0	Abnormal/inappropriate location
Maximal cumulative score	18	

Table 6.7 – Histopathological classification systems according to ICRS-II.

Item		**Score**	**From 0**	**to 100**
1	Tissue morphology (PLM)	0-100	Full-thickness collagen fibers	Normal cartilage birefringence
2	Matrix straining (metachromasia)	0-100	No staining	Full metachromasia
3	Cell morphology	0-100	No round/oval cells	Mostly round/oval cells
4	Chondrocyte clustering	0-100	Present	Absent
5	Surface architecture	0-100	Delamination, or major irregularity	Smooth surface
6	Basal integration	0-100	No integration	Complete integration
7	Formation of a tidemark	0-100	No calcification front	Tidemark
8	Subchondral bone abnormalities/marrow fibrosis	0-100	Abnormal	Normal marrow
9	Inflammation	0-100	Present	Absent
10	Abnormal calcification/ossification	0-100	Present	Absent
11	Vascularization	0-100	Present	Absent
12	Surface/superficial assessment	0-100	Total loss or complete disruption	Resembles intact articular cartilage
13	Mid/deep zone assessment	0-100	Fibrous tissue	Normal hyaline cartilage
14	overall assessment	0-100	Bad (fibrous tissue)	Good (hyaline cartilage)
cumulative score (mean)		0-100		

List of Figures

List of Tables

List of Publications

M. Schöne, R. M. Schulz, H. Tzschätzsch, P. Varga, and K. Raum. Ultrasound palpation for fast in-situ quantification of articular cartilage stiffness, thickness and relaxation capacity. *Biomechanics and Modeling in Mechanobiology*, pages 1–15, Feb. 2017.

M. Schöne, N. Männicke, J. S. Somerson, B. Marquaß, R. Henkelmann, T. Aigner, K. Raum, and R. M. Schulz. 3d ultrasound biomicroscopy for assessment of cartilage repair tissue: volumetric characterisation and correlation to established classification systems. *European Cells & Materials*, 31:119–135, 2016.

N. Männicke, **M. Schöne**, J. Liukkonen, D. Fachet, S. Inkinen, M. K. Malo, M. L. Oelze, J. Töyräs, J. S. Jurvelin, and K. Raum. Species-Independent Modeling of High-Frequency Ultrasound Backscatter in Hyaline Cartilage. *Ultrasound in Medicine & Biology*, 42(6):1375–1384, June 2016.

N. Männicke, **M. Schöne**, M. Oelze, and K. Raum. Articular cartilage degeneration classification by means of high-frequency ultrasound. *Osteoarthritis and Cartilage*, 22(10):1577–1582, Oct. 2014.

N. Männicke, **M. Schöne**, M. Gottwald, F. Göbel, M. L. Oelze, and K. Raum. 3-D High-Frequency Ultrasound Backscatter Analysis of Human Articular Cartilage. *Ultrasound in Medicine & Biology*, 40(1):244–257, Jan. 2014.

M. Schöne, N. Männicke, M. Gottwald, F. Göbel, and K. Raum. 3-D High-Frequency Ultrasound Improves the Estimation of Surface Properties in Degenerated Cartilage. *Ultrasound in Medicine & Biology*, 39(5):834–844, May 2013.

K. Gelse, A. Olk, S. Eichhorn, B. Swoboda, **M. Schoene**, and K. Raum. Quantitative ultrasound biomicroscopy for the analysis of healthy and repair cartilage tissue. *European Cells & Materials*, 19:58–71, 2010.

Acknowledgements

This work was carried out during my time as a PhD student at the Berlin-Brandenburg School of Regenerative Therapies, at the Charité - Universitätsmedizin Berlin. It was financially supported by the Deutsche Forschungsgemeinschaft (DFG, Ra1380/6) and by the German Federal Ministry for Economic Affairs and Energy (BMWi) as a ZIM cooperation project (KF2744004LW3).

First, I like to thank my doctoral supervisor Kay Raum for the long time of support starting before by university degree until my PhD work. I am grateful for the challenging tasks and the possibility to join an international research community.

I want like to express my deepest appreciation to the members of the jury for taking the time to examine my work.

I am deeply indepted to Ronny Schulz for the opportunity to take part in his preclinical studies and for the hours of fruitful discussions.

For the time in Kuopio, Finland I am very grateful to the group of Prof. Dr. Jukka Jurvelin and Prof. Dr. Juha Töyräs, for the sharing of knowledge, the inspiring discussions and introduction into the Finnish culture. Especially the hospitality of Jukka Liukkonen and Markus Malo made this time memorable.

Further, I would like to thank Peter Varga for the constructive discussions and support in FE modeling, but also for his care on a personal level.

I have greatly benefited from Heiko Tzschätzsch, who shared his knowledge about ultrasound elastography and by that added a tremendous improvement to the signal analysis of ultrasound palpation.

I also wish to thank the company GAMPT, especially Michael Schultz, Georg Dietrich and Sven Sonntag, who realized my ideas of the USP prototype.

Thanks to my local butcher's shop Dornig, who regularly provided me with some samples of fresh cartilage after we had a common definition of a patella.

I am extremely grateful to Nils Männicke for our great collaboration in the "carti-

lage team", for the bilateral support in signal analysis and experimental design, and on top of that for a good friendship.

Huge thanks also go to Susanne Schrof for sharing the ups and downs of our PhD time, but ensuring the good moments prevail by her ubiquitous joviality and by playing pranks on Nils or proclaiming ridiculous challenges.

Thanks to all colleagues of our research group. Thank you Bernhard Hesse, Gianluca Iori, Julia Märk, Regina Puts, Jana Hradilova, Anke Kadow-Romacker, Johannes Schneider, Sannachi Lakshmanan, Daniel Rohrbach. You all contributed to marvelous moments during my PhD time.

Finally, I want to express my deepest gratitude to my family for their continuous support and giving me the time to finish this thesis. Especially thanks to my wife Sylvia, my parents, parents-in-law, grandparents and to my brother.

Hiermit erkläre ich, die Dissertation selbstständig und nur unter Verwendung der angegebenen Hilfen und Hilfsmittel angefertigt zu haben. Ich habe mich nicht anderwärts um einen Doktorgrad in dem Promotionsfach beworben und besitze keinen entsprechenden Doktorgrad. Die Promotionsordnung der Mathematisch-Naturwissenschaftlichen Fakultät, veröffentlicht im Amtlichen Mitteilungsblatt der Humboldt-Universität zu Berlin Nr. 42 am 11. Juli 2018, habe ich zur Kenntnis genommen.

Berlin, den _____